

LARGE-SCALE FILMS AND COHERENT HETEROSTRUCTURES OF ATOMIC  
THICKNESS

A Dissertation

Presented to the Faculty of the Graduate School

of Cornell University

In Partial Fulfillment of the Requirements for the Degree of

Doctor of Philosophy

by

Saien Xie

August 2018

© 2018 Saien Xie

# LARGE-SCALE FILMS AND COHERENT HETEROSTRUCTURES OF ATOMIC THICKNESS

Saien Xie, Ph. D.

Cornell University 2018

Thin film materials are the key elements in modern technology, including electronics and photonics. The production of semiconducting thin films with spatially-controlled composition has enabled various applications such as computer chips, photovoltaics, and display technologies. A decrease in film thickness to the atomic scale, a challenging limit for traditional semiconductors (such as Si and GaAs), represents the ultimate thinness limit of thin film engineering and would further advance applications such as flexible electronics.

Transition metal dichalcogenides (TMDs), which form stable three-atom-thick monolayers, provide an ideal material platform for semiconducting thin film engineering in the ultimate atomic-thickness limit. The unique electronic band structures of monolayer TMDs enable remarkable functionalities of TMD monolayers, including high mobility, direct bandgap, large excitonic effect, and valleytronics. While existing experiments have been demonstrated with mechanically exfoliated samples, the full potential of monolayer TMDs cannot be realized without a method that produces these materials in a scalable manner. There are two major challenges regarding the material synthesis of TMD monolayers—large-scale uniform monolayer film and high-quality heterostructure within the monolayer plane.

In this thesis, I present the efforts toward resolving these two challenges based on semiconducting monolayer TMDs. We first describe the synthesis of wafer-scale, high-mobility monolayer TMD films such as molybdenum disulfide. We then demonstrate coherent monolayer TMD heterostructures and superlattices, in which 4% lattice mismatched tungsten disulfide and tungsten diselenide are laterally integrated in the monolayer plane without dislocations. The lattice coherence results in a large strain which is used to precisely engineer the optical band gaps and mechanical deformation of these TMD monolayers. We further construct high-performance (opto-) electronic devices based on heterostructures with monolayer thickness. Finally, we demonstrate that monolayer TMDs can serve as atomic building blocks for creating vertically-heterostructured films containing both TMDs and non-layered materials.

## BIOGRAPHICAL SKETCH

Saien grew up in Shenzhen, Guangdong, China. After receiving a B.S. in Mathematics and Physics from Tsinghua University in 2012, he entered the Applied Physics doctoral program at Cornell University in Ithaca, New York. He completed his Ph.D. research under the supervision of Prof. Jiwoong Park.

To my parents

## ACKNOWLEDGMENTS

Throughout these years of graduate school, I have been truly fortunate to interact with many great people. First and foremost, I am deeply indebted to my advisor Jiwoong Park, for his constant support and guidance. I appreciate deeper and deeper how fortunate I am to have learned from him both scientifically and personally. His exceptional taste for science and attention to detail have been inspiring to me, and will continue to inspire me in years to come.

I am extremely grateful to the other members of my committee—Paul McEuen, David Muller, and Frank DiSalvo—whose insights and advice have been priceless over the years. I am also grateful to have learned from many professors through collaboration and discussion, including Robert DiStasio, Abhay Pasupathy, Vanessa Sih, Philip Kim, Hongkun Park, Donhee Ham, Darrell Schlom, and Greg Engel. I was fortunate to have worked with many talented students and postdocs from these groups, with special thanks to Lijie Tu, Ka Un Lao, Xiaodong Zhou, Alex Kerelsky, Xinlin Song, Andrew Joe, Luis Jauregui, Kateryna Pistunova, You Zhou, Giovanni Scuri, Jiho Sung, Chengye Liu, Houk Jang, Yi Jiang, Michael Cao, Pratiti Deb, Nathaniel Schreiber, and Ryan Wood.

I have been extremely fortunate to work with fantastic labmates in the Park group at two great places during my graduate study: Cornell University and The University of Chicago. Mark, thank you for teaching me the process of device fabrication and how to work with vacuum parts at the beginning of my graduate study. Kibum, I cherish the days and nights we spent working together. Cheol-Joo and Fai, I will always remember the fun discussions and activities we took part in outside the lab. I also enjoyed the

discussions and time spent with Wei, LiHong, Carlos, Robin, Lola, Matt, Lujie, Joel, Yui, Kan-Heng, Yimo, Marcos, Hui, Alan, Zack, Chibeom, Long, Lei, Preeti, Joonki, Yu, Kim, Fauzia, Josh, Andy, and Baorui.

Lastly, I would like to thank my parents for their unconditional love and support, without whom none of my achievements would have been possible.

## TABLE OF CONTENTS

Biographical Sketch.....	v
Dedication.....	vi
Acknowledgements .....	vii
Table of Contents .....	ix
List of Figures.....	xi
<b>Chapter 1: Introduction and Overview</b>	
1.1 Thesis Overview.....	1
1.2 Multifunctional Monolayers.....	4
1.3 Preparation of TMDs.....	9
1.4 Thesis Preview.....	14
<b>Chapter 2: Characterization of Atomically-Thin Transition Metal Dicalcogenides</b>	
2.1 Introduction .....	16
2.2 Optical Microscopy Identification of TMDs.....	17
2.3 Compositional Characterization with Optical Spectroscopies .....	19
2.4 Structural Analysis with Transmission Electron Microscopy .....	25
2.5 Electrical Characterizations.....	32
2.6 Summary.....	33
<b>Chapter 3: High-Mobility Monolayer Transition Metal Dichalcogenides with Wafer-Scale Homogeneity</b>	
3.1 Introduction .....	35
3.2 Monolayer TMD Films with Wafer-Scale Uniformity .....	36
3.3 Metal-Organic Chemical Vapor Deposition for Monolayer TMDs.....	39
3.4 Layer-By-Layer Growth and Grain Size Control.....	40
3.5 High Electrical Performance of Monolayer TMDs.....	46
3.6 Wafer-Scale Batch Fabrication of Monolayer TMD FETs .....	50
3.7 Summary.....	51
<b>Chapter 4: Coherent, Monolayer Transition Metal Dichalcogenide Superlattices with Engineered Strain</b>	
4.1 Introduction .....	54
4.2 Synthesis of Monolayer TMD Superlattices: Modulated MOCVD .....	57
4.3 Lattice Coherence of WS <sub>2</sub> /WSe <sub>2</sub> Superlattices. ....	60
4.4 Omnidirectional Epitaxy .....	64
4.5 Strain Engineering of Photoluminescence of WS <sub>2</sub> /WSe <sub>2</sub> Superlattices .....	68
4.6 Compressive Strain Induced Out-of-Plane Ripples in WSe <sub>2</sub> .....	70
4.7 Summary.....	75
<b>Chapter 5: High Performance Monolayer Devices</b>	
5.1 Introduction .....	76
5.2 Monolayer WSe <sub>2</sub> /WS <sub>2</sub> P-N Diodes .....	77

5.3 Double Heterostructure (DH) Transistors .....	83
5.4 Monolayer Transistor: Metal-Semiconductor Heterojunctions.....	84
5.5 Low Contact Resistance of Graphene Electrodes .....	91
5.6 Summary.....	94
<b>Chapter 6: Hybrid Thin Films with Vertically Programmed Composition</b>	
6.1 Introduction .....	95
6.2 Hybrid Films of MoS <sub>2</sub> /SiO <sub>2</sub> with Vertical Composition Control.....	96
6.3 Layer-by-Layer Assembly of TMDs into Wafer-Scale Vertical Heterostructures .....	98
6.4 Tuning Electrical Conductance of Stacked Semiconductor Films by Vertical Composition Control .....	106
6.5 TMD Films at Various Interfaces.....	109
6.6 Summary.....	110
<b>References .....</b>	<b>111</b>

## LIST OF FIGURES

Figure 1.1 Library of 2D materials.....	4
Figure 1.2 Structure of transition metal dichalcogenides.....	5
Figure 1.3 The three crystalline phases of group-VI TMDs.....	6
Figure 1.4 Direct band gaps and valleys of monolayer TMDs.....	7
Figure 1.5 Advantages of 2D materials compared to traditional 3D materials for electronic devices.....	8
Figure 1.6 Mechanical exfoliation of 2D materials to create ultra-thin layers.....	10
Figure 1.7 Schematics of various approaches of chemical synthesis of TMD films. ..	12
Figure 2.1 Optical contrast of TMDs on SiO <sub>2</sub> /Si substrates.....	18
Figure 2.2 Band structure and orbital contributions to electronic states of TMDs. ....	20
Figure 2.3 PL spectra of WS <sub>2</sub> and WSe <sub>2</sub> .....	21
Figure 2.4 Raman modes and spectra of TMDs.....	22
Figure 2.5 Widefield imaging based on Raman or photoluminescence.....	24
Figure 2.6 Diagram of TEM diffraction and imaging modes.....	26
Figure 2.7 DF-TEM imaging of monolayer TMDs.....	27
Figure 2.8 Schematic of STEM and ADF-STEM images of MoS <sub>2</sub> .....	29
Figure 2.9 EMPAD imaging of monolayer TMDs.....	31
Figure 2.10 Schematic of a monolayer MoS <sub>2</sub> FET.....	33
Figure 3.1 Wafer-scale monolayer TMD films.....	37
Figure 3.2 Uniform PL of patterned monolayer TMD films.....	38
Figure 3.3 MOCVD for monolayer TMDs.....	39
Figure 3.4 Layer-by-layer growth of monolayer TMDs.....	42
Figure 3.5 Thermal decomposition of precursors.....	43
Figure 3.6 Grain size control of monolayer TMD synthesis.....	44
Figure 3.7 Laterally stitched polycrystalline ML TMD films.....	46
Figure 3.8 Electrical characterization and batch fabrication of ML TMD FETs.....	47
Figure 3.9 Batch fabrication of ML TMD FETs.....	50
Figure 3.10 Synthesis of various TMDs on various substrates.....	52
Figure 4.1 Incoherent and coherent epitaxy.....	55
Figure 4.2 3D and 2D superlattices.....	56
Figure 4.3 2D monolayer TMD superlattices.....	57
Figure 4.4 Modulated MOCVD process.....	59
Figure 4.5 Lattice coherence of WS <sub>2</sub> /WSe <sub>2</sub> superlattices.....	61
Figure 4.6 Lattice coherence over entire WS <sub>2</sub> /WSe <sub>2</sub> superlattices.....	62
Figure 4.7 Lattice rotation map of an incoherent WS <sub>2</sub> /WSe <sub>2</sub> heterostructure.....	64
Figure 4.8 Schematic of conventional and omnidirectional epitaxy.....	66
Figure 4.9 Coarse-grained simulation of the coherent WS <sub>2</sub> /WSe <sub>2</sub> superlattice.....	67
Figure 4.10 Strain engineering of PL of WS <sub>2</sub> /WSe <sub>2</sub> superlattices.....	68
Figure 4.11 Formation of out-of-plane ripples in WSe <sub>2</sub> .....	71

Figure 4.12 AFM images of WS <sub>2</sub> /WSe <sub>2</sub> heterostructures. ....	73
Figure 4.13 Critical thickness analysis. ....	74
Figure 5.1 Electrical transport of WSe <sub>2</sub> /WS <sub>2</sub> p-n diodes without encapsulation. ....	78
Figure 5.2 Micrographs of fabrication of <i>h</i> -BN encapsulated TMD devices. ....	79
Figure 5.3 Electrical transport of WSe <sub>2</sub> /WS <sub>2</sub> p-n diodes with <i>h</i> -BN encapsulation. ...	79
Figure 5.4 Electroluminescence of WSe <sub>2</sub> /WS <sub>2</sub> p-n diodes without encapsulation. ....	81
Figure 5.5 Electrical transport of WSe <sub>2</sub> /WS <sub>2</sub> /WSe <sub>2</sub> double heterostructures. ....	82
Figure 5.6 Graphene-TMD lateral heterostructures using graphene as contact. ....	85
Figure 5.7 Graphene-TMD heterostructures with large scale uniformity. ....	87
Figure 5.8 Confirmation of lateral connection between graphene and TMD. ....	89
Figure 5.9 High performance 1D edge contact of graphene electrodes. ....	91
Figure 6.1 Monolayer TMDs as building blocks for 3D structures. ....	95
Figure 6.2 Hybrid thin film of SiO <sub>2</sub> /MoS <sub>2</sub> vertical heterostructures. ....	97
Figure 6.3 High-quality vertically-designed films using layer-by-layer assembly of monolayer TMDs. ....	99
Figure 6.4 Programmed vacuum stack (PVS) process. ....	101
Figure 6.5 Uniform Raman and optical absorption of PVS-stacked MoS <sub>2</sub> films. ....	103
Figure 6.6 Tuning electrical conductance of stacked semiconductor films using the number of layers or vertical composition. ....	105
Figure 6.7 TMD films at different interfaces. ....	107

## CHAPTER 1

### INTRODUCTION AND OVERVIEW

#### *1.1 Thesis Overview*

Thin film materials are the key elements in modern technology, including electronics and photonics. Producing thin films with spatially controlled composition has enabled various applications such as computer chips, photovoltaics, display technology. Atomically-thin films represent thin films in the ultimate, atomic-thickness limit. Creating such atomically-thin thin films and freeing these films from rigid substrates would allow for advanced applications previously unavailable. However, it is difficult to achieve these goals with traditional semiconductors, such as Si and GaAs. Traditional three-dimensional (3D) semiconductors are unstable when thinned down to atomic thickness, and the dangling bonds which form at the surface often severely degrade the electrical performance of these thin films. Additionally, these thin films are covalently bonded to the substrates, making it challenging to produce freestanding films.

Two-dimensional (2D) materials, usually one- or few-atom thick, represent the ultimate, atomic-thickness limit of thin films. Strong lateral covalent bonds provide the in-plane mechanical strength for 2D materials. The absence of dangling bonds in the basal plane makes 2D materials stable even in the monolayer limit, allowing the preparation of atomically-thin films, even in a free-standing fashion. These stable 2D monolayers provide the ideal material platform for thin film engineering in the atomic-thickness limit. Furthermore, these monolayers can serve as building blocks for out-of-plane heterostructures—they can be vertically integrated with almost any foreign

substrates as well as other 2D materials, through their weak van der Waals (vdW) interactions. Such structural versatility presents the vast potential of 2D materials for a variety of applications.

There exists a large group of 2D materials with assorted compositions and properties. For example, any material of layered nature that can be thinned down to the monolayer limit can be regarded as a 2D material. Graphene, a single layer of carbon atoms arranged in a honeycomb lattice, is the a representative example of such 2D layered material [1]. Since the first fabrication of graphene devices in 2004, there has been a booming development of the 2D materials research for both fundamental and application purposes. Owing to the lack of compositional variation of graphene (i.e. consisting of only carbon), there has been tremendous effort spent on developing 2D materials with diverse compositions and properties.

Transition metal dichalcogenides (TMDs)—which form stable three-atom-thick monolayers—allow for the broad tuning of their properties via controlling the chemical composition. Monolayer TMDs display a variety of electronic properties, ranging from semiconducting to metallic, and superconducting. In addition, their unique electronic band structures enable unique functionalities of TMD monolayers, including the indirect-to-direct bandgap transition, large excitonic effect, valleytronics, and piezoelectricity [2–7]. Importantly, owing to their similar crystal structures, these TMD monolayers can be laterally integrated in the monolayer plane to form heterostructures and superlattices with monolayer thickness.

The production of high-quality films and heterostructures of monolayer thickness represents the ultimate, atomic-thickness limit of thin film engineering. Its realization exhibits two major challenges:

*(i) Production of high-quality monolayer TMD films with wafer-scale homogeneity.*

Similar to the silicon technologies which begin with the production of high-quality wafers, the production of wafer-scale TMDs is essential for their large-scale application. The existing techniques only produce monolayer TMDs with limited uniformity and electrical performance over large areas, limiting the application of such materials on a technologically relevant scale.

*(ii) Generation of high-quality TMD heterostructures in the monolayer plane.* The integration of different TMDs in the monolayer plane to create 2D heterostructures with precise spatial control (i.e. superlattices) not only provides a platform for studying epitaxy in the reduced two dimension, but also serves as building blocks for creating vertically-stacked hybrid films and exhibit unique properties that were inaccessible to their 3D analogs. A method that can produce high-quality monolayer TMD superlattices is lacking.

In order to achieve the full potential of monolayer TMDs for thin film engineering, these two challenges must be addressed. In this thesis, we focus on semiconducting TMDs, which mainly include MoS<sub>2</sub>, MoSe<sub>2</sub>, WS<sub>2</sub>, and WSe<sub>2</sub>. Importantly, our solutions to the challenges above can be applied to a variety of other TMDs, representing a general approach for producing functional atomically-thin films.

## 1.2 Multifunctional Monolayers

The essence of 2D materials is that the electrons in 2D materials can be described using two wave vectors. This 2D electronic feature is naturally held in any material that can be thinned down to the monolayer, molecular limit (e.g. graphene, TMDs). Non-layered materials can also be thinned down to the molecular thickness thus forming 2D materials (e.g. 2D silica glass [8]). The large variety of 2D materials makes them a powerful platform that can include multifunctions for material engineering while maintaining the monolayer thickness.

Graphene family	Graphene	hBN 'white graphene'	BCN	Fluorographene	Graphene oxide
2D chalcogenides	MoS <sub>2</sub> , WS <sub>2</sub> , MoSe <sub>2</sub> , WSe <sub>2</sub>		Semiconducting dichalcogenides: MoTe <sub>2</sub> , WTe <sub>2</sub> , ZrS <sub>2</sub> , ZrSe <sub>2</sub> , and so on	Metallic dichalcogenides: NbSe <sub>2</sub> , NbS <sub>2</sub> , TaS <sub>2</sub> , TiS <sub>2</sub> , NiSe <sub>2</sub> , and so on	
				Layered semiconductors: GaSe, GaTe, InSe, Bi <sub>2</sub> Se <sub>3</sub> , and so on	
2D oxides	Micas, BSCCO	MoO <sub>3</sub> , WO <sub>3</sub>	Perovskite-type: LaNb <sub>2</sub> O <sub>7</sub> , (Ca,Sr) <sub>2</sub> Nb <sub>3</sub> O <sub>10</sub> , Bi <sub>4</sub> Ti <sub>3</sub> O <sub>12</sub> , Ca <sub>2</sub> Ta <sub>2</sub> TiO <sub>10</sub> and so on		Hydroxides: Ni(OH) <sub>2</sub> , Eu(OH) <sub>2</sub> , and so on
	Layered Cu oxides	TiO <sub>2</sub> , MnO <sub>2</sub> , V <sub>2</sub> O <sub>5</sub> , TaO <sub>2</sub> , RuO <sub>3</sub> , and so on			Others

**Figure 1.1 Library of 2D materials.**

Currently known 2D materials that have been exfoliated down to monolayers. Reproduced from [9].

There is a vast collection of 2D materials besides graphene and TMDs, spanning a variety of crystal structures (Figure 1.1). These 2D materials exhibit diverse properties: ferromagnetic CrI<sub>3</sub> [10] and Cr<sub>2</sub>Ge<sub>2</sub>Te<sub>6</sub> [11], black phosphorus with band gaps as small as 0.3 eV [12, 13], high-T<sub>c</sub> superconductor FeSe [14, 15], and 2D polymers [16].

### ***Transition Metal Dichalcogenides (TMDs)***

TMDs are a group of layered materials with the stoichiometry MX<sub>2</sub>, where M is a transition metal element (for example, Mo, W, Nb, Zr, Ta) and X is a chalcogen element

(S, Se, Te) [17]. Monolayer TMDs are three atoms thick, where a layer of transition metal atoms is sandwiched between two layers of chalcogen atoms (Figure 1.2A). Depending on the composition, TMD monolayers exhibit a broad range of electronic properties (Figure 1.2B). Examples include semiconductors (e.g. MoS<sub>2</sub>, WSe<sub>2</sub>), metals (e.g. NbSe<sub>2</sub>), and superconductors (e.g. TaS<sub>2</sub>).

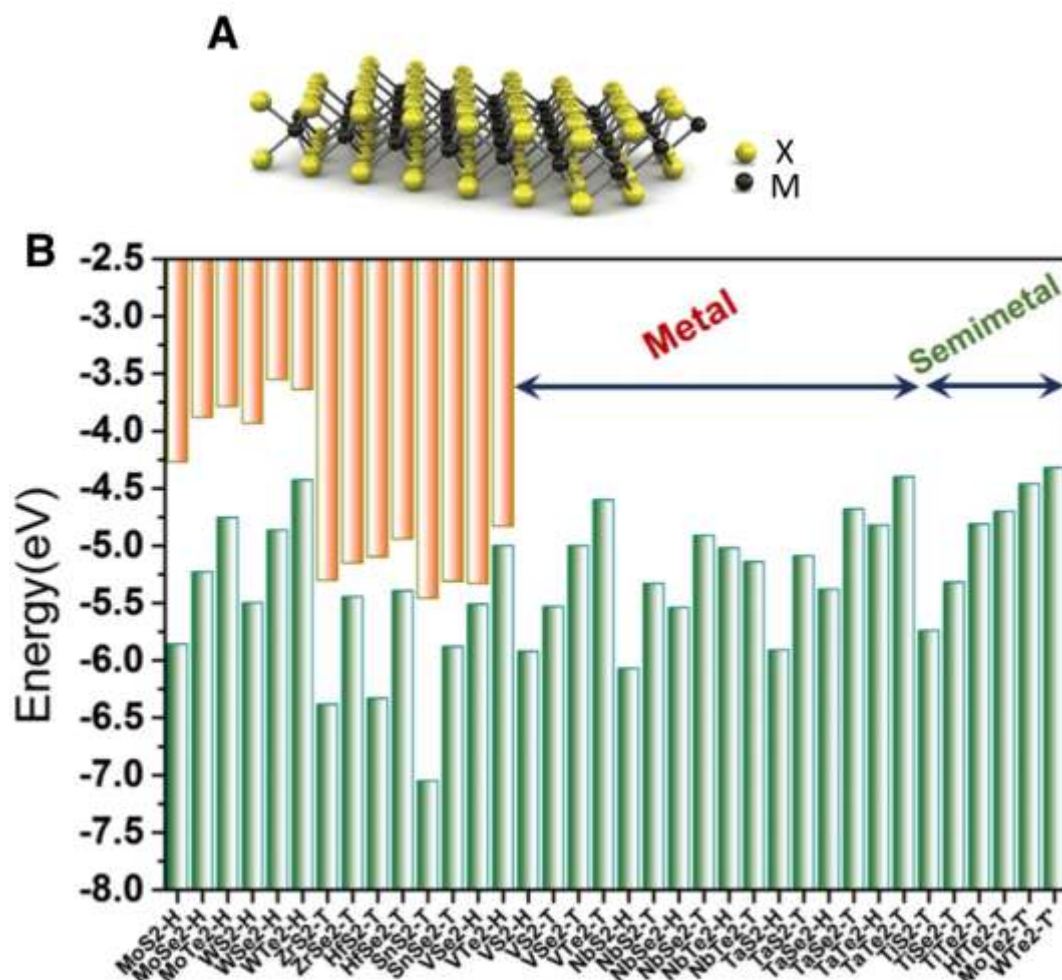


**Figure 1.2 Structure of transition metal dichalcogenides.** (A) Structure of TMD MX<sub>2</sub>, where a layer of metal atoms is sandwiched between two layers of chalcogen atoms. Reproduced from [17]. (B) Theory predicted conduction band minimum and valence band maximum of various monolayer TMDs plotted in orange and green columns. Reproduced from [18].

The variation in the lattice structures of monolayer TMDs provides another knob to tune their electronic properties. Three common structural phases (Figure 1.3) are trigonal prismatic (2H), in which the two layers of chalcogen atoms occupy the same in-plane position; octahedral (1T), in which the two layers of chalcogen atoms occupy different in-plane positions; and the distorted 1T, namely the 1T' phase. TMDs of different phases can have very different energies and show substantially different electronic properties. For instance, semiconducting 2H-MoS<sub>2</sub> is the most thermodynamically stable phase while the metallic 1T-MoS<sub>2</sub> is metastable (the thermodynamically stable phases of various TMDs are shown in Figure 1.3B) [19]. In this thesis, we will focus on semiconducting, 2H-phase group-VI TMDs (mainly MoS<sub>2</sub>, MoSe<sub>2</sub>, WS<sub>2</sub>, and WSe<sub>2</sub>), which are referred in this thesis simply as TMDs unless noted otherwise.

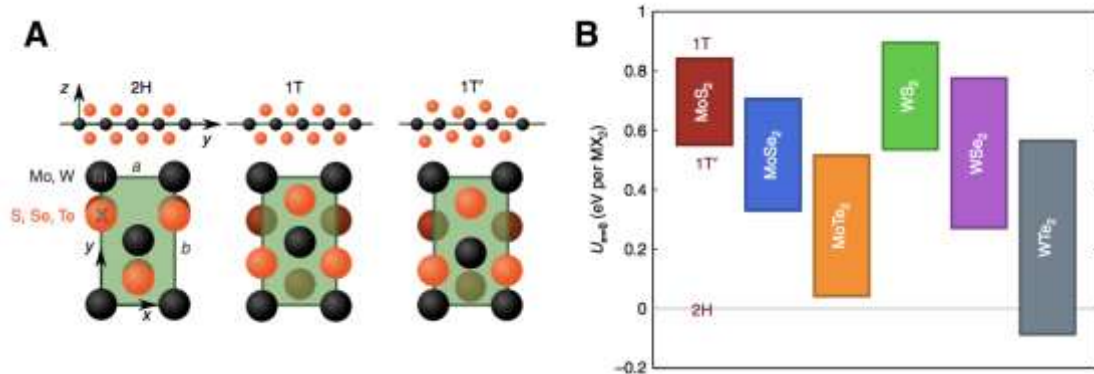


**Figure 1.3 The three crystalline phases of group-VI TMDs.**

(A) Schematic of trigonal prismatic (2H phase), octahedral (1T phase), and distorted octahedral (1T' phase) structures of TMDs. (B) Ground-state energy differences between 2H, 1T and 1T' phases of six different monolayer TMDs. Reproduced from [19].

A unique aspect of monolayer semiconducting TMDs is their direct band gaps, which are critical for optoelectronic applications such as light-emitting devices. For

example, monolayer MoS<sub>2</sub> has a direct gap at the K point, while MoS<sub>2</sub> thicker than bilayers become indirect-gapped due to the quantum confinement and the orbital constitution of the valence and conduction extrema (Figure 1.4) [20]. As a result, monolayer TMDs show much stronger photoluminescence than their thicker counterparts, making them ideal for optoelectronic applications (Figure 1.4B).

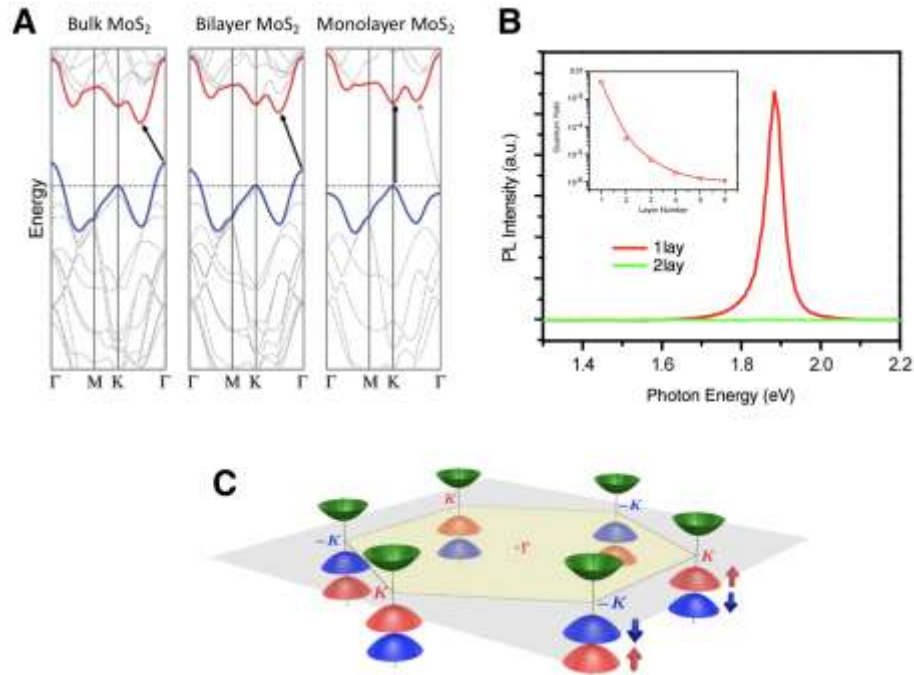


**Figure 1.4 Direct band gaps and valleys of monolayer TMDs.**

(A) Calculated band structures of bulk, bilayer, and monolayer MoS<sub>2</sub>, where a direct band gap only appears in monolayer MoS<sub>2</sub>. Reproduced from [31]. (B) PL spectra for mono- and bilayer MoS<sub>2</sub> samples in the photon energy range from 1.3 to 2.2 eV. Inset: PL quantum yield of MoS<sub>2</sub> with layer number 1-6. Reproduced from [3]. (C) Schematic drawing of the band structure at the band edges located at the K points, where spin- and valley-degree of freedom are locked in each valley. Reproduced from [24].

Symmetry plays an important role in 2D materials. Due to the absence of inversion symmetry in monolayer TMDs, the spin degeneracy at the K and K' valleys are lifted. As a result, the spin and valley degrees of freedom are locked in the electronic states at each valley, and the spin-up state at the K valley is degenerate with the spin-down state

at the K' valley due to the time reversal symmetry (Figure 1.4C) [21–23]. The unique spin- and valley-dependent electronic band structure can be utilized for manipulating the valley degree of freedom in these direct band gap semiconductors as demonstrated by the circular dichroism and valley specific properties [23–30].

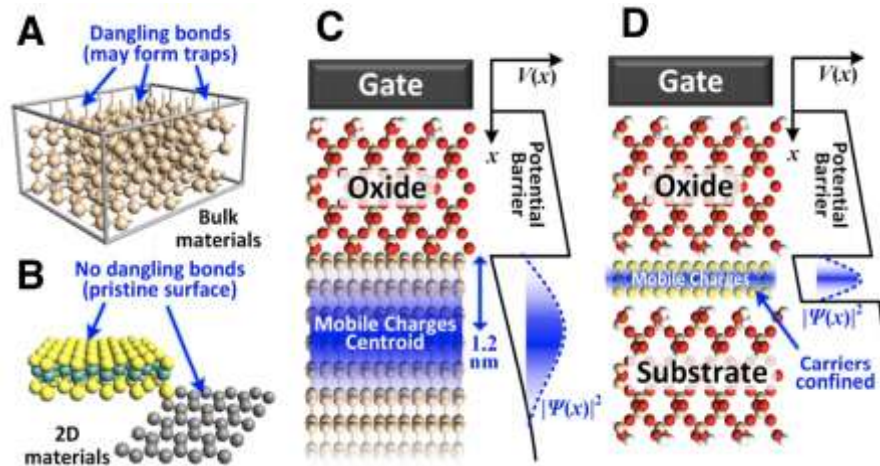


**Figure 1.5 Advantages of 2D materials compared to traditional 3D materials for electronic devices.**

(A) 3D semiconductors have dangling bonds that form traps for electrons and reduce the performance of field-effect transistors. (B) In contrast, 2D materials have pristine surfaces. (C) Gate electrostatics and mobile charge distribution in 3D semiconductors.  $V(x)$  is the gate voltage as a function of the distance  $x$ . The potential barrier is the energy level of the gate dielectric and  $|\Psi(x)|^2$  refers to the probability function of the carriers in the semiconductors. The majority of the mobile charge carriers are located approximately 1.2 nm from the semiconductor gate dielectric interface. (D) In 2D materials, charge carriers are confined in the atomically thin semiconductor, resulting in a narrower mobile charge distribution. This confinement of charge carriers allows the carriers to be easily controlled by the gate voltage, leading to excellent gate electrostatics. Reproduced from [33].

The stable surfaces of TMDs that are free of dangling bonds exhibit unique benefits for electronic device applications compared to conventional semiconducting thin films (Figure 1.5). The performance of transistors made from conventional 3D semiconductors significantly degrades when their thickness decreases. The mobility shows a thickness<sup>6</sup> dependence [32]. The decrease in mobility is due to the presence of

dangling bonds at the surfaces of 3D semiconductors which leads to stronger scattering of carriers due to interfacial states and phonons [33]. In contrast, TMDs that are free of dangling bonds facilitate carrier transport in the 2D channel. In addition, the leakage current between the source and drain can be significantly reduced in atomically-thin TMD based transistors because the conducting paths are confined in the atomic layer, whereas in 3D semiconductors there are always conducting channels in the bulk materials [33–35].

High performance field effect transistors (FETs) based on monolayer TMDs have been demonstrated in several works, including the lower leakage current monolayer MoS<sub>2</sub> FETs compared to single crystalline silicon FETs [34] and high mobility MoS<sub>2</sub> (monolayer: 60 cm<sup>2</sup>/Vs at room temperature and 1000 cm<sup>2</sup>/Vs at low temperature) [36–40]. Multilayer MoS<sub>2</sub> displays an enhanced mobility of 34000 cm<sup>2</sup>/Vs (six layer) [40]. Altogether, monolayer TMDs, despite their atomic thickness, show great promise for future electronic and optoelectronic applications.

### ***1.3 Preparation of TMDs***

Material research only prospers when the materials are easily accessible. For initial studies, mechanical exfoliation remains the most widely-used method for producing TMDs with high electrical and optical qualities. However, this is impossible to scale up due to the random shape and thickness of exfoliated flakes. Several chemical methods that produce TMDs on larger scales have been developed, including the chemical vapor deposition (CVD) method. Still, the growth of high-quality, monolayer TMD films with wafer-scale uniformity remained unsolved.

## ***Mechanical Exfoliation***

Utilizing a piece of sticky tape to cleave layered materials and create fresh surfaces is a well-known technique for surface science [41]. Efforts towards the production of ultra-thin TMDs date back to half a century. R. Frindt et al. produced MoS<sub>2</sub> flakes that were thinner than 10 nm by cleavage [42]. Still, the booming development of research on TMDs in the mono- and few- layer forms did not occur until this decade [3, 31], which was stimulated by the graphene research [43–46]. Mechanical exfoliation is ideal for generating micrometer sized mono- and few- layer flakes for prototype devices and fundamental studies. The process of mechanical exfoliation is illustrated in Figure 1.6A. First, bulk 2D crystals are adhered to the sticky side of scotch tape. Second, the tape is folded onto itself and then pulled apart to thin down the 2D crystals. A few iterations of this step will create 2D flakes with significantly reduced thicknesses. Third, by pressing the tape down to a clean substrate and gently peeling away, ultrathin 2D materials can leave the tape and stick onto the substrate via vdW interactions [47].

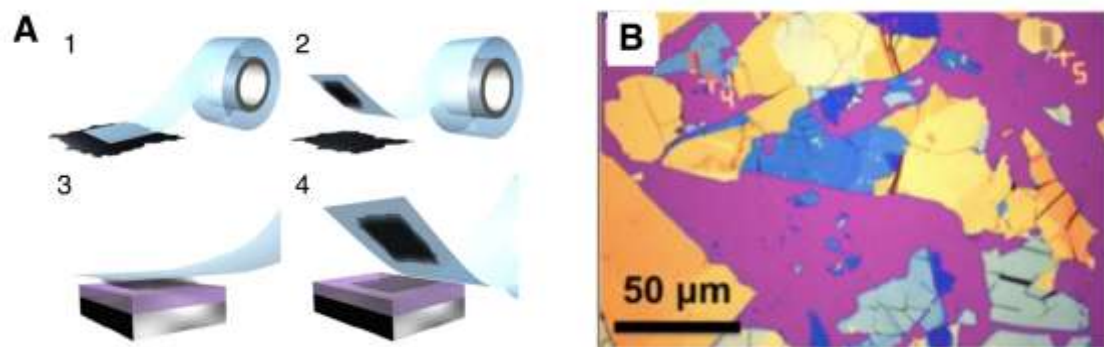


**Figure 1.6 Mechanical exfoliation of 2D materials to create ultra-thin layers.** (A) Process of mechanical exfoliation of 2D crystals. (1) Adhesive tape is pressed against a 2D crystal so that the top few layers are attached to the tape (2). (3) The tape with crystals of layered material is pressed against a surface of choice. (4) Upon peeling off, the bottom layer is left on the substrate. Reproduced from [47]. (B) A representative optical micrograph of 2D material flakes produced by mechanical exfoliation, displaying random thickness, shape, and spatial distribution. Reproduced from [48].

Mechanical exfoliation produces TMD flakes with random thickness, shape, and spatial distribution (Figure 1.6B). Micrometer-sized mono- and few- layer flakes can be identified using optical microscopy and other methods. Although the identification process can be time consuming, mechanical exfoliation remains the most widely used technique for producing ultrathin TMD flakes for prototyping devices for fundamental studies due to the simplicity of the process that does not require sophisticated instruments. TMDs produced by mechanical exfoliation often set the standards for electrical and optical properties.

### ***Chalcogenization of Metal or Metal Compounds***

One method to synthesize TMD films is the chalcogenization of deposited metal or metal compounds. Without the need to control both precursors at the same time, this method is straightforward for producing large-scale TMD films. In this method, films of elemental metals or metal compounds were deposited on target substrates and then heated up in the chalcogen environment, as schematically illustrated in Figure 1.7A. Chalcogenization of a variety of deposited materials, including Mo and MoO<sub>3</sub> have produced MoS<sub>2</sub> films of 2 - 12 layers [49–51], WS<sub>2</sub> films of 1 - 3, 18 - 20, and 39 - 41 layers [52]. While the chalcogenization method is straightforward, it only controls the average thickness of the synthesized TMD films, producing spatially inhomogeneous mixtures of monolayer, multi-layer and no-growth regions. The poor uniformity is fundamentally limited by the low mobility of metal atoms on the substrates as well as the lack of control over the metal precursor films. As a result, TMDs synthesized by this chalcogenization method are usually of small grain size below 100 nm and contain a

high density of defects [53], making this technique unsuitable for our goal of producing high-quality uniform monolayer films.

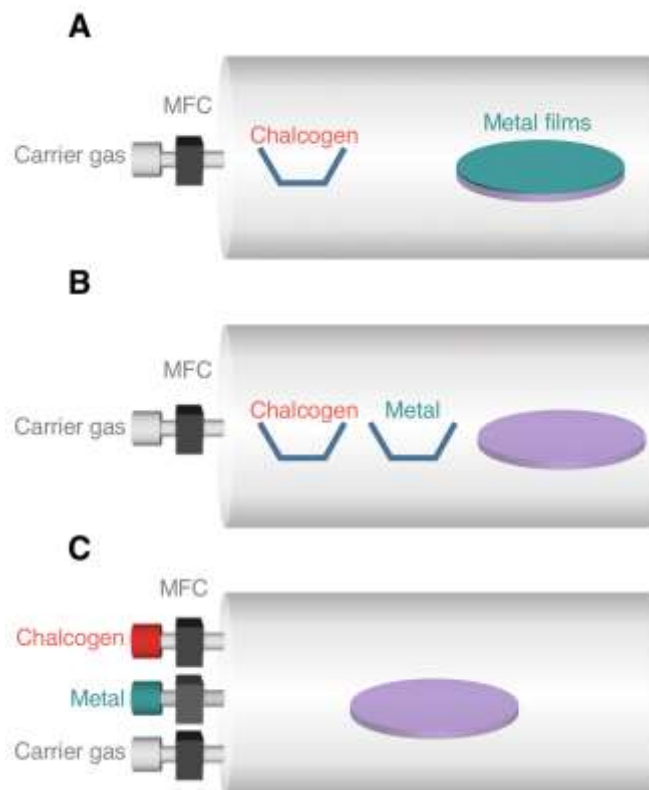


**Figure 1.7 Schematics of various approaches of chemical synthesis of TMD films.** (A) Chalcogenization of metal or metal compounds, where chalcogen precursor is placed upstream in a hot furnace. (B) CVD based on solid precursors, where both metal and chalcogen precursors are placed upstream and delivered and react downstream at an elevated temperature. (C) The ideal case where all precursors are supplied from outside the furnace with precisely control and react in gas phase at an elevated temperature in a furnace.

### ***Chemical Vapor Deposition (CVD)***

CVD has been the most widely used technique to grow TMDs films, in which both metal and chalcogen precursors transport and react in gas phase. The better control over both precursors, together with the high mobility of the gas-phase precursors allow for the synthesis of TMD films with high crystallinity. As illustrated schematically in Figure 1.7B, the chalcogen and metal precursors are placed in a heated furnace, with the

growth substrate placed either downstream or face-down on top of the metal precursor. Elemental chalcogens are commonly used as the chalcogen precursors.  $\text{MoO}_3$ ,  $\text{MoCl}_5$ , and  $\text{WO}_3$  are commonly used as the metal precursors. Various TMDs can be synthesized using this CVD technique, including  $\text{MoS}_2$  [54–58],  $\text{WS}_2$  [59, 60],  $\text{MoSe}_2$  [61, 62],  $\text{WSe}_2$  [63, 64],  $\text{MoTe}_2$  [65], and  $\text{WTe}_2$  [66].

Due to the difference in reactivity, volatility, and chemical properties of different solid precursors [67], different TMDs are usually synthesized under distinct temperatures (for example, 700 °C [55] for  $\text{MoS}_2$  and 900 °C for  $\text{WS}_2$  [59]) or concentrations of reducing gas  $\text{H}_2$  (much higher for selenides and tellurides compared to sulfides [63]).

Although the abovementioned CVD technique has produced TMDs with higher crystallinity and better thickness control compared to the chalcogenization technique, the synthesis of uniform, continuous films over the wafer-scale is still challenging. One fundamental limit is the difficulty of maintaining a steady and precise supply of the precursors during the entire growth time—the onset of the vaporization and consumption of the precursors cannot be precisely controlled. Ideally, the synthesis of uniform TMDs should be done by a process in which the supply and reaction of precursors are controlled constant both spatially and temporally. The setup with such precise controls are schematically illustrated in Figure 1.7C and will be discussed in Chapter 3.

## ***Monolayer Heterostructure Synthesis***

The successful growth of monolayer TMD films over a large area requires the growth to happen in the edge attachment mode without multilayer formation—after the nucleation, individual grains only grow laterally in the monolayer plane, until they coalesce and form a continuous film. Monolayer heterostructures can be readily synthesized based on this mechanism by switching the growth environment for different TMD growth. Due to the drastically different environments (e.g. temperature, in-furnace solid precursors), synthesis of heterostructures with precisely controlled composition is challenging [68–71]. In addition, the frequent change in the growth environment (sometimes breaking the vacuum to switch the growth furnace) results in a high density of defects and voids at heterointerfaces.

### ***1.4 Thesis Preview***

TMDs provide the ideal materials for studying thin films in the ultimate, atomic-thickness limit. The composition variation of TMDs allows one to create monolayers with a variety of (opto-) electronic properties. Their unique band structures further give rise to new properties that are inaccessible in conventional semiconductors, for instance valleytronics. While researches based on materials produced by the unscalable mechanical exfoliation technique have shown the promise of these materials, the applications of the monolayer TMDs on the technologically relevant scale still poses two main challenges as discussed above in Section 1.1.

This thesis presents our efforts towards resolving these problems, which represents the material engineering in the monolayer limit, followed by using these monolayers as

building blocks for creating vertically-heterostructured thin films. In Chapter 2, we will first introduce the characterization techniques used throughout this thesis for compositional, structural, and electrical analysis of our monolayer TMDs. In Chapter 3, we will describe the synthesis of high-quality, wafer-scale uniform monolayer TMDs (*challenge i*). We will present the details on how we achieve the wafer-scale growth by developing a metal–organic chemical vapor deposition process and the high electrical performance of the grown films. In Chapter 4, we will discuss how we create coherent monolayer TMD superlattices (*challenge ii*), where 4% lattice mismatched TMDs are precisely controlled and laterally stitched without dislocations. The lattice coherence results in large strain that are used to precisely engineer the optical band gaps and mechanical deformation of TMD monolayers. Our monolayer TMD superlattice further presents a unique omnidirectional epitaxy system in contrast to conventional epitaxy, in which an isotropic change of lattice constant is observed. In Chapter 5, we discuss high-performance devices based on heterostructures of monolayer thickness, including semiconductor/semiconductor and semiconductor/metal heterojunctions that are enabled by the techniques discussed in Chapter 3 and 4. Finally, in Chapter 6, we show that TMD monolayers can serve as building blocks for creating vertically-stacked films containing both 2D materials and non-layered materials.

CHAPTER 2  
CHARACTERIZATION OF ATOMICALLY-THIN TRANSITION METAL  
DICALCOGENIDES

**2.1 Introduction**

Characterization is essential for providing information on a material based on which the synthesis can be improved. The characterization of monolayer TMDs is challenging as they are extremely thin and sensitive to damage compared to conventional 3D materials. Meanwhile, the large-scale monolayer films for applications usually span multi inches and are structurally complex due to the polycrystallinity. The mechanical, optical, and electrical properties of TMD films are largely determined by their compositional and structural properties. Rapid characterization techniques that provide information on composition, structure, and electrical properties of TMDs are critical for advancing TMD films towards application.

The thorough characterization of monolayer TMD films requires techniques that capture different properties of the monolayer TMDs across different length scales. Different characterization tools have their own benefits and drawbacks and are often utilized in a collective manner to gain thorough information on the TMD films. Standard characterization tools such as optical microscopes and scanning electron microscopes (SEMs) can be used to identify and provide initial topography information on TMD monolayers but fail to capture compositional and structural information. For the compositional characterization of TMDs, spectroscopy techniques such as Raman and photoluminescence (PL) spectroscopies are commonly employed. The (crystalline)

structures of TMD films on different length scales can be probed with transmission electron microscopy (TEM) techniques. Nevertheless, the composition and structure of TMDs interplay and often cannot be distinguished from one another by using only a single technique. Different techniques are commonly applied in a complementary manner to provide full characterization of TMD films over several critical length scales.

In this chapter we will describe the major techniques used throughout this thesis for characterizing our TMD films. These techniques are categorized by their purpose—for compositional, structural, and electrical characterization. In the following sections, we will first introduce the most used optical microscopy tool for the identification of TMDs, followed by Raman/PL spectroscopy and imaging for compositional analysis of TMDs. We then describe the structural characterization of TMDs using various TEM techniques. Lastly, we discuss the electrical device characterizations of TMDs using the field effect transistor (FET) configuration.

## ***2.2 Optical Microscopy Identification of TMDs***

Synthesized TMDs can contain empty, monolayer, bilayer and multilayer regions which span length scales on the order of inches (A representative optical micrograph shown in Figure 2.1B). A rapid method that identifies and locates TMDs is indispensable to examine the quality of such large-scale films and provide feedback for the synthesis. Optical methods are most suitable for such a purpose. Mono- and few-layer TMDs can absorb up to a few percent of incident light in the visible range, making them visible even on transparent substrates [72, 73]. The reflection from the TMDs can be further enhanced greatly by engineering the dielectric environment of the underlying

substrate. Figure 2.1A illustrates different viable paths for light reflection at different interfaces for TMDs on the most commonly used substrate, thermally oxidized Si. According to theoretical calculations, a significant contrast as high as 80% between monolayer MoS<sub>2</sub> and empty region on SiO<sub>2</sub>/Si substrate can be achieved with a specific choice of oxide thickness and illumination wavelength (Figure 2.1C) [74]. Under white light illumination, silicon wafers with either 78 nm or 272 nm SiO<sub>2</sub> show the highest contrast (Figure 2.1D). As a result, the standard 285 nm SiO<sub>2</sub>/Si are often used as the substrate for TMDs. TMDs with different layer numbers can also be readily differentiated from each other, especially on the 285 nm SiO<sub>2</sub>/Si substrates (Figure 2.1B, substrate, monolayer, and bilayer regions marked).

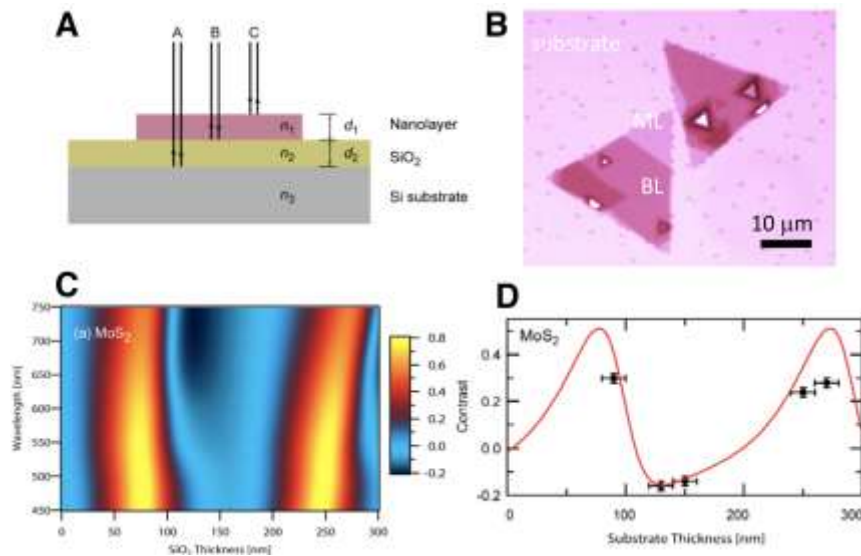


**Figure 2.1 Optical contrast of TMDs on SiO<sub>2</sub>/Si substrates.**

(A) Schematic of optical reflection and transmission for TMD with thickness  $d_1$  and complex index of refraction  $n_1$  on an SiO<sub>2</sub> layer with thickness  $d_2$  and index of refraction  $n_2$  on top of a Si substrate. (B) An optical micrograph of synthesized MoS<sub>2</sub> on a 285 nm SiO<sub>2</sub>/Si substrate where empty, mono-, bi-, and multi-layer regions can be easily distinguished. (C) Color plot of calculated contrast as a function of incident light wavelength and SiO<sub>2</sub> layer thickness for MoS<sub>2</sub>. (D) Calculated contrast values for MoS<sub>2</sub> on SiO<sub>2</sub> substrates with varying thicknesses. Curve represents contrast for broadband illumination and detection using the green channel (495–530 nm) of a color camera. Black dots are experimental data points. A, C, and D reproduced from [74].

The quick turnaround of TMD synthesis and identification expedites the optimization of the synthesis and provides important information for characterization in depth. While there exist a variety of characterization techniques that provide information inaccessible otherwise, optical microscopy remains the most often used technique to inspect TMDs.

### ***2.3 Compositional Characterization with Optical Spectroscopies***

Optical spectroscopy techniques are widely used to study TMDs, as they are rapid and non-destructive. Fundamentally, optical spectroscopy probes the electronic and phononic structure of a material, which is determined by the composition and lattice structure. Here in this section, we will focus on the applications of optical spectroscopies for compositional characterization.

#### ***Photoluminescence Spectroscopy***

Photoluminescence is light emission from any material after the absorption of photons. The PL spectra of a semiconducting material depends on its electronic band structure. For example, the energy of emitted photons is usually higher for material with a larger band gap. Monolayer TMDs are of particular interest, partially due to their direct band gaps. As a result, the PL quantum yields of monolayers are orders of magnitudes higher than that of the multilayer counterparts (Figure 1.4B). As an example, the fundamental band gap in bulk MoS<sub>2</sub> is an indirect transition from the top of the valence band at  $\Gamma$  point to the bottom of the conduction band located between the  $\Gamma$  and K points (Figure 2.2A) [3]. The orbital contribution of to the electronic states in monolayer TMDs is shown in Figure 2.2, B-C. The electronic states of the band maxima at K point

mainly consist of M- $d_{x^2-y^2}$ ,  $d_{xy}$ ,  $d_z$ , and X- $p_x$ ,  $p_y$  orbitals, whereas the states of the valence band top at  $\Gamma$  point, the X- $p_z$  contribution become significant [75, 76]. Such orbital contributions lead to two important properties of TMDs. First, as the layer number decreases, the interlayer interaction between X- $p_z$  state at the valence band at  $\Gamma$  point change substantially, while the interactions of other states (e.g. at K points) barely changes, which leads to the transition from indirect to direct band gap in the monolayers. Second, the strong contribution of the M- $d_{xy}$ ,  $d_z$ , and X- $p_x$ ,  $p_y$  orbitals at K point valence band lead to the large spin splitting, which is critical for the valley dependent optical [23, 24, 26, 28–30, 77] and electrical [5, 24, 25] properties of these materials.

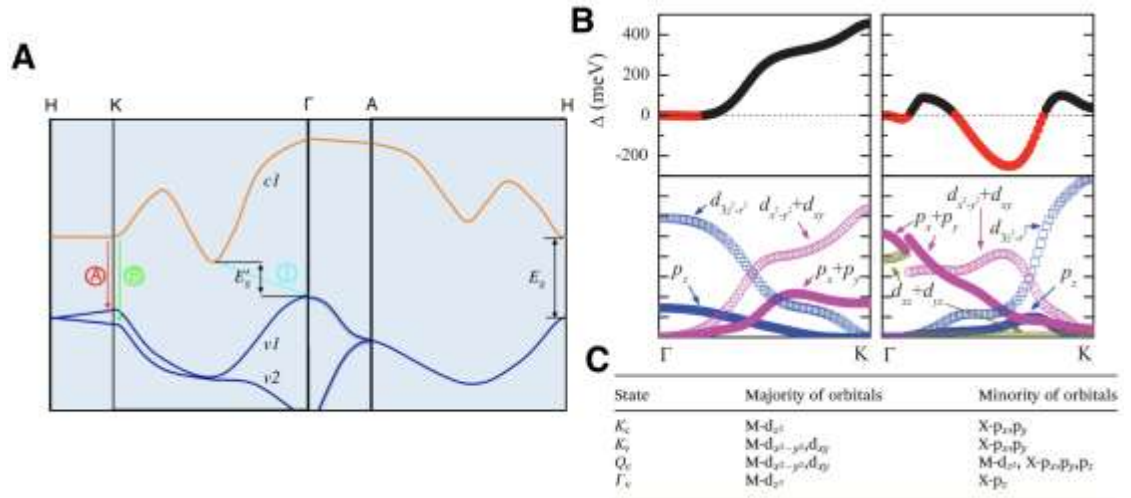


**Figure 2.2 Band structure and orbital contributions to electronic states of TMDs.** (A) simplified band structure of bulk MoS<sub>2</sub>, showing the lowest conduction band  $c1$  and the highest split valence bands  $v1$  and  $v2$ . A and B are the direct-gap transitions, and I is the indirect-gap transition.  $E'_g$  is the indirect gap for the bulk. Reproduced from [3]. (B) (Top) Spin splitting along the  $\Gamma$ -K line; and (Bottom) orbital contributions of W and Se of WSe<sub>2</sub>. (Left) uppermost valence band (Right) lowermost conduction band. Reproduced from [75]. (C) Orbital composition of monolayer TMDs at several points. Reproduced from [76].

The three optical transitions are summarized in Figure 2.2A. Three corresponding peaks can be observed in multilayer samples (representative PL spectra of WS<sub>2</sub> and

WSe<sub>2</sub> shown in Figure 2.3) [78]. When the layer number decreases to monolayer, the most fundamental transition A (A exciton) dominates the PL signal in monolayer TMDs. The A exciton peak position ranges from visible to near infrared, depending on the chemical composition especially the chalcogens. The room-temperature PL spectra acquired from exfoliated monolayer TMDs have been used as the standard to which synthesized monolayers are compared. We also note the composition is not the only factor that determines the PL spectra of TMD monolayer. In fact, doping level and strain, among other factors, can also change the PL peak position of a TMD monolayer. Nonetheless, with proper control of the sample, PL spectroscopy provides an effective method to examine the composition of TMDs and differentiate the monolayers from the multilayers.

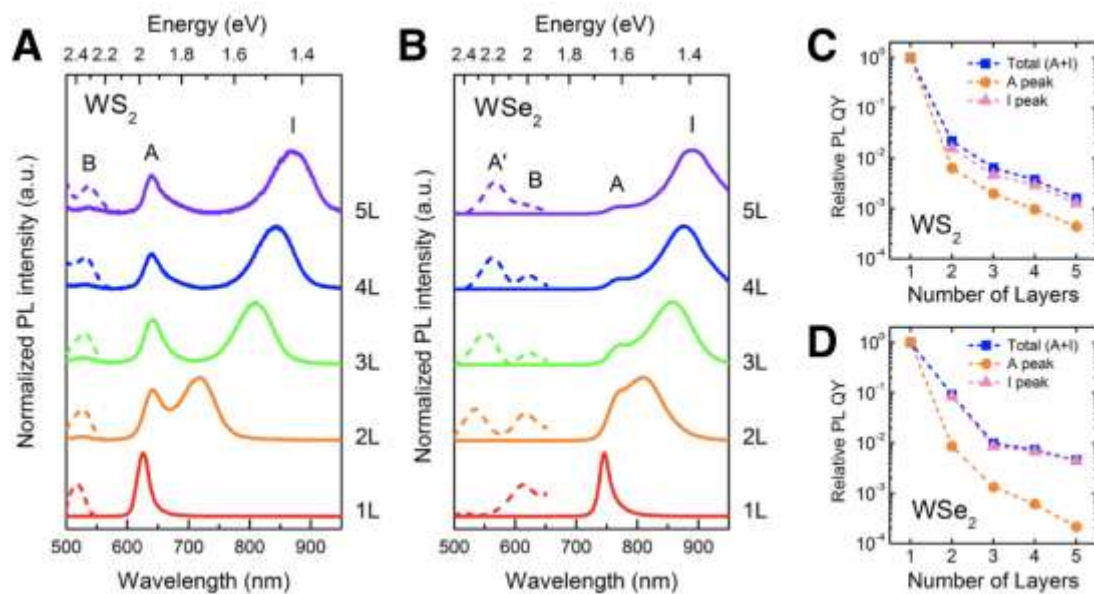


**Figure 2.3 PL spectra of WS<sub>2</sub> and WSe<sub>2</sub>.**

(A-B) Normalized PL spectra of mechanically exfoliated (A) 2H-WS<sub>2</sub> and (B) 2H-WSe<sub>2</sub> flakes consisting of 1–5 layers. Peak I is an indirect gap emission. Weak hot electron peaks A' and B are magnified and shown as dashed lines for clarity. These hot electron

peaks are typically 100 to 1000 times weaker than the band edge emission peaks. The total emission intensity becomes significantly weaker with increasing number of layers. (C-D) Relative decay in the PL quantum yield with the number of layers for (C) WS<sub>2</sub> and (D) WSe<sub>2</sub>. The values are relative to the PL quantum yield of a monolayer flake as discussed in the text. The plots are shown for A and I peaks and their sum (A+I). Reproduced from [78].

### Raman Spectroscopy

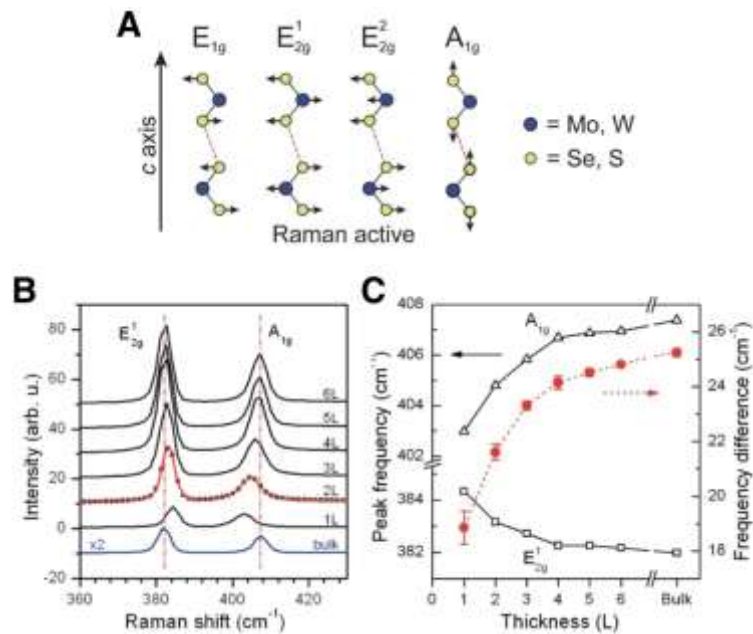


**Figure 2.4 Raman modes and spectra of TMDs.**

(A) Schematics of active Raman modes of TMDs. Reproduced from [79]. (B) Raman spectra of thin and bulk MoS<sub>2</sub> films. The solid line for the bilayer spectrum is a double Voigt fit through data (circles for bilayer, solid lines for the rest). (C) Frequencies of E<sub>2g</sub><sup>1</sup> and A<sub>1g</sub> Raman modes (left vertical axis) and their difference (right vertical axis) as a function of layer thickness. Reproduced from [80].

Raman spectroscopy, a technique based on the inelastic scattering of light by phonons in a material is widely used to characterize the composition and structure of materials. Because the phonon spectra (i.e. the vibration modes) strongly depend on the composition and thickness, Raman spectroscopy is an effective tool for characterizing the composition and layer number of TMDs.

According to group theory analysis, there are four Raman active mode for TMD (point group  $D_{6h}$ )—three in-plane  $E_{1g}$ ,  $E_{2g}^1$ , and  $E_{2g}^2$ , and one out-of-plane  $A_{1g}$  mode (Figure 2.4A) [79, 81]. In a typical Raman measurement configuration where the backscattered signal is collected, the  $E_{1g}$  mode is forbidden according to the Raman selection rules [82]. The  $E_{2g}^2$  mode is of low frequency ( $< 50 \text{ cm}^{-1}$ ), and hence is difficult to resolve except in a carefully designed system [83, 84]. In our experiments, we mainly focus on the two accessible Raman  $E_{2g}^1$  and  $A_{1g}$  modes.

The frequency and intensity of the Raman  $E_{2g}^1$  and  $A_{1g}$  modes of TMDs are affected by the layer number (Raman spectra of  $\text{MoS}_2$  shown in Figure 2.4, B-C). The  $A_{1g}$  peak shows a stronger dependence on the layer number as expected by its out-of-plane nature. The frequency of  $A_{1g}$  increases as the layer number increases due to the stiffening caused by the interlayer van der Waals interactions [80]. On the other hand, the frequency of the  $E_{2g}^1$  mode decreases which is the result of the stiffening due to the increased dielectric screening of the interlayer Coulomb interaction and stacking-induced change in the interlayer interactions [85]. This monotonic dependence of Raman frequencies on the material thickness can be used to characterize the layer number of TMDs.

### ***Widefield Imaging***

Most optical spectroscopic characterization of TMDs are performed in the confocal configuration. To gain spatial information, the focused laser beam is scanned through the sample, point by point, which is time consuming. As discussed above, the PL and Raman spectra of a specific TMD of interest usually show peaks only at certain energies

in the spectrum. Thus, in the scanning confocal measurements, a large portion of the spectrum acquisition time is spent on regions that are not of interest, making it inefficient for spatial characterization of homogeneous films. A solution to the issue of time-consuming spatial characterization is to use widefield microscopy, where we collect photons of certain energies from the sample which is under widefield illumination (Figure 2.5) [86]. In such scheme, we sacrifice the energy resolution and gain spatial resolution in return.

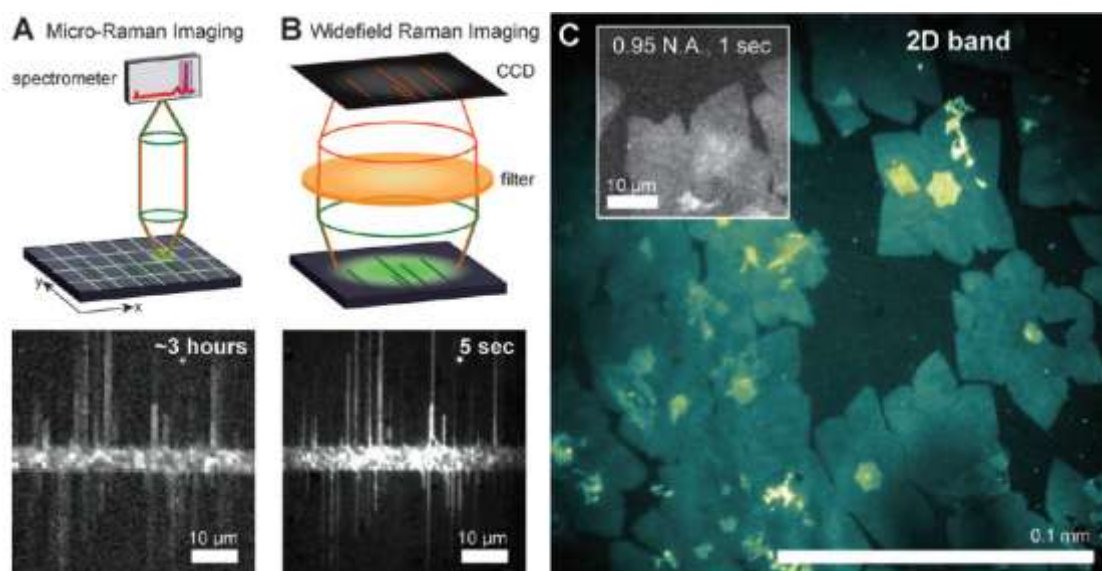


**Figure 2.5 Widefield imaging based on Raman or photoluminescence.**

(A) Conventional imaging of a carbon nanotube sample using a scanning confocal microscope. (B) Widefield imaging setup and Raman image of similar sample in (A). (C) False color image of the 2D-band for a sample of graphene (bright areas). Reproduced from [86].

Widefield techniques can be effectively used to characterize the spatial uniformity of TMD films with single or multiple compositions. In order to do this, proper filters are used to select photons of specific energies and to generate spatial maps of peak intensity with diffraction-limit resolution. Widefield techniques can be 100-fold more time-efficient than conventional scanning confocal setups, for generating spatial

intensity maps (Figure 2.5). In addition, the widefield image can have a submillimeter scale field of view, making it ideal for characterizing large scale TMD films.

## ***2.4 Structural Analysis with Transmission Electron Microscopy***

TEM is an ideal technique for characterizing 2D materials, especially the crystallinity information, on a scale ranging from micrometers to angstroms. In a TEM measurement, a high-energy electron beam passes through the sample and scatters both elastically and inelastically with it. Analyzing the electron beam after different scattering processes can provide information on the sample's structure. For example, the elastically diffracted beams can reveal the crystalline structure of the sample, and the energy loss to inelastic scattering processes can disclose the composition of the sample. Depending on the illumination configuration, TEM can work in either conventional TEM mode or scanning TEM (STEM) mode. In TEM mode, a sample of interest is illuminated, and electron diffraction patterns (DPs) and bright-field (BF) and dark-field (DF) images can be recorded using a camera. In STEM mode, the electron beam is focused into a spot of sub-nanometer size, and by scanning the beam through the sample, the scattered electrons can be recorded as a function of the beam position with atomic resolution. Elastically scattered electrons are collected by an annular dark-field (ADF) detector, displaying contrast according to the atomic number. Inelastically scattered electrons are collected simultaneously with the ADF signal, which provides compositional and bonding information according to the electron energy-loss spectroscopy (EELS). A combination of these different TEM techniques allows sample characterization across length scales spanning several orders of magnitudes from

micrometers to angstroms. As a result, TEM has been widely used to study the structure of various 2D materials.

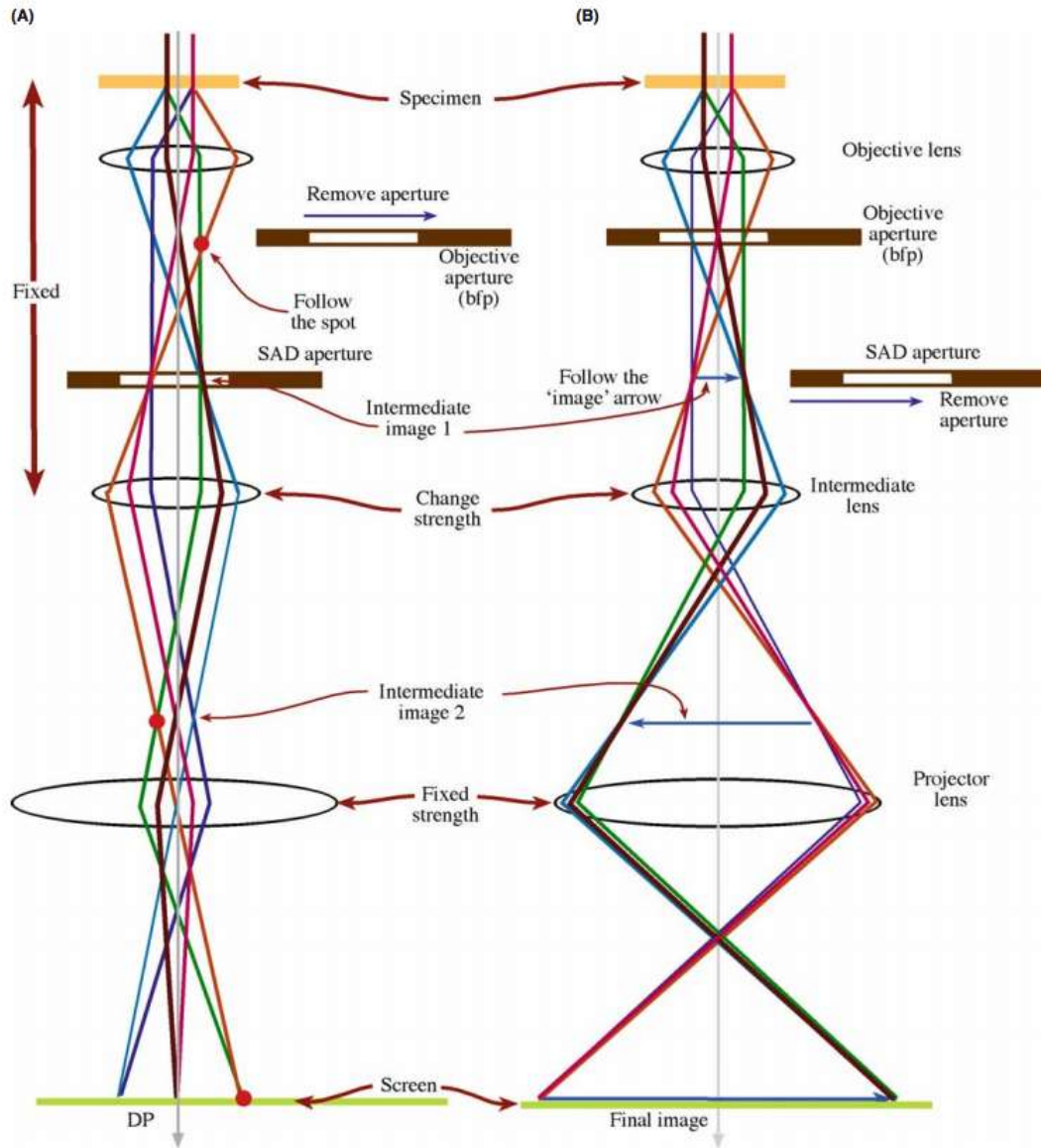


**Figure 2.6 Diagram of TEM diffraction and imaging modes.**

(A) TEM diffraction mode: projecting the DP onto the viewing screen or camera. (B) Image mode: projecting the image onto the screen or camera. Reproduced from [87].

### *Electron Diffraction and Dark-Field TEM*

When interacting with crystalline materials, electrons can be diffracted by the periodic lattice of the crystal. The change in momentum of the electron resembles the

reciprocal lattice of the crystal. Therefore, diffraction-based techniques can be used to identify the lattice structure of crystalline materials. Figure 2.6 shows the ray diagrams of TEM in diffraction mode and imaging mode. First, the orientation of the DP can be used to determine the crystal orientation of the TMD, which is often referred to as the zigzag or armchair directions. Second, the position of the diffraction spots is determined by the real-space lattice constants. Smaller lattice spacing can result in larger DP separation in the corresponding direction. Third, the intensity is determined by the unit cell structure, which is particularly useful for dark field imaging [55, 88].

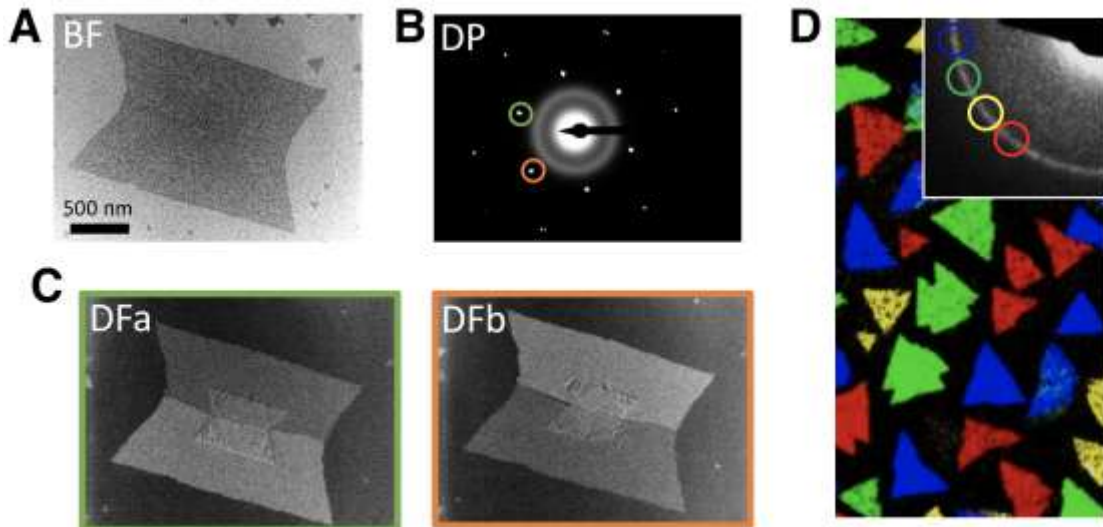


**Figure 2.7 DF-TEM imaging of monolayer TMDs.**

(A) Bright field image of a twin structure of monolayer in-plane  $\text{WS}_2$  and  $\text{WSe}_2$  heterostructure. (B) The diffraction pattern of the TMD sample in (A). (C) Corresponding DF-TEM images based on the selected spots in (B). (D) False-color DF-TEM image of polycrystalline  $\text{MoS}_2$ .

To take DPs of TMDs, the sample of interest is first identified in the bright field mode (Figure 2.7A), then a selected area (SA) aperture of proper size is inserted to block beams outside the aperture to prevent diffraction from irrelevant flakes. A set of hexagonal diffraction spots can be observed for single crystalline TMDs. To take a DF

image, a specific diffraction spot is selected using an objective aperture (Figure 2.7B, color circles), while keeping other TEM optics the same with BF mode (Figure 2.7C). In this example, a twin structure of monolayer in-plane WS<sub>2</sub> and WSe<sub>2</sub> heterostructure is being imaged, where the upper grain is rotated by 180° with respect to the bottom grain. The different intensities in the twin structure results from the asymmetry of the unit cell structure of the monolayer TMD, and the contrast is determined by the polarity of unit cell: WSe<sub>2</sub> (core) gives less contrast due to the lower polarity compared to WS<sub>2</sub> (edge) [55, 89]. DF-TEM is particularly useful for imaging polycrystalline samples [88]. When there are many arbitrarily oriented grains in the field of view, the DP will show a continuous ring instead of a single hexagonal pattern (Figure 2.7D, inset). By selecting different parts of the diffraction ring with a series of objective apertures followed by color coding the DF images, a composite false-color DF image, where the different colors indicate the grain orientation, can be obtained (Figure 2.7D). Due to its operational simplicity, DF-TEM is widely used for characterizing the micrometer-scale crystalline structure of TMD films.

### ***Scanning Transmission Electron Microscope (STEM)***

While conventional TEM can provide information on the crystalline structure of TMD on a relatively large scale, it is less effective at atomic resolution which can be critical in various instances. One example is for the characterization of the atomic arrangements at grain boundaries, which can be deterministic to the electrical properties of TMD films. Aberration-corrected annular dark-field scanning transmission electron microscopy (ADF-STEM) enables the atomically-resolve imaging of the lattice of 2D

materials [90]. In the high angle regime where the collection angle is three-time or more greater than the convergence of the angle of the incident beam, the scattering intensity is roughly proportional to  $Z^\gamma$ , where  $Z$  is the atomic number and  $1.3 < \gamma < 2$  [91]. Figure 2.8B shows ADF-STEM images of  $\text{MoS}_2$  in a single-crystal region and at a tilt boundary region. Together, TEM and STEM are complementary techniques that can be combined to study the lattice structure of TMDs on many critical length scales that determines the properties of these TMD films.

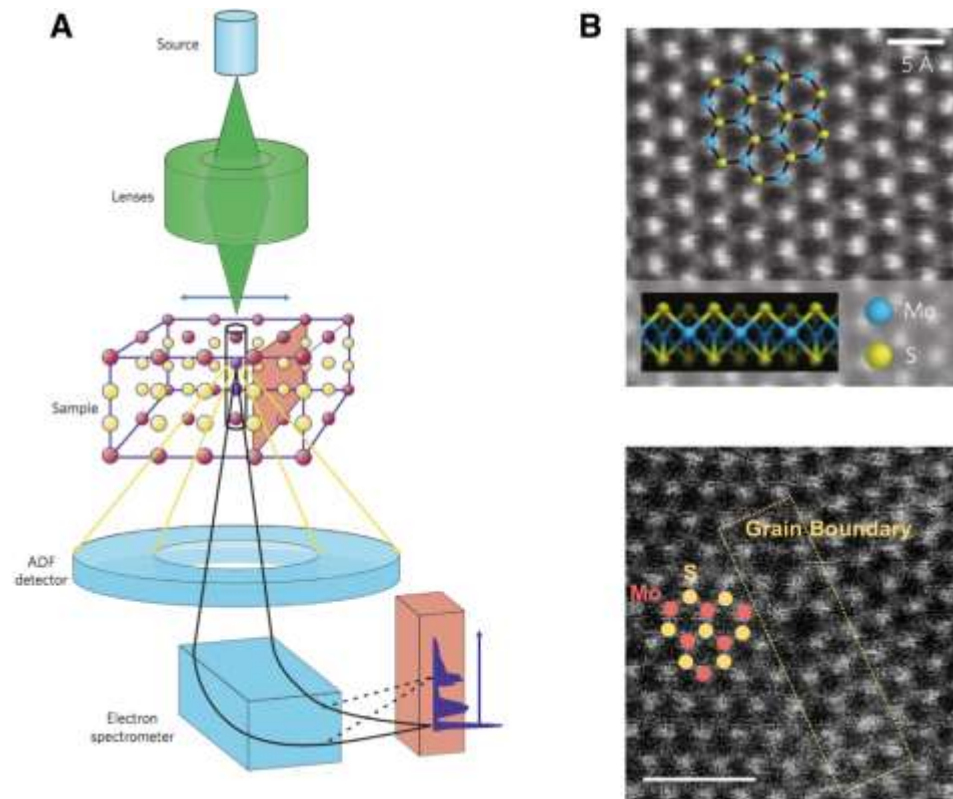


**Figure 2.8 Schematic of STEM and ADF-STEM images of  $\text{MoS}_2$ .**

(A) Schematic of the major elements of a scanning transmission electron microscope. Reproduced from [92]. (B) ADF-STEM image of  $\text{MoS}_2$  in the single crystalline region (top) and laterally stitched grain boundary region (bottom). Reproduced from [55, 93].

### ***Electron Energy-Loss Spectroscopy (EELS)***

Besides the “Z contrast” imaging by ADF-STEM, rich information on the composition and bonding of materials can be obtained by analyzing the EELS of inelastically scattered electrons (Figure 2.8A). The inelastically scattered electrons are collected simultaneously with the ADF signal and are analyzed by an electron spectrometer, which separates electrons according to their energy loss. In inelastic scattering processes, the incident electrons lose energy to the electrons in the sample. For example, the incident electrons can excite the electrons from inner-shell states to unoccupied states above the Fermi level of the material. These excitations correspond to unique energy losses for different elements and can be used to determine the composition of a material. Altogether, STEM is a powerful technique for acquiring information on lattice structure and compositions with atomic resolution.

### ***Electron Microscope Pixel Array Detector (EMPAD)***

For some characterizations (e.g. defect identification in a micrometer-sized TMD), it is necessary to map out the atomic structure over the entire sample. The STEM technique mentioned above appears impractical in such cases because of the small field of view (typically  $< 100$  nm). For this purpose, we utilized a newly-developed electron microscope pixel array detector (EMPAD) for STEM imaging. The EMPAD with  $128 \times 128$  pixels provides a 1,000,000:1 dynamic range, which allows the recording of the direct electron beam, while still maintaining single electron sensitivity [94]. In a EMPAD experiment, the beam is focused on (for example with a 0.5 mrad convergence angle) and scanned across the TMD sample, and the diffraction patterns at every

position in real space are recorded to build up a 4-dimensional data set (Figure 2.9A) [95]. The high dynamic range of EMPAD enables collection of all transmitted electrons at small convergence angles with the primary beam unsaturated and diffracted beams clearly resolved (Figure 2.9B). Real space mappings can be constructed by integrating different diffraction spots, for example the virtual bright field image (Figure 2.9C, by integrating the center spot) and dark field image (Figure 2.9D, by integrating one of the diffracted spot).

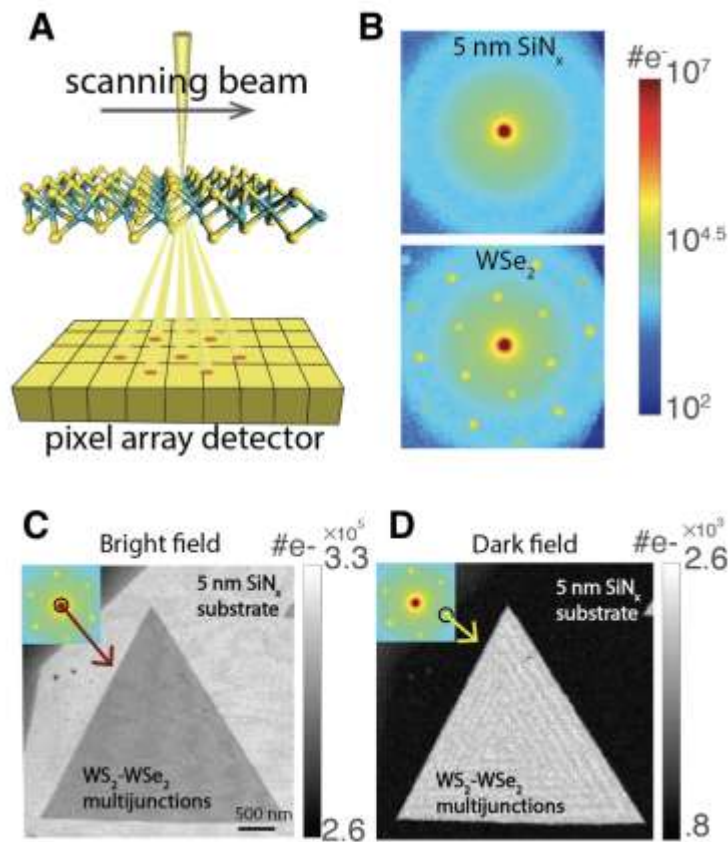


**Figure 2.9 EMPAD imaging of monolayer TMDs.**

(A) Schematic of the EMPAD operation, where a full diffraction pattern, including the unsaturated primary beam, is recorded at each scan position. (B) Diffraction images taken by EMPAD. The top panel shows the diffraction image of a 5 nm SiN<sub>x</sub> film, while the bottom panel displays the diffraction pattern of a WSe<sub>2</sub> monolayer located on the 5 nm SiN<sub>x</sub> film. (C-D) The virtual bright field (C) and filtered dark field (D) images obtained by integrating the central and the labeled diffracted beam, respectively, as indicated in their top left insets. Reproduced from [95].

The EMPAD with high-speed, high dynamic range, and high sensitivity allows fast data acquisition within minutes, which minimizes the electron beam damage to the atomically-thin samples. EMPAD provides lattice structure mapping with sub-picometer precision over length scales ranging from angstroms to many micrometers, presenting an extremely powerful technique for characterizing various TMDs [96].

## 2.5 *Electrical Characterizations*

In order to characterize the electrical properties of a material, one has to connect it to an external measurement setup, often with probes. Due to the thinness of 2D TMDs, bulk metals are often used as electrodes for connecting the TMDs and measurement circuits. In this thesis, the majority of electrical characterization is performed in the field effect transistor (FET) configuration [97]. There are three terminals in a FET device: source, drain, and gate(s). In a monolayer TMD FET (Figure 2.10), the spatially-defined TMD forms the channel between the source and drain, and the carriers are injected into the channel from the source and collected at the drain [36]. The current that runs through the channel from the source and collected at the drain [36]. The current that runs through the device (i.e. the conductance) can be modulated by applying gate voltages. Two important parameters that characterize the performance of FET devices are field-effect mobility and on-off ratio. The field-effect mobility (simply referred to as mobility) describes how fast the carrier movement can be modulated by the electric field, and is defined as  $\mu_{FE} = \frac{L}{W C_g} \times \frac{dG}{dV_g}$ , where  $C_g$  is the capacitance of the gate dielectric per unit area,  $L$  is the length of the channel,  $W$  is the width of the channel,  $G$  is the conductance of the device, and  $V_g$  is the backgate voltage applied. The on-off ratio is defined by the ratio between the on-state conductance and off-state conductance of the device.

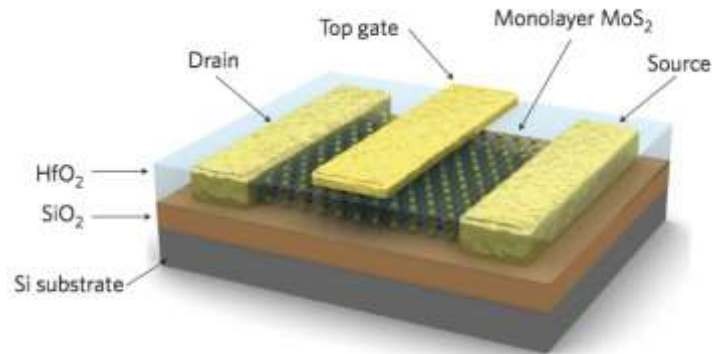


**Figure 2.10 Schematic of a monolayer MoS<sub>2</sub> FET.**

Schematic of a MoS<sub>2</sub> FET with both global Si backgate and local top gate using HfO<sub>2</sub> as the dielectric. Reproduced from [36].

Both bottom gate and top gate can simultaneously function in a FET device, and high- $\kappa$  dielectric materials are commonly used to enhance the gating efficiency of FET devices. In this thesis, all devices are fabricated with standard photolithography and e-beam lithography in combination with thin film deposition techniques. Using the FET configuration, heterostructure devices in which the channel materials are electrically inhomogeneous can also be measured. Examples include TMD/TMD p-n junctions and graphene/TMD junctions which will be discussed in detail in Chapter 5.

## 2.6 Summary

In this chapter, we introduced the characterization techniques that are used throughout the rest of this thesis. These techniques are used in combination in order to study the correlation between different properties. For example, a TMD sample with low defect density often results in high mobility. The rich information acquired by these characterization techniques provides valuable information based on which the synthesis is improved.



## CHAPTER 3

### HIGH-MOBILITY MONOLAYER TRANSITION METAL DICHALCOGENIDES WITH WAFER-SCALE HOMOGENEITY

#### ***3.1 Introduction***

The large-scale growth of semiconducting thin films is the basis of modern electronics and optoelectronics. Reducing film thickness to the ultimate, sub-nanometer length scale, a difficult limit for traditional semiconductors (e.g. Si and GaAs), would greatly benefit for applications in ultrathin and flexible electronics, photovoltaics and display technology [98–100]. For this, transition metal dichalcogenides (TMDs), which can form stable three-atom-thick monolayers (MLs) [101], provide ideal semiconducting materials with high electrical carrier mobility [102–107]. Their large-scale growth on insulating substrates would enable batch fabrication of atomically-thin high-performance transistors and photodetectors on a technologically relevant scale without film transfer. In addition, their unique electronic band structures provide novel ways to enhance the functionalities of such devices, including the large excitonic effect [4], bandgap modulation [108], indirect-to-direct bandgap transition [3], piezoelectricity [6] and valleytronics [5]. However, the large-scale growth of ML TMD films with spatial homogeneity and high electrical performance remains an unsolved challenge.

Existing growth methods for large-scale ML TMDs have so far produced materials with limited spatial uniformity and electrical performance. For instance, the sulfurization of metal or metal compounds only provides control over the average layer number, producing spatially-inhomogeneous mixtures of monolayer, multilayer, and

no-growth regions [49, 50]. While chemical vapor deposition (CVD) based on solid-phase precursors (such as  $\text{MoO}_3$ ,  $\text{MoCl}_5$ , or  $\text{WO}_3$ ) [54–59] has demonstrated better thickness control over the large scale, the electrical performance of the resulting material, which is often reported from a small number of devices in selected areas, fails to show spatially uniform high carrier mobility.

In this chapter, which is largely adapted from Ref. 98, we present high-mobility, 4-inch wafer-scale films of ML molybdenum disulfide ( $\text{MoS}_2$ ) and tungsten disulfide ( $\text{WS}_2$ ), directly grown on insulating  $\text{SiO}_2$  substrates, with excellent spatial homogeneity over the entire films. They are grown using a newly developed metal-organic chemical vapor deposition (MOCVD) technique, and show high electrical performance, including an electron mobility of  $30 \text{ cm}^2/\text{Vs}$  at room temperature and  $114 \text{ cm}^2/\text{Vs}$  at 90 K for  $\text{MoS}_2$ , with little position or channel-length dependence. Using these films, we successfully demonstrate the wafer-scale batch fabrication of high-performance ML  $\text{MoS}_2$  field effect transistors (FETs) with a 99% device yield.

### ***3.2 Monolayer TMD Films with Wafer-Scale Uniformity***

Figure 3.1 presents our continuous TMD ML films and shows their wafer-scale homogeneity and intrinsic optical properties. The color photos of  $\text{MoS}_2$  (Figure 3.1A; greenish yellow) and  $\text{WS}_2$  (Figure 3.1B; yellow) films grown on a transparent 4-inch fused silica wafer show that the TMD grown region (right half) is uniform over the whole substrate and clearly distinguishable from the bare silica substrate (left half). The optical absorption, photoluminescence (PL), and Raman spectra measured from our films show characteristics unique to ML  $\text{MoS}_2$  and  $\text{WS}_2$ , respectively (Figure 3.1, C-E).

All of these measured spectra have the same peak positions as in exfoliated ML samples (denoted by diamonds) [72, 78, 109, 110], regardless of the location of the measurements within our films (Figure 3.1F). The X-ray photoelectron spectra (XPS) taken from our ML MoS<sub>2</sub> film show almost identical features as in bulk single crystal with low level of defects, further confirming the precise chemical composition and the high quality of our MoS<sub>2</sub> film (Figure 3.1G).

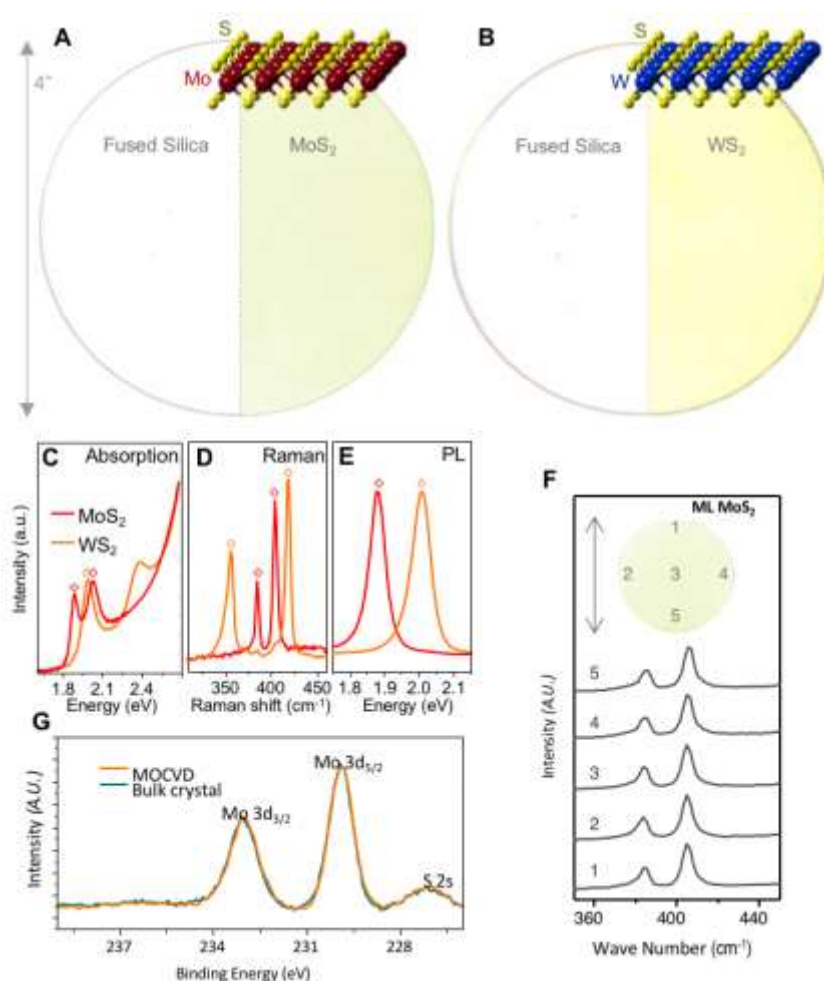


**Figure 3.1 Wafer-scale monolayer TMD films.**

(A-B) Photo of ML MoS<sub>2</sub> (A) and WS<sub>2</sub> (B) film grown on 4-inch fused silica substrate with schematics for their respective atomic structure. Left half shows bare fused silica substrate for comparison. (C) Optical absorption spectra of MOCVD grown ML MoS<sub>2</sub> (red line) and WS<sub>2</sub> (orange line) films in the photon energy range from 1.6 to 2.7 eV. (D) Raman spectra of as-grown ML MoS<sub>2</sub> and WS<sub>2</sub>, normalized to the silicon peak

intensity. (E) Normalized photoluminescence (PL) spectra of as-grown ML MoS<sub>2</sub> and WS<sub>2</sub>. The peak positions are consistent with those seen from exfoliated samples, denoted by diamonds, same for (C-E). (F) Raman spectra for MoS<sub>2</sub> taken at different locations marked on the corresponding fused silica wafer. (G) XPS spectra of Mo 3d 3/2, 5/2 and S 2s state for MoS<sub>2</sub> grown by our method (orange) and bulk MoS<sub>2</sub> single crystal (cyan blue), where the peak position and FWHM are almost identical.

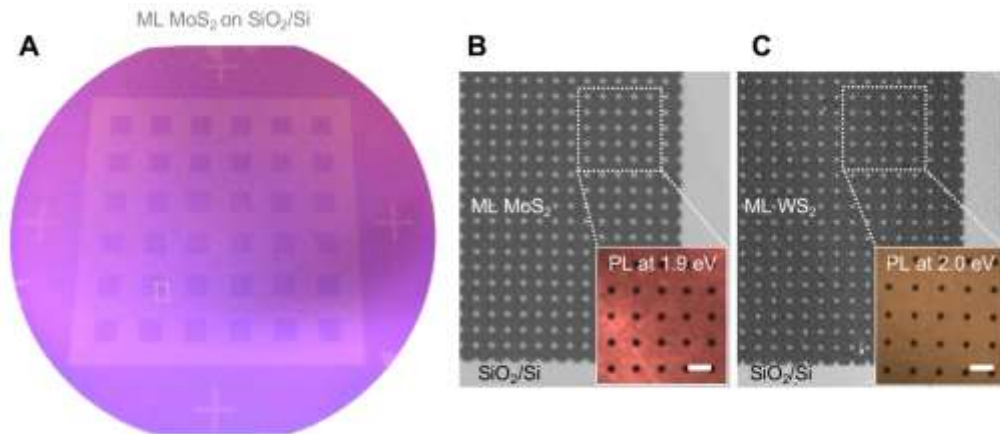


**Figure 3.2 Uniform PL of patterned monolayer TMD films.**

(A) Photo of patterned ML MoS<sub>2</sub> film on 4-inch SiO<sub>2</sub>/Si wafer (the darker areas are covered by MoS<sub>2</sub>). (B-C) Optical images (normalized to the bare substrate region) and PL images (inset, at 1.9 eV for MoS<sub>2</sub> and 2.0 eV for WS<sub>2</sub>) of patterned ML MoS<sub>2</sub> and WS<sub>2</sub>, respectively on SiO<sub>2</sub>, taken from the wafer scale patterned films. Scale bar, 10  $\mu$ m.

Figure 3.2A shows a photo of a MoS<sub>2</sub> film grown on a 4-inch SiO<sub>2</sub>/Si wafer. The ML film was patterned using standard photolithography and oxygen plasma etching to form MoS<sub>2</sub> covered squares (dark, 6 mm wide) with an array of 3  $\mu$ m holes. A zoomed-in, normalized optical reflection image (Figure 3.2B) displays a homogeneous reflection contrast for the entire MoS<sub>2</sub> covered region, confirming uniform ML growth everywhere with no gaps. The widefield PL images of these films show strong, spatially uniform PL signals, further confirming that they are continuous ML MoS<sub>2</sub>, with its high quality maintained even after patterning or transfer. The same spatial uniformity was seen in the optical reflection and PL images of a ML WS<sub>2</sub> film that was similarly grown and patterned (Figure 3.2C). Together, the optical data confirm that our MoS<sub>2</sub> and WS<sub>2</sub>

films are continuous MLs, spatially uniform over the entire 4-inch growth substrates with intrinsic optical properties.

### 3.3 Metal-Organic Chemical Vapor Deposition for Monolayer TMDs

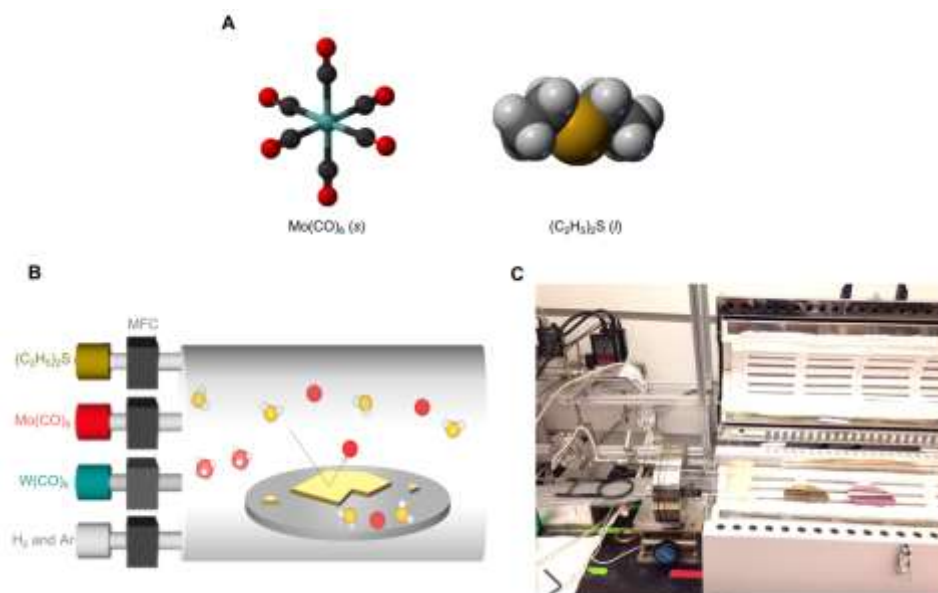


**Figure 3.3 MOCVD for monolayer TMDs.**

(A) Schematics of high-vapor pressure metal organic precursors. (B-C) Schematic (B) and photo (C) of our MOCVD growth setup. Precursors are introduced to the growth setup using individual mass flow controllers (MFCs). Red sphere = Mo or W atom, yellow = S, white = carbonyl or ethyl ligands.

As illustrated in Figure 3.3, the synthesis of ML MoS<sub>2</sub> and WS<sub>2</sub> was carried out in a 4.3-inch (inner diameter) hot-wall quartz tube furnace. Molybdenum hexacarbonyl (MHC), tungsten hexacarbonyl (THC), diethyl sulfide (DES), which have high equilibrium vapor pressure near room temperature, are selected as chemical precursors for Mo, W, S, respectively, and introduced to the furnace in gas phase. H<sub>2</sub> and Ar are injected to the chamber using separate lines.

The concentration of each reactant can be precisely controlled during the entire growth time by regulating the partial pressure (P<sub>x</sub>) of each reactant (X). Thus, our setup

offers an ideal environment for maximizing the areal coverage of the ML, and for engineering the film structure by controlling the nucleation density and intergrain stitching. The optimum growth parameters for ML MoS<sub>2</sub> and WS<sub>2</sub> films are as follows. We use a total pressure of 7.5 Torr, growth temperature of 550 °C and growth time ( $t_0$ ) of 26 hrs. The flow rates of precursors are 0.01 sccm for MHC or THC, 0.4 sccm for DES, 5 sccm for H<sub>2</sub>, and 150 sccm for Ar, which were regulated by individual mass flow controllers (MFCs). The low flow rates were used for MHC, THC and DES for the layer-by-layer growth mode. The long growth time ( $t_0 \sim 26$  hrs) is necessary for full ML growth, because of the low growth rate in this regime. NaCl is loaded in the upstream region of the furnace as a desiccant to dehydrate the growth chamber, which significantly increases the grain size, as discussed as below.

### ***3.4 Layer-by-Layer Growth and Grain Size Control***

#### ***Layer-by-Layer Growth***

Our MoS<sub>2</sub> film is grown in the layer-by-layer growth mode, which is ideal for the uniform layer control over large scale. Figure 3.4B plots the areal coverage of ML ( $\theta_{1L}$ ) and multilayer ( $\theta_{\geq 2L}$ ; mostly bilayer) regions measured from our MoS<sub>2</sub> grown on SiO<sub>2</sub>/Si along with optical images (Figure 3.4A) at different growth times. It shows the initial nucleation on the SiO<sub>2</sub> surface ( $t = 0.5 t_0$ ), subsequent ML growth near ( $0.8 t_0$ ) and at the maximum ML coverage ( $t_0$ ), followed by nucleation mainly at grain boundaries ( $1.2 t_0$ ) and bilayer growth ( $2 t_0$ ). Significantly, we observe no nucleation of second layer while the first layer is forming ( $\theta_{\geq 2L} \sim 0$  when  $t < t_0$ ), producing an optimal growth time  $t_0$  near full ML coverage ( $\theta_{1L} \sim 1$ ). Additional PL and electron microscope

images taken after different growth times further suggest that the edge attachment is the main mechanism for the ML growth after nucleation and that the neighboring ML grains are uniformly connected by tilt grain boundaries with enhanced PL [55] at  $t = t_0$  (Figure 3.4C). The grown films show much brighter PL uniformly along GBs at  $t = t_0$  and much darker PL there when  $t > t_0$ . The brighter PL at  $t = t_0$  is consistent with the PL behaviors previously seen from the tilt GBs in CVD grown  $\text{MoS}_2$ <sup>19</sup> [55]. This suggests that upon the completion of the first layer growth ( $t = t_0$ ), neighboring grains are uniformly connected laterally by tilt GBs before further growth occurs for the second layer. Once the second layer starts growing on top of the first layer, the PL signal decreases especially along GBs, as the band structure of  $\text{MoS}_2$  shifts from direct bandgap (ML) to indirect bandgap (for multilayers).

We studied thermal reaction for DES and MHC using a residual gas analyzer (RGA), which connected to the outlet of the furnace and detects the mass signal of the gas residue. Figure 3.5A shows the relative intensity ratio for corresponding molecules extracted from mass spectra of RGA. First, we flowed vaporized MHC into the chamber at room temperature (blue circle), and we confirmed that vaporized MHC contains several carbonyl molybdenum,  $\text{Mo}(\text{CO})_x$ . Above 250 °C the signal for  $\text{Mo}(\text{CO})_x$  disappeared, indicating that  $\text{Mo}(\text{CO})_x$  was completely decomposed. In the case of DES, the intensity profiles at room temperature (blue circle) are almost the same as at growth temperature, 550 °C (red circle), with both showing various hydrocarbon sulfides ( $\text{C}_x\text{H}_y\text{S}$ ) under RGA resolution. This means that the concentration of DES in the furnace barely changed due to its decomposition. According to the RGA study, we summarize the status of precursors at growth temperature: (i) the concentration of  $\text{C}_x\text{H}_y\text{S}$  is uniform

inside the furnace at the laminar flow condition. (ii) MHC is decomposed to Mo and delivered by high flow Ar.

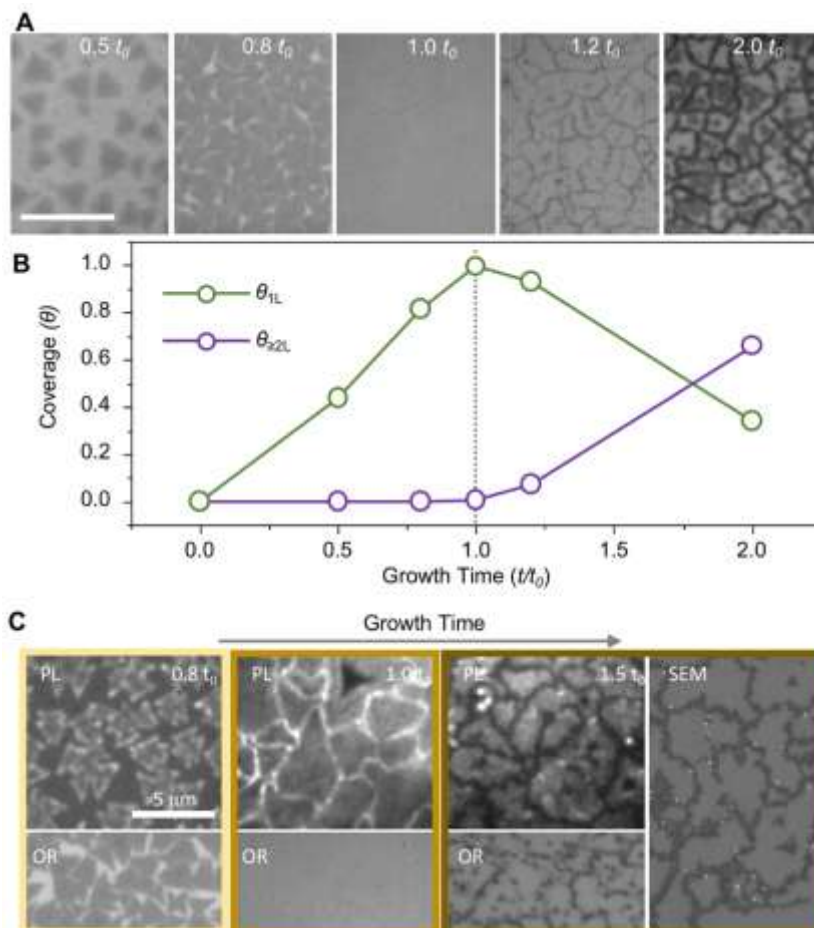


**Figure 3.4 Layer-by-layer growth of monolayer TMDs.**

(A) Optical images of MOCVD-grown MoS<sub>2</sub> at different growth times, where  $t_0$  is the optimal growth time for full ML coverage. Scale bar, 10 μm. (B) Coverage ratio for ML ( $\theta_{1L}$ ) and multi-layer region ( $\theta_{\geq 2L}$ ) as a function of growth time. (C) Optical reflection, PL, SEM images of MOCVD-grown MoS<sub>2</sub> at different growth times, where  $t_0$  is the optimal growth time for full ML coverage.

The standard thin film growth model [111] suggests this layer-by-layer growth mode is effective below a certain deposition rate of the growth species, above which it suggests a different mode that forms thicker islands. Indeed, the layer-by-layer growth of MoS<sub>2</sub> film was observed only when we apply a low partial pressure ( $P_{\text{Mo}} \sim 10^{-4}$  Torr

in Figure 3.4, A-B) of Mo vapor (produced by thermal decomposition of  $\text{Mo}(\text{CO})_6$ ) under the presence of excess  $(\text{C}_2\text{H}_5)_2\text{S}$ . In contrast, the growth at a higher  $P_{\text{Mo}}$  is no longer in the layer-by-layer growth mode, instead producing a mixture of ML, multilayer, and no growth regions simultaneously (Figure 3.5B). For the uniform ML growth over a large substrate, it is thus important to maintain a low  $P_{\text{Mo}}$  constantly over the entire growth region and over time, the key technical capability provided by our MOCVD setup.

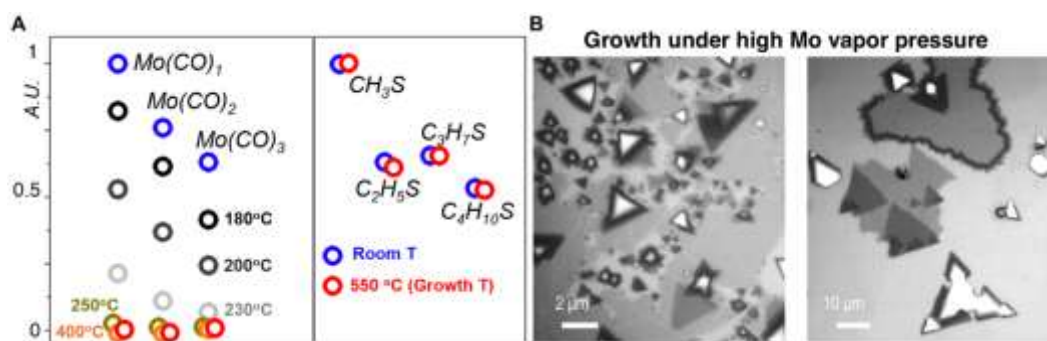


**Figure 3.5 Thermal decomposition of precursors.** (A) Normalized intensity of residual gas signal for  $\text{Mo}(\text{CO})_x$  and  $\text{C}_x\text{H}_y\text{S}$  depending on temperature. Each dot corresponds to a temperature, as denoted in the figure. (B) high Mo vapor concentration environment, where a mixture of monolayer, multilayer and no-growth regions exist.

### *Grain Size Control*

The grain structure of our  $\text{MoS}_2$  film, including the average grain size and the intergrain connection, depends sensitively on the concentrations of  $\text{H}_2$ ,  $(\text{C}_2\text{H}_5)_2\text{S}$  as well as residual water. Figure 3.6 shows the two main effects of  $\text{H}_2$ , whose presence is necessary for removing carbonaceous species generated during the MOCVD growth: (i) the average grain size increases from hundreds of nm to over 10  $\mu\text{m}$  with decreasing  $\text{H}_2$  flow, and (ii) the  $\text{MoS}_2$  grains grown under higher  $\text{H}_2$  flow have mostly perfect triangular shapes without merging with neighboring grains, a trend that disappears with

lower H<sub>2</sub> flow (left and middle images). These observations are consistent with the H<sub>2</sub> induced decomposition of (C<sub>2</sub>H<sub>5</sub>)<sub>2</sub>S (increasing nucleation due to hydrogenolysis) [112], and the etching of the MoS<sub>2</sub> (preventing intergrain connection) [113] as previously reported. As illustrated in Figure 3.6, the grain size also strongly depends on the concentration of (C<sub>2</sub>H<sub>5</sub>)<sub>2</sub>S and water (under the presence of salt desiccant, for example, NaCl, KCl, and NaBr). Grain size increases under lower concentration (C<sub>2</sub>H<sub>5</sub>)<sub>2</sub>S, and the grain size increased up to 100-fold, according to the presence/absence of salt.

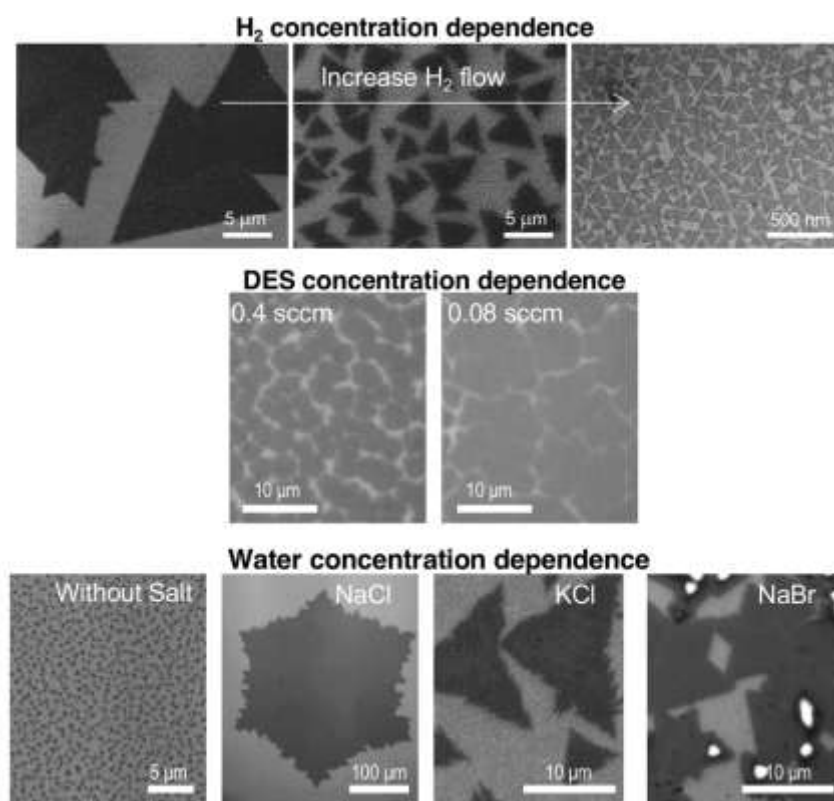


**Figure 3.6 Grain size control of monolayer TMD synthesis.**

Top row: Grain size variation of ML MoS<sub>2</sub> depending on the hydrogen flow rate from left to right; 5 sccm (SEM image shown), 20 sccm (SEM) and 200 sccm (TEM). Bottom row: Grain size dependence on DES flow rates. Bottom row: Grain size dependence on water concentration by using salt (desiccant).

In order to explain these phenomena, we need to discuss the precursor decomposition and nucleation kinetics. First, according to hydrolysis and

hydrogenolysis [112],  $H_2$  and  $H_2O$  promote the decomposition of DES precursor, which enhances the concentration of sulfur vapor. Also, the concentration of sulfur vapor linearly depends on the concentration of DES, since DES contains certain ratio of sulfur vapor. Second, the concentration of sulfur affects the nucleation kinetics and grain size. The assumptions we make are: (i) our growth is Mo diffusion limited growth, since the Mo concentration is kept low for layer-by-layer growth. In comparison, the concentration of DES is much higher than that of Mo vapor. (ii) when a Mo atom produced by thermal decomposition of MHC, arrives at the surface, it diffuses until reacting with sulfur produced by decomposition of DES. (iii) energetically, Mo and S atoms prefer to be adsorbed at a  $MoS_2$  edge. (iv) if the decomposition rate of DES is fast, Mo atoms lose their chance to find energetically favorable positions and nucleation occurs at a non-edge region. Based on these assumptions, we conclude that the nucleation density of  $MoS_2$  increases on the surface when the decomposition kinetics of DES becomes faster. Therefore, when  $H_2$ ,  $H_2O$ , and DES concentrations are high, nucleation density increases and grain size decreases.

As discussed earlier, the presence of salt (e.g. NaCl) is crucial for promoting lateral growth of monolayer TMDs due to its effect of reducing water concentration in the MOCVD process. Several recent studies suggest that NaCl can also promote the lateral growth of monolayer TMD by lowering the melting points of metal precursors and forming volatile intermediate metal oxychlorides. These observed effects of NaCl are especially beneficial for TMD growth based on precursors with high melting point such as  $MoO_3$  and  $WO_3$  [114–118].

### *Laterally Stitched Polycrystalline Monolayer TMD Films*

The darkfield transmission electron microscope (DF-TEM) and annular darkfield scanning TEM (ADF-STEM) images shown in Figure 3.7A-B confirm the structural continuity of our MoS<sub>2</sub> film grown under those conditions on the nanometer and atomic length scales. The DF-TEM image shows a continuous polycrystalline ML film with no visible gaps, while having less than 0.5% bilayer area. The ADF-STEM data (Figure 3.7B) further confirm that adjacent grains are likely to be connected by a high quality lateral connection with similar structures seen in previous reports [54, 55]. These high-quality grain boundaries result in mechanically strong ML TMD films that can be free-standing. Figure 3.7C shows a scanning electron microscope (SEM) image of an array of fully-suspended ML MoS<sub>2</sub> membranes (2 μm in diameter) fabricated by transferring our MOCVD-grown film onto a SiN grid with holes. Its high fabrication yield (> 99.5%) suggests mechanical strength and continuity of the film.

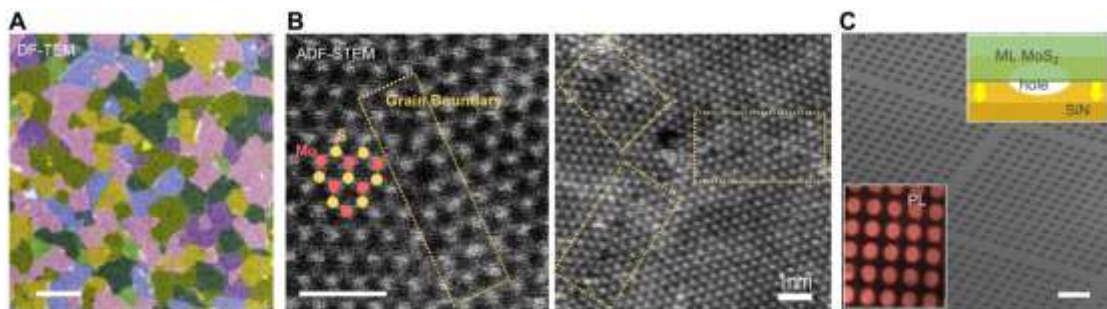


**Figure 3.7 Laterally stitched polycrystalline ML TMD films**

(A) False-color DF-TEM image showing a continuous ML MoS<sub>2</sub> film. Scale bar, 1 μm. (B) ADF-STEM images of laterally-stitched grain boundaries in a ML MoS<sub>2</sub> film, with red and yellow dots representing the Mo and S atoms, respectively. Scale bar, 1 nm. (C) SEM image and PL image (bottom inset, at 1.9 eV) of ML MoS<sub>2</sub> films suspended over SiN TEM grid with 2-μm-sized holes (schematic of suspended film in the top inset). Scale bar, 10 μm.

### *3.5 High Electrical Performance of Monolayer TMDs*

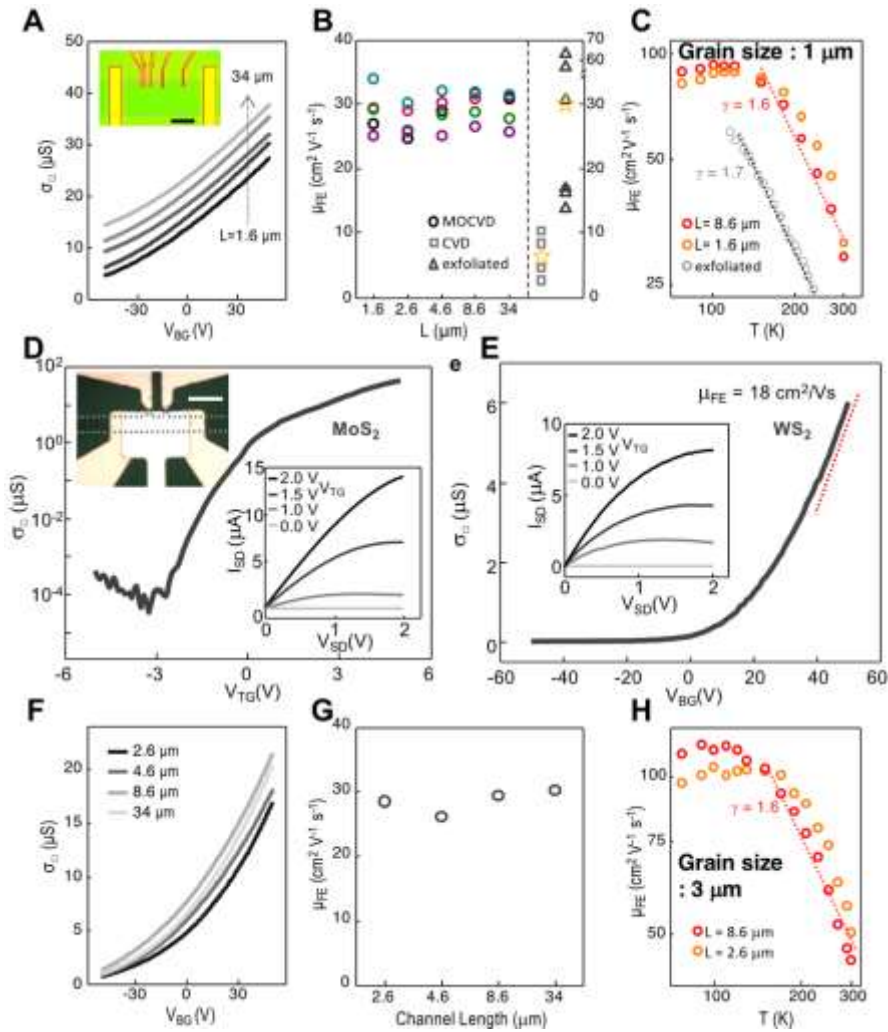


**Figure 3.8 Electrical characterization and batch fabrication of ML TMD FETs.**

(A) Gate-dependent sheet conductance ( $\sigma_{\square}$ ) of ML MoS<sub>2</sub> (grain size  $\sim 1 \mu\text{m}$  for A-C) FETs measured with different  $L$ , the channel length (curves shifted from the bottom for clarity). Inset: optical image of the device, scale bar  $10 \mu\text{m}$ . (B) Field effect mobility ( $\mu_{\text{FE}}$ ) measured from five MoS<sub>2</sub> FETs fabricated at random locations with different  $L$ . Data from previous results for CVD-grown [57] and exfoliated samples [104] are shown for comparison (yellow stars indicating their medians). (C) Temperature dependence of  $\mu_{\text{FE}}$  measured from the device in (A), and from a previous report on exfoliated samples [103], both showing the phonon limited intrinsic transport. (D) Top gate ( $V_{\text{TG}}$ ) dependent  $\sigma_{\square}$  for dual-gate ML MoS<sub>2</sub> FET (device shown in upper inset). Lower inset:  $V_{\text{TG}}$ -dependent  $I_{\text{SD}}-V_{\text{SD}}$  curves showing current saturation and Ohmic electrode contact. Scale bar,  $10 \mu\text{m}$ . (E) Transfer curves measured from MoS<sub>2</sub> (grain size  $\sim 3 \mu\text{m}$  for F-H) with different channel lengths. (F)  $\mu_{\text{FE}}$  of different channel lengths extracted from (E). (G)  $\mu_{\text{FE}}$  of different channel lengths extracted from (F). (H) Temperature dependence of  $\mu_{\text{FE}}$  measured from MoS<sub>2</sub> film of grain size  $3 \mu\text{m}$ , with different channel lengths, which show the same dependence as shown in (C).

The electrical properties of our ML MoS<sub>2</sub> films display two important characteristics: the spatial uniformity over a large scale and excellent transport properties similar to those seen in exfoliated samples. All our electrical measurements in this chapter (except for Figure 3.8, C and H) were performed at room temperature. Figure 3.8A first shows the sheet conductance ( $\sigma_{\square}$ ) vs backgate voltage ( $V_{BG}$ ) curves measured from a ML MoS<sub>2</sub> FET (optical image shown in the inset) with multiple electrodes for the four-probe measurements (except for channel length ( $L$ ) = 34  $\mu\text{m}$ ). It includes several curves for different  $L$  ranging between 1.6 and 34  $\mu\text{m}$  (shifted from the bottom one for clarity), all of which show nearly identical behaviors, including the  $n$ -type conductance, carrier concentration ( $\sim 4 \times 10^{12} \text{ cm}^{-2}$  at  $V_{BG} = 0 \text{ V}$ ), and high field effect mobility ( $\mu_{FE}$ ). Figure 3.8B further plots  $\mu_{FE}$  measured from five such devices, fabricated at random locations and separated by up to 3.3 mm on a single chip. All the devices show similar  $\mu_{FE}$  near 30  $\text{cm}^2/\text{Vs}$  independent of  $L$  and device location with similarly uniform  $\sigma_{\square}$ - $V_{BG}$  curves, suggesting the spatial homogeneity of the electrical properties of the MoS<sub>2</sub> film at length scales ranging from micrometers to millimeters.

The distribution of  $\mu_{FE}$  of our devices is compared with the results of multiple devices from two previous reports, each measured from individual grains of exfoliated [104] or CVD grown [57] MoS<sub>2</sub> samples. Surprisingly,  $\mu_{FE}$  measured from our MOCVD film is similar to the median  $\mu_{FE}$  (denoted by a star) of exfoliated samples (and several times higher than the CVD results), while displaying a much narrower distribution. In addition, the temperature dependence of  $\mu_{FE}$  (Figure 3.8C) measured from the same device in Figure 3.8A shows higher  $\mu_{FE}$  at lower temperatures (92  $\text{cm}^2/\text{Vs}$  at 100K) and

the intrinsic, phonon-limited electron transport, similar to the behaviors previously observed in exfoliated samples (data from ref. 108 shown in Figure 3.8C) but different from those observed from a CVD sample with stronger effects from defects [119]. Specifically, our data show the characteristic of  $\mu_{FE} \sim T^{-\gamma}$  dependence between 150 and 300K with  $\gamma = 1.6$ , close to the value predicted by theory (1.69) [102] and consistent with results from previous experiments (average value ranging between 0.6 and 1.7) [103–106] for a similar temperature range. Finally, Figure 3.8D shows a high-performance MoS<sub>2</sub> FET fabricated with an individual top-gate electrode ( $V_{TG}$ ). It has a high on/off conductance ratio ( $\sim 10^6$ ), current saturation at relatively low bias  $V_{SD}$  (lower inset, Figure 3.8D), high field effect mobility ( $\sim 29 \text{ cm}^2/\text{Vs}$ ) and large transconductance ( $\sim 2 \text{ }\mu\text{S}/\mu\text{m}$ ), all of which are comparable to the best reported results [103–105]. We note that our devices studied in Figure 3.8 were fabricated at random locations using a polycrystalline ML MoS<sub>2</sub> film, unlike the devices with single-grain samples used for comparison.

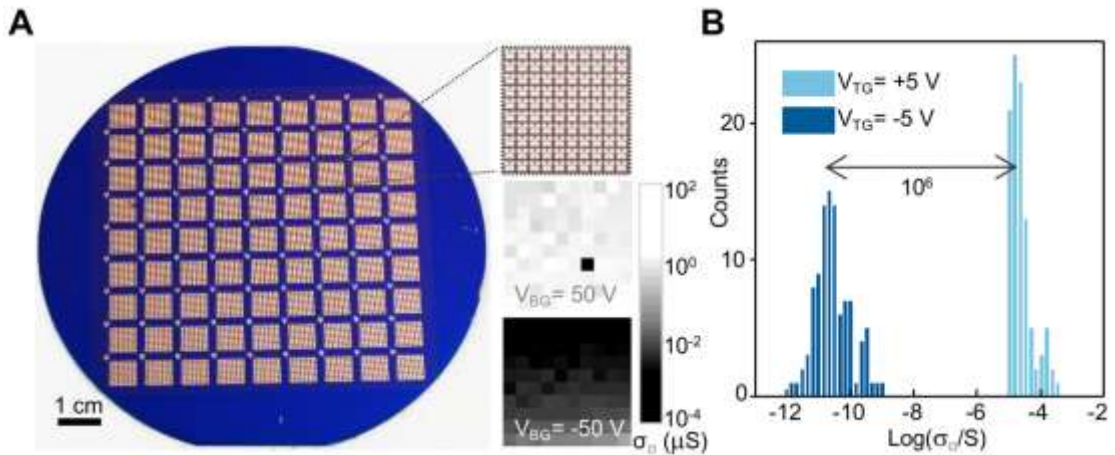
In addition, the electrical properties measured from a separate ML MoS<sub>2</sub> film with a larger average grain size of 3  $\mu\text{m}$  (instead of 1  $\mu\text{m}$  in Figure 3.8, A-C) show almost identical characteristics, including the channel length independence of  $\mu_{FE}$  and the phonon-limited transport at  $T > 150\text{K}$  (see Figure 3.8, F-H; with the low temperature mobility as high as  $114 \text{ cm}^2/\text{Vs}$  at 90K). Altogether, our data shown in Figure 3.8 confirm the spatial uniformity and high electrical performance of our MoS<sub>2</sub> FETs independent of the average grain size, which suggests that the inter-grain boundaries in our film do not significantly degrade their electrical transport properties. This is likely due to the formation of well-stitched inter-grain boundaries with a low level of defects,

an explanation also supported by the ADF-STEM (Figure 3.7B) and XPS data (Figure 3.1G) discussed earlier. Therefore, our data lead to an important conclusion that our optimized MOCVD growth provides an electrically homogeneous ML MoS<sub>2</sub> film. Moreover, we successfully fabricated and measured 60 FETs using a ML WS<sub>2</sub> film. Even though the growth of ML WS<sub>2</sub> is not carefully optimized, these devices show excellent electrical properties with their  $\mu_{FE}$  as high as 18 cm<sup>2</sup>/Vs at room temperature (Figure 3.8E) with the median  $\mu_{FE}$  close to 5 cm<sup>2</sup>/Vs. In addition, the WS<sub>2</sub> device shows a high on/off ratio of 10<sup>6</sup> and the current saturation behavior (inset, Figure 3.8E) as in our MoS<sub>2</sub> devices.

### ***3.6 Wafer-Scale Batch Fabrication of Monolayer TMD FETs***

The structural and electrical uniformity of our MoS<sub>2</sub> film enables the wafer-scale batch fabrication of high performance FETs as demonstrated in Figure 3.9, A-B. Figure 3.9A shows a photo of 8,100 MoS<sub>2</sub> FETs with a global back gate, which were fabricated on a 4-inch SiO<sub>2</sub>/Si wafer using a standard photolithography process. The middle and bottom insets to Figure 3.9A shows the color-scale map of  $\sigma_{\square}$  measured from 100 MoS<sub>2</sub> FETs in one square region at  $V_{BG} = +50$  V and -50 V, respectively; the top inset to Figure 3.9A shows an enlarged optical image of the devices. We observed an almost perfect device yield of 99%; only two out of 200 FETs we characterized (including data from an adjacent region) do not conduct. Our data also confirm the spatially uniform *n*-type transistor operation (larger  $\sigma_{\square}$  for positive  $V_{BG}$ ) with similar  $V_{BG}$  dependence for all our devices and high on-state device conductance.

**Figure 3.9 Batch fabrication of ML TMD FETs.**



(A) Batch-fabricated 8,100 MoS<sub>2</sub> FET devices on a 4-inch SiO<sub>2</sub>/Si wafer. Top inset: enlarged image of one square containing 100 devices. Middle and bottom insets: corresponding color maps of  $\sigma_{\square}$  at gate bias  $V_{BG} = 50\text{ V}$  and  $-50\text{ V}$  respectively, with the black block in the middle inset representing the only non-conducting device. (B) Histogram of on- and off- state  $\sigma_{\square}$  of 100 dual-gate FETs showing a median on-off ratio of  $10^6$  and a high on-state conductivity.

Similarly, we fabricated 100 individually addressable dual gate MoS<sub>2</sub> FETs (similar to the device in Figure 3.8D) on another wafer piece. The histogram of the on-state  $\sigma_{\square}$  ( $V_{TG} = 5\text{ V}$ ; median carrier concentration  $\sim 7 \times 10^{12}\text{ cm}^{-2}$ ) and off-state  $\sigma_{\square}$  ( $V_{TG} = -5\text{ V}$ ) collected from all such FETs (Figure 3.9B) shows strong peaks above  $10^{-5}\text{ S}$  and near  $10^{-11}\text{ S}$ , respectively, confirming a uniform conductance switching behavior with high on-state  $\sigma_{\square}$  ( $> 10\ \mu\text{S}$ ) and on-off ratio ( $\sim 10^6$ ).

### 3.7 Summary

In this chapter we presented our work on the MOCVD synthesis of high-mobility, 4-inch wafer-scale films of ML MoS<sub>2</sub> and WS<sub>2</sub> directly grown on insulating SiO<sub>2</sub> substrates, with excellent spatial homogeneity over the entire films. We note that our high-mobility ML TMD films can be immediately utilized for the batch fabrication of

TMD-based integrated circuitry consisting of FETs, photodetectors and light emitting diodes, on a technologically-relevant multi-inch wafer scale.

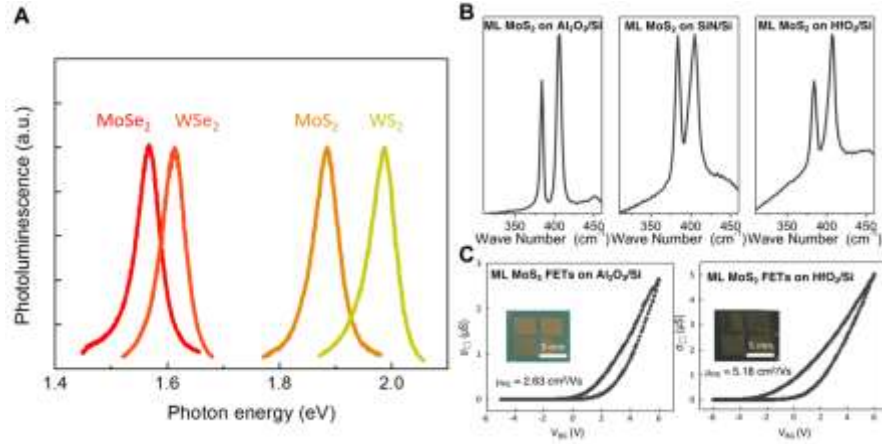


**Figure 3.10 Synthesis of various TMDs on various substrates.**

(A) PL spectra for MOCVD grown MoSe<sub>2</sub>, WSe<sub>2</sub>, MoS<sub>2</sub> and WS<sub>2</sub>, respectively. These TMDs were synthesized using MOCVD technique on wafer scale and show expected intrinsic PL spectra. (B) Raman spectra for MoS<sub>2</sub> grown on Al<sub>2</sub>O<sub>3</sub>, SiN and HfO<sub>2</sub> covered Si, respectively. (C)  $\sigma_{\square}$ - $V_{BG}$  curves for ML MoS<sub>2</sub> FET on Al<sub>2</sub>O<sub>3</sub>/Si and HfO<sub>2</sub>/Si, respectively.

In addition, as our MOCVD growth is controlled by the kinetics of precursor supply rather than specific precursor/substrate chemistry (an example of the latter would be the different graphene growth modes on Cu vs Ni), its use is not limited to the TMD/substrate combinations reported here. Our MOCVD technique could be generalized for producing various TMD materials, both semiconductor (e.g. MoSe<sub>2</sub>, WTe<sub>2</sub>) and metal (e.g. NbSe<sub>2</sub>, TaS<sub>2</sub>), with precise layer control over a large scale. Indeed, different TMDs can be synthesized using our MOCVD technique (PL spectra of representing MoSe<sub>2</sub> and WSe<sub>2</sub> shown in Figure 3.10A). As an initial demonstration, the ML TMD growth is possible on a variety of other technologically important substrates (Al<sub>2</sub>O<sub>3</sub>, SiN, HfO<sub>2</sub>) with the same growth conditions developed for SiO<sub>2</sub> (see Figure 3.10, B and C, for MoS<sub>2</sub> growth and device fabrication on these substrates using these

non-optimized conditions). Therefore, our versatile MOCVD growth provides an exciting new avenue for the growth, patterning and integration of multiple, high-quality ML TMD films with different compositions and electrical properties on a single substrate, enabling the future development of atomically thin integrated circuitry.

CHAPTER 4  
COHERENT, MONOLAYER TRANSITION METAL DICHALCOGENIDE  
SUPERLATTICES WITH ENGINEERED STRAIN

### ***4.1 Introduction***

Heterostructures that join together materials with different electronic properties are the fundamental element for circuits and optoelectronic devices. High quality heterostructures are often produced using epitaxy technique, where crystalline films are deposited on top of a single crystalline substrates, while maintaining the atomic registry. While the crystalline epilayer can be readily grown, its lattice spacing may differ from that of the substrate, due to the intrinsic lattice mismatch between the epi-material and the substrate. Such lattice mismatch, especially when large, often results in incoherent epitaxy, where arrays of dislocations form at the heterointerface and the lattice constants of both the epilayer and substrate remain their intrinsic values (schematically illustrated in Figure 4.1A, top). The dislocations at the heterointerfaces generally degrade the performance of heterostructure devices, for example, by increasing the scattering rates of carriers in the electronic device and promoting non-radiative recombination in light emitting devices (Figure 4.1B). In contrast, the lattice spacing in the direction parallel to the heterointerface of the epilayer may change to match that of the substrate, leading to coherent epitaxy with no dislocation at the interface (Figure 4.1A, bottom).

In addition to the coherent heterointerface, another important aspect of heterostructure is to precisely control their spatial composition (i.e. producing superlattices). Superlattices with coherent heterointerfaces enable advanced scientific

and technological applications, including multiferroic oxides with engineered strain and symmetry (Figure 4.1C) [120, 121], high-performance quantum cascade lasers [122], and high-efficiency light emitting diodes [123].

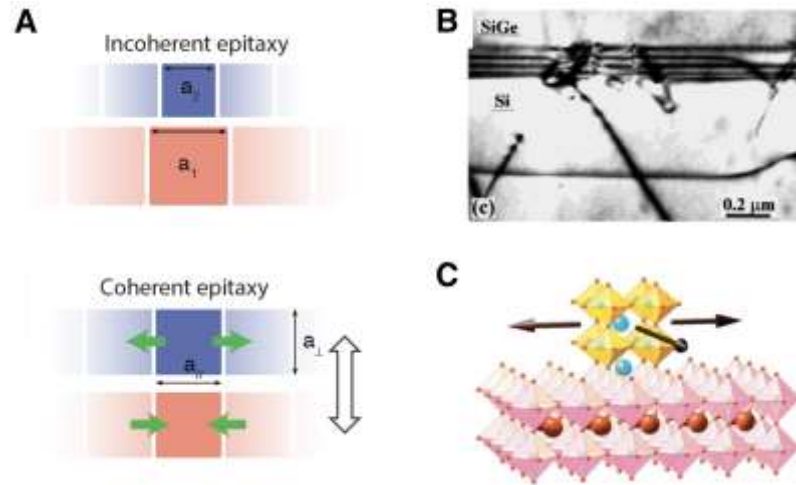


**Figure 4.1 Incoherent and coherent epitaxy.**

(A) Schematic of incoherent and coherent epitaxy, with the epitaxy direction represented by the outlined arrow. (B) Micrographs of misfit dislocation networks at the interface between Si and SiGe. Reproduced from Ref. [124]. (C) Schematic of strain engineering of epi-layer via coherent epitaxy. Reproduced from Ref. [121].

The dimensionality of heterostructures determines how they interact with external matter and their environment. For heterostructures and superlattices based on 3D materials, the heterointerfaces are automatically embedded in the structure once formed (Figure 4.2, left). In contrast, the heterointerfaces in 2D superlattices are always exposed, as the result of the unique all-surface feature of 2D materials (Figure 4.2, right). Such a feature allows one to modulate the properties of 2D materials by integrating them with other materials. In this regard, 2D coherent heterostructures and superlattices can serve as ultrathin building blocks for advanced stacking and hetero-integration with other materials [101, 125, 126] and provide opportunities not available to their 3D analogs.

Realizing this goal would require the integration of various 2D materials whose properties can be tuned by the strain required for coherent lattice matching, as well as a method for precisely controlling the superlattice dimensions while maintaining lattice coherence over the entire structure. Monolayer transition metal dichalcogenides (TMDs), many of which share similar crystal structures, provide an ideal material platform with diverse electrical, optical [23, 127], piezoelectric [6, 7], and valley properties [21]. However, recent studies on TMD heterostructure synthesis have shown only limited capabilities toward realizing coherent 2D superlattices [68–71, 128–132].

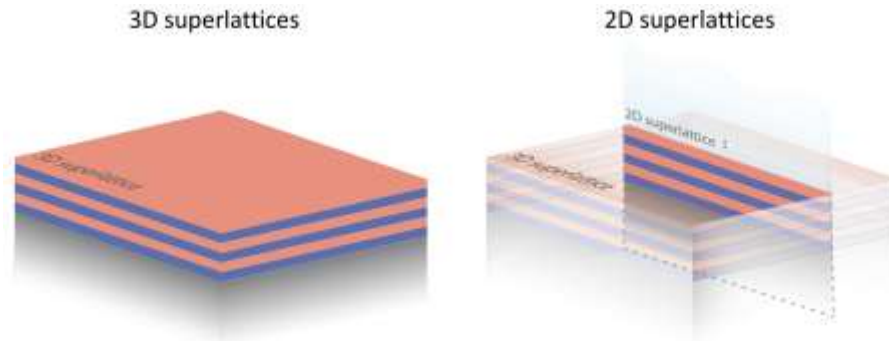


**Figure 4.2 3D and 2D superlattices.**

Schematics of 3D (left) and 2D (right) superlattices, where 2D superlattices can be regarded as a cross section of their 3D counterpart due to the reduced dimension.

In this chapter, which is largely adapted from Ref. 133, we report coherent monolayer TMD superlattices with precisely controlled supercell dimensions and lattice coherence maintained over the entire structure. Grown by an omnidirectional epitaxy, these superlattices display fully-matched lattice constants across heterointerfaces while maintaining a surprisingly isotropic lattice structure and triangular symmetry, despite large lattice mismatches. This strong epitaxial strain is precisely engineered via the nanoscale supercell dimensions, thereby enabling broad tuning of the optical properties and producing photoluminescence peak shifts as large as 250 meV. We present

theoretical models to explain this coherent growth and the energetic interplay governing the ripple formation in these strained monolayers. Such coherent superlattices provide building blocks with targeted functionalities at the atomically-thin limit.

#### 4.2 Synthesis of Monolayer TMD Superlattices: Modulated MOCVD

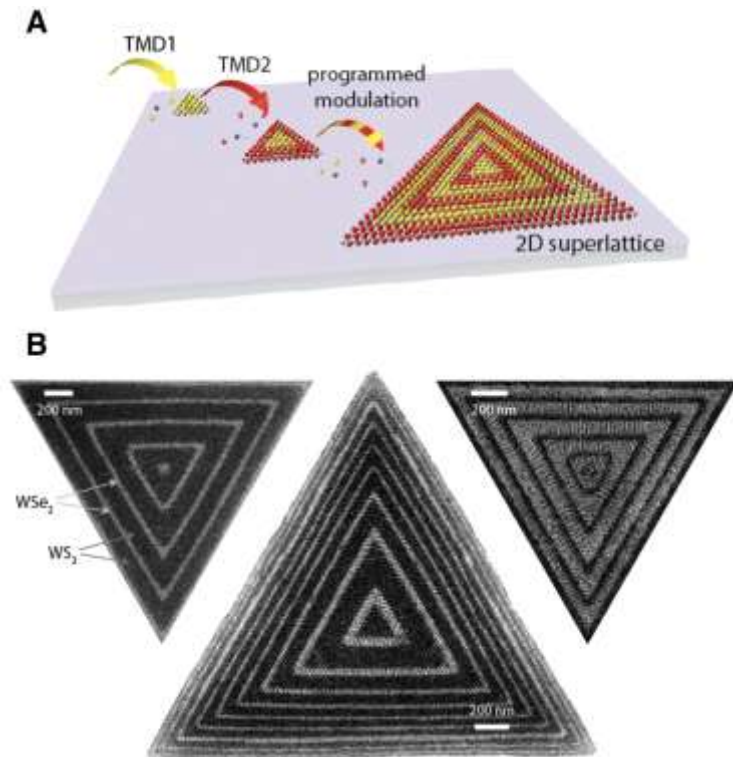


**Figure 4.3 2D monolayer TMD superlattices.**

(A) Schematic of 2D superlattices based on monolayer TMDs. (B) SEM images of three monolayer WS<sub>2</sub>/WSe<sub>2</sub> superlattices. Scale bars, 200 nm.

We used WS<sub>2</sub> and WSe<sub>2</sub> as the two main TMDs for our heterostructures and superlattices (Figure 4.3A), where the repeat direction of the superlattice is in the growth plane of a monolayer, rather than the out-of-plane direction of conventional thin-film superlattices. These TMDs have a substantial lattice mismatch ( $\Delta$ ) of  $\sim 4\%$  with WSe<sub>2</sub> having the larger lattice constant. In scanning electron microscope (SEM) images

of three representative WS<sub>2</sub>/WSe<sub>2</sub> heterostructures with controlled supercell dimensions (Figure 4.3B), dark (bright) regions correspond to WS<sub>2</sub> (WSe<sub>2</sub>) monolayers. Every triangular unit of WS<sub>2</sub> and WSe<sub>2</sub> shows a highly-symmetric, equilateral triangular shape of uniform width, each defined by straight, parallel heterointerfaces, that could be directly controlled with nanoscale precision. These widths could be as narrow as 20 nm (Figure 4.3B, center) and periodically modulated to form superlattices with different dimensions, represented by the two widths { $d_{\text{WS}_2}$  and  $d_{\text{WSe}_2}$ }. Two examples of superlattices are shown, one primarily composed of WS<sub>2</sub> ( $d_{\text{WS}_2} \gg d_{\text{WSe}_2}$ ) (Figure 4.3B, left) and the other by WSe<sub>2</sub> ( $d_{\text{WS}_2} \ll d_{\text{WSe}_2}$ ) (Figure 4.3B, right). Heterostructures consisting of different metal and chalcogen elements could also be synthesized with a similar level of control (see Figure 4.4C for an example of a WSe<sub>2</sub>/MoS<sub>2</sub>/WS<sub>2</sub> heterostructure).

### ***Precisely Controlled Precursor Supplies***

These crystalline TMD superlattices were synthesized by a modulated metal-organic chemical vapor deposition (MOCVD) [93] process with two distinctive features compared with previous approaches (schematic shown in Figure 4.4A) [68–71, 128–132]. During the synthesis process, the concentration of each precursor was individually and precisely controlled, which allowed the direct tuning of the supercell dimensions. Tungsten hexacarbonyl (THC), molybdenum hexacarbonyl (MHC), diethyl sulfide (DES), and dimethyl selenide (DMSe) were selected as chemical precursors for W, Mo, S and Se, respectively. THC and MHC were kept in bubblers at a constant pressure of 800 Torr and introduced into the furnace with Ar as the carrier gas at room temperature.

The growth of the superlattices was kept at a constant temperature of 600 °C and a total pressure of 2 Torr throughout. Flow rates of all precursors were kept constant during the growth except for the chalcogens: 20 sccm of THC or MHC with Ar as the carrier gas, 1 sccm H<sub>2</sub> and 350 sccm Ar, 0.3 sccm DES, and 0.4 sccm DMSe. For WS<sub>2</sub>/WSe<sub>2</sub> superlattice growth, the flow of the chalcogen precursors was alternated with breaks (typically 2 min) in between for purging purposes (see schematic in Figure 4.4B). The width of each component was determined by controlling the timing of the switch, according to a simple linear dependence between the width and the growth time (Figure 4.4D).

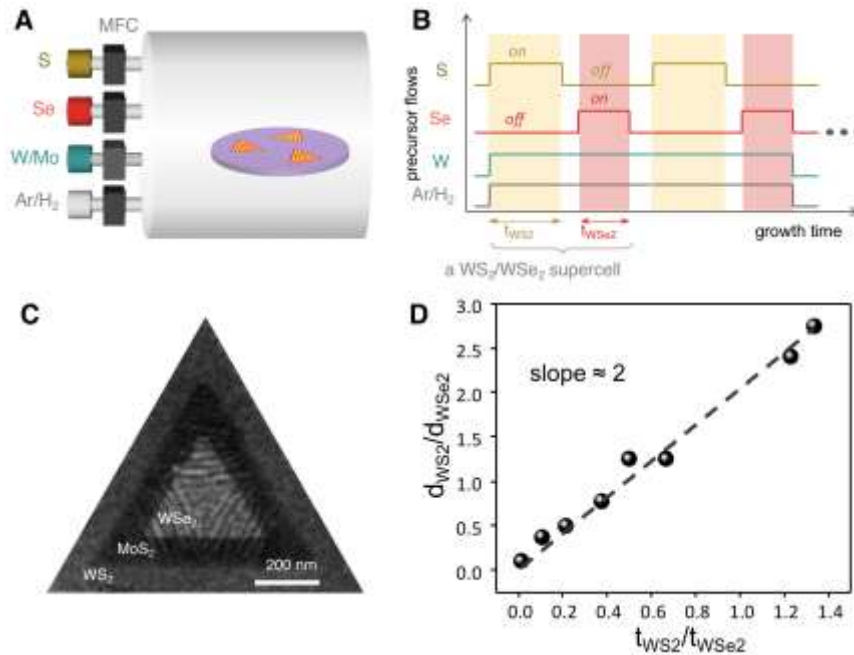


**Figure 4.4 Modulated MOCVD process.**

(A) Schematic of modulated-MOCVD reactor with individual MFCs that precisely control the flow of all precursors. (B) Time sequence of the modulated superlattice growth where the growth time for a supercell {WS<sub>2</sub> and WSe<sub>2</sub>} is { $t_{WS_2}$  and  $t_{WSe_2}$ }. (C) SEM image of a coherent WSe<sub>2</sub>/MoS<sub>2</sub>/WS<sub>2</sub> heterostructure. (D) Plot of relative widths ( $\rho = d_{WS_2}/d_{WSe_2}$ ) of superlattices versus relative growth time ( $t_{WS_2}/t_{WSe_2}$ ) showing a linear dependence.

### ***Constant Growth Environment***

The growth environment was maintained constant throughout the synthesis regardless of the specific TMD composition, which was crucial for producing coherent heterointerfaces. For example, both WS<sub>2</sub> and WSe<sub>2</sub> were grown under constant temperature, pressure, and overall flow rate, with the only difference being the chalcogen precursors. In our experiment, different components of our superlattices were grown with a slow growth rate (ranging between 20 and 60 nm/min) near thermodynamic equilibrium, and exhibited straight heterointerfaces with the most stable W-zigzag edges [134, 135]. In contrast, the synthesis with a temperature decrease (3 min, down to 300 °C) between different TMD growths result in heterostructures without lattice coherence.

### ***4.3 Lattice Coherence of WS<sub>2</sub>/WSe<sub>2</sub> Superlattices.***

In this section, we show that our WS<sub>2</sub>/WSe<sub>2</sub> superlattices maintained lattice coherence over the entire crystal despite the large 4% lattice mismatch between WS<sub>2</sub> and WSe<sub>2</sub>. We used various TEM techniques to confirm the lattice coherence over the entire superlattices with nanometer resolution.

First, the superlattices were free of misfit dislocations. Figure 4.5A shows an annular dark-field scanning transmission electron microscope (ADF-STEM) image near a heterointerface (dashed line) between WS<sub>2</sub> (lower) and WSe<sub>2</sub> (upper). The ADF-STEM data taken from a larger area (Figure 4.5B) shows continuous lines of atoms with no misfit dislocations near the heterointerface across ~160 unit cells (shown after the inverse fast Fourier transform (FFT)). One dislocation is expected every 25 unit cells

on average for incoherent heterointerfaces with  $\Delta \approx 4\%$ , so these images are consistent with our superlattice forming coherent heterointerfaces.

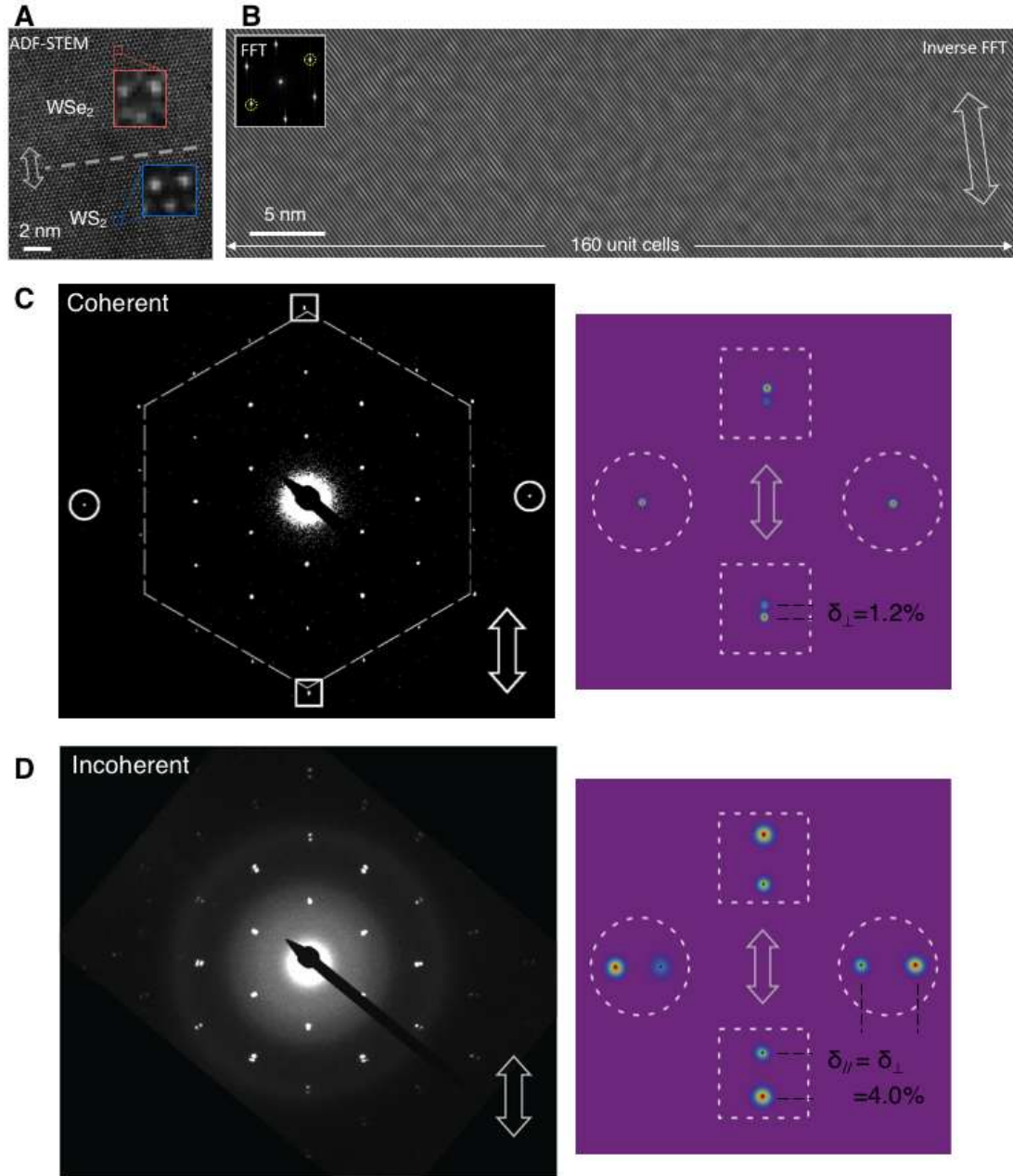


**Figure 4.5 Lattice coherence of WS<sub>2</sub>/WSe<sub>2</sub> superlattices.**

(A) An ADF-STEM image at the heterointerface area between WS<sub>2</sub> and WSe<sub>2</sub> (epitaxy direction represented by the arrow, same for all). Scale bar, 2 nm. (B) Inverse FFT of an ADF-STEM image from a larger area near the heterointerface, based on the circled spots in its FFT (inset). Scale bar, 5 nm. (C) SAED pattern of superlattice {50 nm and 40 nm}, taken from an area of diameter of 280 nm. (Inset) Enlarged diffraction spots as

indicated in (C). (D) SAED pattern of an incoherent WS<sub>2</sub>/WSe<sub>2</sub> heterostructure. (Inset) The same enlarged diffraction spots as in (C, inset).

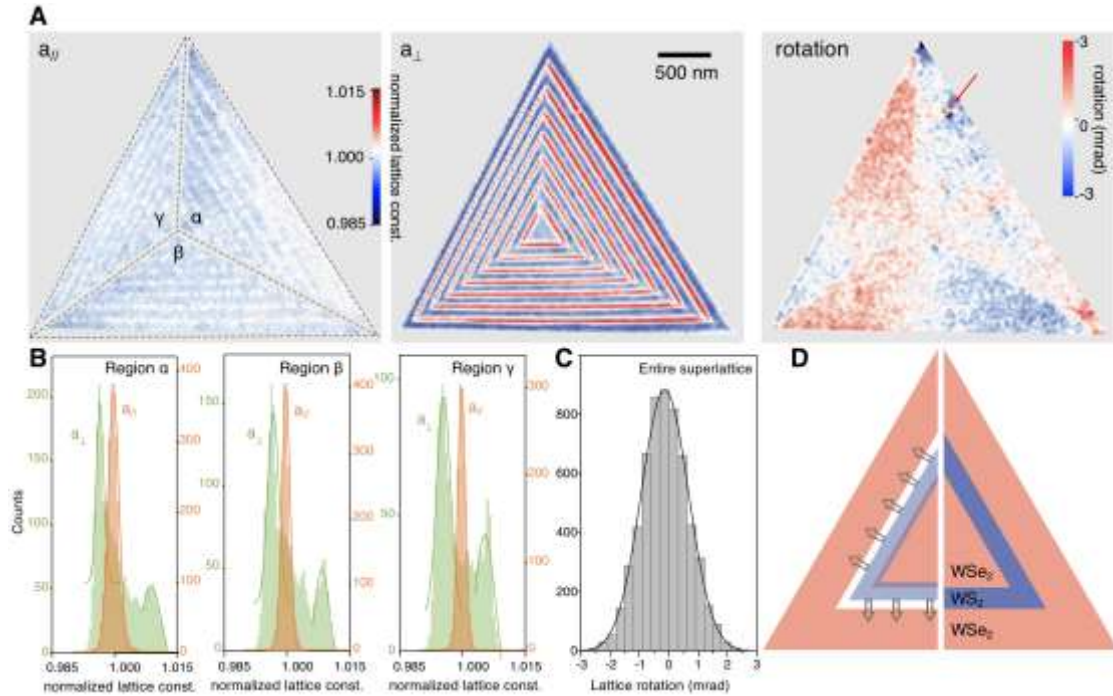


**Figure 4.6 Lattice coherence over entire WS<sub>2</sub>/WSe<sub>2</sub> superlattices.**

(A) Spatial maps of normalized lattice constants  $a_{||}$ ,  $a_{\perp}$ , and lattice rotation map of superlattice {75 nm and 60 nm}. Scale bar, 500 nm. (B) Histograms of  $a_{||}$  and  $a_{\perp}$  for region  $\alpha$  (two  $a_{\perp}$  peaks centered at 0.996 and 1.008),  $\beta$  (two  $a_{\perp}$  peaks centered at 0.996 and 1.008), and  $\gamma$  (two  $a_{\perp}$  peaks centered at 0.996 and 1.005). (C) Histogram of lattice rotation of the entire superlattice showing a standard deviation of 0.8 mrad. (D) Schematic of the isotropic expansion of the WS<sub>2</sub> lattice in an omnidirectional coherent WS<sub>2</sub>/WSe<sub>2</sub> heterostructure.

Second, our superlattices displayed lattice constants that were uniform over the entire structure. Figure 4.5C shows selective-area electron diffraction (SAED) data measured from a representative superlattice {50 nm and 40 nm} within a region with a single epitaxy direction (denoted by the arrow). These data exhibited a single-crystal-like pattern with sharp and isotropic diffraction spots. We used their positions to measure the lattice constants along the directions parallel ( $a_{||}$ ) or perpendicular ( $a_{\perp}$ ) to the heterointerfaces (schematic, Figure 4.1A), as well as the lattice mismatch along each

direction (e.g.,  $\delta_{//} = 2|a_{//,1} - a_{//,2}|/(a_{//,1} + a_{//,2})$ ). Diffraction data corresponding to  $a_{//}$  (circles in Figure 4.5C, enlarged in the inset) showed a single diffraction spot with no separation, confirming perfect lattice matching ( $\delta_{//} = 0$ ). Diffraction data corresponding to  $a_{\perp}$  (squares in Figure 4.5C, enlarged in the inset) also showed similar lattice constants; while two spots were observed, each originating from the WS<sub>2</sub> and WSe<sub>2</sub> regions (see below), the mismatch  $\delta_{\perp} = 1.2\%$  was much smaller than  $\Delta$ . In contrast, the same diffraction spots measured from an incoherent WS<sub>2</sub>/WSe<sub>2</sub> heterostructure displayed a 4% concentric separation with  $\delta_{//} = \delta_{\perp} = \Delta$  (Figure 4.5D and inset).

Lattice coherence was directly confirmed with nanoscale resolution over the entire WS<sub>2</sub>/WSe<sub>2</sub> superlattice. We used our newly-developed electron microscope pixel array detector (EMPAD), which measures local diffraction maps pixel-by-pixel, providing structural information for imaging with nanoscale resolution (as introduced in Section 2.4) [94]. Figure 4.6A shows three maps generated based on EMPAD data taken from another superlattice {75 nm and 60 nm}, each plotting  $a_{//}$ ,  $a_{\perp}$ , and lattice rotation. We note that the superlattice consists of three regions ( $\alpha$ ,  $\beta$ , and  $\gamma$ ; as outlined in the  $a_{//}$  map) with heterointerface orientations rotated by 120° from each other. The orientations of  $a_{//}$  and  $a_{\perp}$  are different for  $\alpha$ ,  $\beta$ , and  $\gamma$ , and defined relative to the heterointerfaces in each region. The  $a_{//}$  map (Figure 4.6A left) showed little contrast between WS<sub>2</sub> and WSe<sub>2</sub>, generating a single histogram peak as shown in Figure 4.6B for region  $\alpha$ ,  $\beta$ , and  $\gamma$ , respectively. The  $a_{\perp}$  map showed a small contrast between the WS<sub>2</sub> and WSe<sub>2</sub> regions, generating two peaks (Figure 4.6B) centered 0.4% below (corresponding to WS<sub>2</sub>) and 0.8% above (corresponding to WSe<sub>2</sub>) the  $a_{//}$  peak, resulting in  $\delta_{\perp} = 1.2\%$  as seen in

Figure 4.5C. Third, the lattice rotation map resolved only one dislocation clearly (arrow) within the entire superlattice (lateral size  $\sim 3.2 \mu\text{m}$ ), suggesting the existence of a dislocation-free, coherent lattice everywhere, including the boundary regions between the  $\alpha$ ,  $\beta$ , and  $\gamma$  regions. In contrast, incoherent heterostructures showed arrays of dislocations at heterointerfaces (Figure 4.7).

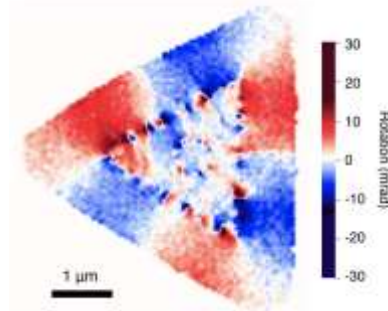


**Figure 4.7 Lattice rotation map of an incoherent  $\text{WS}_2/\text{WSe}_2$  heterostructure.** An incoherent  $\text{WS}_2/\text{WSe}_2$  heterostructure showing arrays of dislocations at the heterointerfaces. Scale bar,  $1 \mu\text{m}$ .

#### 4.4 Omnidirectional Epitaxy

Figure 4.6 shows that  $\delta_{//} = 0$  everywhere, confirming coherent heterointerfaces in our superlattice. In addition, we note that the lattice isotropy and rotational symmetry were maintained over the entire superlattice. Our TEM and EMPAD data confirm that (i) nearly identical and isotropic unit cell dimensions for both the  $\text{WS}_2$  and  $\text{WSe}_2$  regions and that (ii) the lattice orientation in our EMPAD map (Figure 4.6A, right) was highly uniform (standard deviation  $< 1 \text{ mrad}$ ), consistent with the observed sharp and isotropic TEM diffraction spots (Figure 4.5C), (iii) that the superlattice is triangular with straight edges and heterointerfaces. This result is in sharp contrast to the lattice anisotropy expected from conventional unidirectional epitaxy, where  $a_{//}$  is matched for the epilayers and  $a_{\perp}$  is free from any constraints, causing the superlattice to have a different symmetry

than that of the original crystal. Instead, our superlattice grew with coherent omnidirectional epitaxy where regions of different epitaxy directions ( $\alpha$ ,  $\beta$ , and  $\gamma$ ) coherently connect with each other while maintaining the same symmetry of the original crystal.

The perfect symmetry in our coherent superlattices imposes an additional constraint that requires identical values of  $a_{\perp}$  for both  $\text{WS}_2$  and  $\text{WSe}_2$ . This feature is further illustrated in Figure 4.6D: When a triangular  $\text{WSe}_2$  unit was replaced by  $\text{WS}_2$ , the latter needed to expand by the same amount in all directions (i.e., larger  $a_{\parallel}$  and  $a_{\perp}$ ) in order to coherently bridge the inner and outer triangular  $\text{WSe}_2$  units. This ideal picture changes in real superlattices with finite bulk and shear moduli values, where the final structure will minimize the total elastic strain energy. In this case, the lattice would deviate from having identical  $a_{\perp}$  values for  $\text{WS}_2$  and  $\text{WSe}_2$ , resulting in  $0 \lesssim \delta_{\perp} < \Delta$ , as seen from our data.

### ***Lattice Isotropy***

Below, we explain the symmetry and lattice isotropy in the superlattice grown by omnidirectional coherent epitaxy, using a symmetry analysis. We use a square lattice to illustrate the symmetry constraint for simplicity. Conventional unidirectional coherent epitaxy only requires matched  $a_{\parallel}$  while  $a_{\perp}$  is free of any constraints, thus  $a_{\perp}$  of small (large) lattice becomes even smaller (larger), corresponding to  $\delta_{\perp} > \Delta$  for positive Poisson's ratio (Figure 4.8A). Therefore, the resulting heterostructure shows a different symmetry (rectangular) than that of the original crystal (square). However, in omnidirectional coherent epitaxy, the epilayers grown in all directions connect to each

other without dislocation. As a result, the final heterostructure maintains the same symmetry with that of the original crystal, showing  $\delta_{\perp} = 0$  (Figure 4.8B). Similar results for our  $\text{WS}_2/\text{WSe}_2$  superlattices is illustrated in Figure 4.6D. The isotropic lattice constants result in an isotropic change of lattice constants, regardless of the intrinsic Poisson's ratios of each component, and is universal for any coherent omnidirectional epitaxy system.

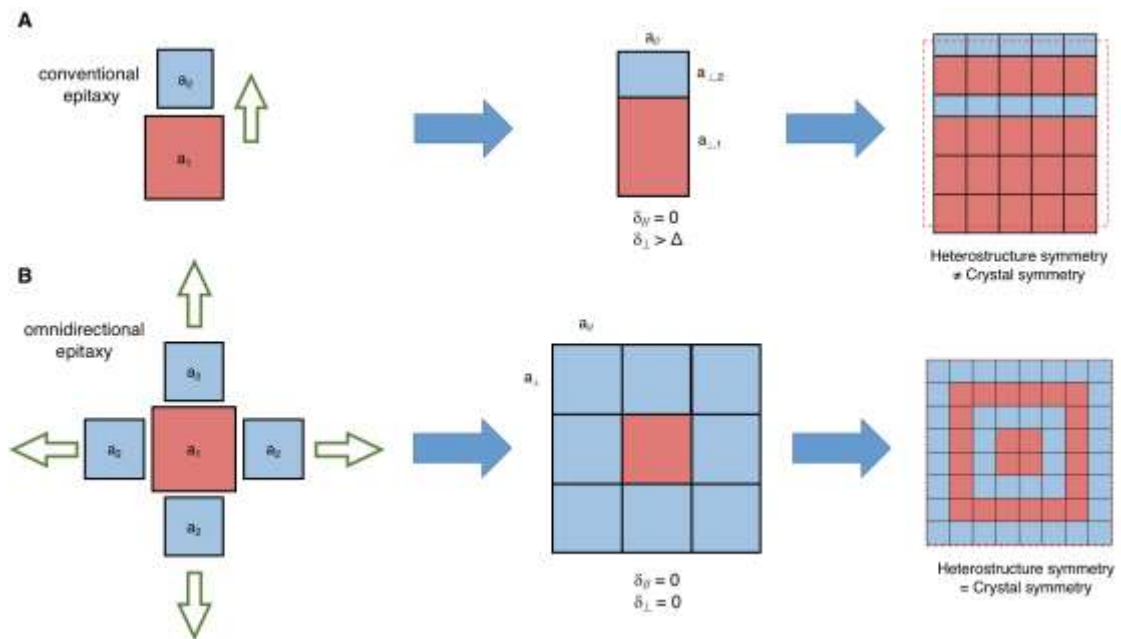


**Figure 4.8 Schematic of conventional and omnidirectional epitaxy.**

(A) Schematic of conventional unidirectional epitaxy and the resulting heterostructure with different symmetry from that of the original crystal. (B) Schematic of omnidirectional coherent epitaxy and the resulting heterostructure maintaining the same symmetry of the original crystal.

These observations were quantitatively predicted by coarse-grained simulations of these superlattices that account for both bond and angle interactions on an appropriate footing (Figure 4.9). In this regard, it is the inclusion of angular interactions in particular, which accounts for the shear stiffness inside the TMD superlattice and thereby introduces local frustration (analogous to the antiferromagnetic triangular-lattice Ising

model), that is key to predicting coherent omnidirectional epitaxy across the entire lattice as well as a small but non-vanishing  $\delta_{\perp}$ .

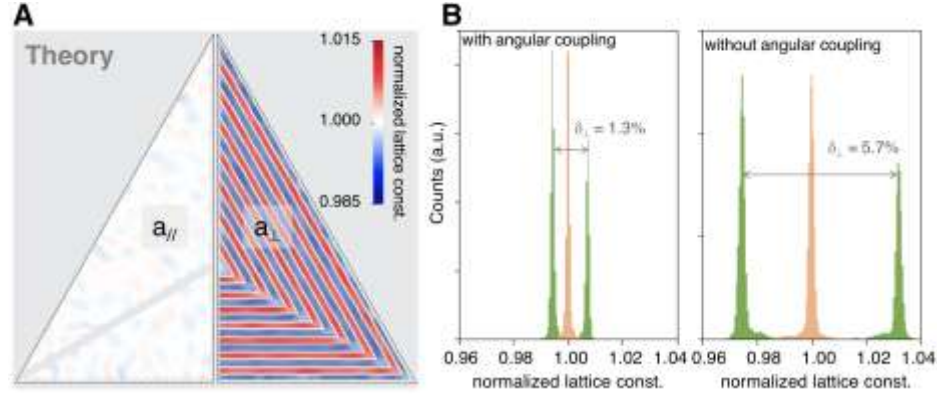


**Figure 9.9 Coarse-grained simulation of the coherent  $WS_2/WSe_2$  superlattice.**

(A) Composite maps of  $a_{\parallel}$  (left) and  $a_{\perp}$  (right) of a superlattice with ratio  $d_{WS_2}/d_{WSe_2} = 1.25$ , computed from a coarse-grained theoretical simulation. (B) Theoretical simulation results for the  $a_{\parallel}$  and  $a_{\perp}$  distributions. The addition of angular coupling terms significantly reduces  $\delta_{\perp}$  from 5.7% to 1.3%, in excellent agreement with the experimental observation of coherent epitaxy in both the parallel and perpendicular directions.

The coarse-grained force-field model used for studying the equilibrium state of the entire coherent TMD that accounts for nearest-neighbor bonding and angular interactions. In this approach, the atom types are “dressed W atoms” and can either be  $WS_2$  or  $WSe_2$  units centered at the corresponding W atomic position in the 2D superlattice. The total potential energy expression employed for the superlattice is  $E_{latt} = \frac{1}{2} \sum_{bonds} k_b (r - r_0)^2 + \frac{1}{2} \sum_{angles} k_{\theta} (\theta - \theta_0)^2$ , in which the first term represents a harmonic bond potential (with  $k_b$  and  $r_0$  representing the bond force constant and equilibrium bond distance, respectively) and the second term a harmonic angular potential (with  $k_{\theta}$  and  $\theta_0$  representing the angular force constant and equilibrium angle, respectively). With reasonable parameters in the model, we find excellent agreement

with the experimental results for  $a_{//}$  and  $a_{\perp}$ , as shown in Figure 4.6, A-C. More details on the simulation model can be found in Ref. 133.

## 4.5 Strain Engineering of Photoluminescence of $WS_2/WSe_2$

### Superlattices

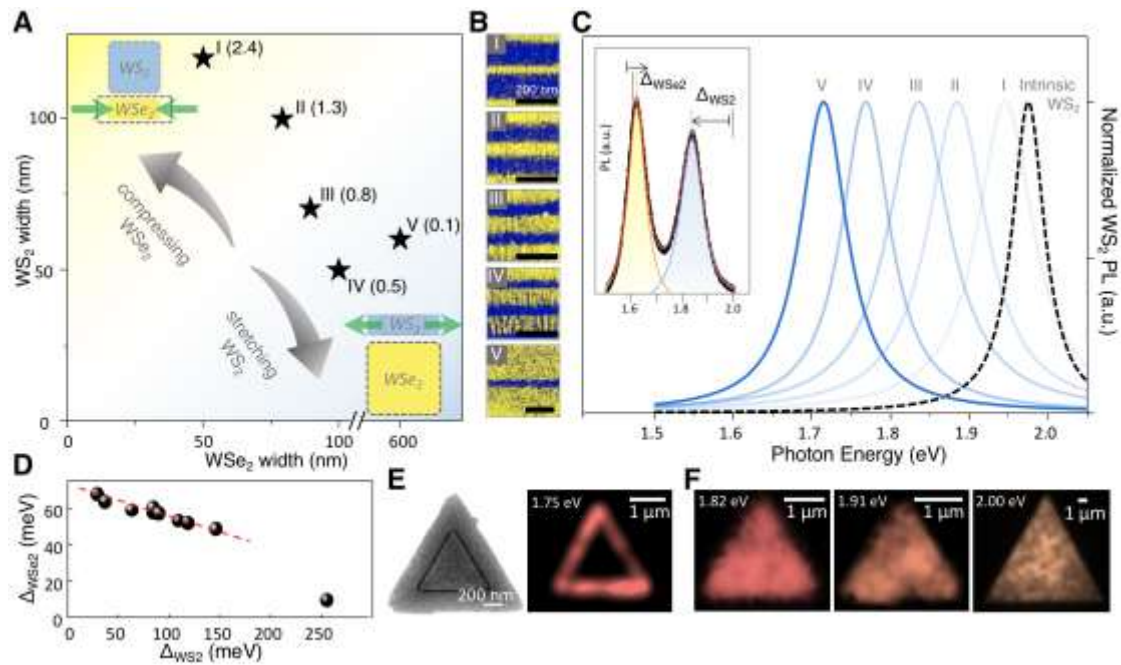


**Figure 4.10** Strain engineering of PL of  $WS_2/WSe_2$  superlattices.

(A) Plot of  $WS_2/WSe_2$  superlattices I to V with different ratios  $\rho = d_{WS_2}/d_{WSe_2}$  (values shown in parentheses). (Insets) Schematic of supercell dimension-dependent strain magnitude in the superlattice. (B) False-color SEM images of superlattices I to V. Scale bars, 200 nm. (C) Normalized PL spectra of  $WS_2$  for intrinsic  $WS_2$  (dashed line) and superlattices I to V. (Inset) a representative PL spectrum of a  $WS_2/WSe_2$  superlattice showing the  $WS_2$  peak red shifted by  $\Delta_{WS_2}$  and the  $WSe_2$  peak blue shifted by  $\Delta_{WSe_2}$ . (D) Plot of  $\Delta_{WSe_2} - \Delta_{WS_2}$  for  $WS_2/WSe_2$  superlattices with different supercell dimensions. (E) (Left) SEM image of a narrow  $WS_2$  stripe embedded in  $WSe_2$ . (Right) PL image of a heterostructure similar to the left, taken at photon energy of 1.75 eV. (F) PL images of two  $WS_2/WSe_2$  superlattices at photon energies near their  $WS_2$  peak positions (left and middle, at 1.82 eV and 1.91 eV, respectively) and an intrinsic monolayer  $WS_2$  (right, at 2.00 eV). Scale bars, 1  $\mu m$ .

This lattice coherence also resulted in a tensile (compressive) strain within the  $WS_2$  ( $WSe_2$ ) region in our superlattices, the magnitude of which varied depending on the

supercell dimensions. Figure 4.10A illustrates such strain control. For example, a smaller  $d_{WS_2}$  or larger  $d_{WSe_2}$  (with a small ratio  $\rho = d_{WS_2}/d_{WSe_2}$ ) increased the tensile strain in  $WS_2$  and decreased the compressive strain in  $WSe_2$  as it brought  $a_{//}$  and  $a_{\perp}$  closer to the intrinsic values for  $WSe_2$ . In addition, the band structure of both  $WS_2$  and  $WSe_2$  was sensitive to the applied strain—the size of the direct band gap decreased (increased) when subjected to tensile (compressive) strain [136–139].

This strain-dependent band structure allowed for broad tuning of the optical properties by superlattice design. Figure 4.10B shows the false-color SEM images of five representative  $WS_2$  (blue)/ $WSe_2$  (yellow) coherent superlattices I to V with different  $\rho$  (dimensions plotted in Figure 4.10A). The resulting photoluminescence (PL) spectra showed two peaks, with one corresponding to  $WS_2$  and the other to  $WSe_2$  (Figure 4.10C inset). However, the  $WS_2$  peak was red shifted from the intrinsic peak energy of 1.97 eV by  $\Delta_{WS_2}$  while the  $WSe_2$  peak was blue shifted from the intrinsic value of 1.61 eV by  $\Delta_{WSe_2}$ . Figure 4.10C compares the normalized  $WS_2$  peaks measured from superlattices I to V (each extracted from the full PL spectra) to the intrinsic  $WS_2$  peak (dashed curve). Superlattices with smaller  $\rho$  showed larger  $\Delta_{WS_2}$ , as large as 250 meV. Figure 4.10D further plots  $\Delta_{WS_2}$  vs.  $\Delta_{WSe_2}$  for additional superlattices with different supercell dimensions.

These PL characteristics were consistent with the strain engineered by the superlattice design. The positive values for both  $\Delta_{WS_2}$  and  $\Delta_{WSe_2}$  confirmed the tensile (compressive) strain in  $WS_2$  ( $WSe_2$ ). Their magnitudes showed a negative correlation, which is consistent with their expected negatively correlated strain magnitude (Figure 4.10A). The largest  $\Delta_{WS_2}$  of 250 meV, corresponding to a 3.4% uniaxial strain or a 1.4%

isotropic biaxial strain [136], was consistent with the large tensile strain expected from superlattice V with a small  $\rho = 0.1$ . Moreover, the PL image (Figure 4.10E right; taken at 1.75 eV) confirmed that the highly red-shifted WS<sub>2</sub> PL peak indeed originated from the strained WS<sub>2</sub> region (SEM image of a similarly grown sample shown in Figure 4.10E left). In general, superlattices with supercell dimensions below the diffraction limit (Figure 4.10F, left and middle) showed uniform PL intensities at their respective peak energies over the entire structure, with a similar uniformity compared to intrinsic WS<sub>2</sub> (Figure 4.10F, right).

## ***4.6 Compressive Strain Induced Out-of-Plane Ripples in WSe<sub>2</sub>***

### ***Energetics Interplay Between Elastic Strain Energy and van der Waals Energies***

Strained thin films relax through out-of-plane deformations such as wrinkles and ripples, which makes these films non-flat and their edges curved [140–142]. However, our ultrathin superlattices maintained lattice coherence and symmetry, despite being highly strained and their edges being under alternating compressive and tensile stress during growth, because of strong van der Waals (vdW) interactions between the superlattice and the underlying growth substrate (SiO<sub>2</sub> in our experiment) [101, 143], which keep the 2D superlattice flat. Figure 4.11A plots the theoretically calculated total energy ( $E_{\text{tot}}$ , circles) per WSe<sub>2</sub> of a strained WSe<sub>2</sub> monolayer on SiO<sub>2</sub> as a function of the out-of-plane ripple height ( $A$ , measured from peak to valley; see schematic in Figure 4.11B).  $E_{\text{tot}}$  consists of the elastic strain energy ( $E_{\text{el}}$ , triangles), computed using a macroscopic elastic energy model (that accounts for both stretching and bending energy components in an ultrathin film), and the interlayer vdW binding energy between the

WSe<sub>2</sub> and SiO<sub>2</sub> ( $E_{vdw}$ , squares), computed using an all-atom quantum-mechanical vdW energy model (see Ref. 133 for details). Although the rippled state ( $A \approx 3$  nm) that relaxes the compressive strain is lowest in energy, the energetic profile shows another minimum at  $A = 0$  nm, corresponding to the flat state. These two states have similar energies because the reduction in  $E_{el}$  roughly equals the increase in  $E_{vdw}$  for the rippled state.

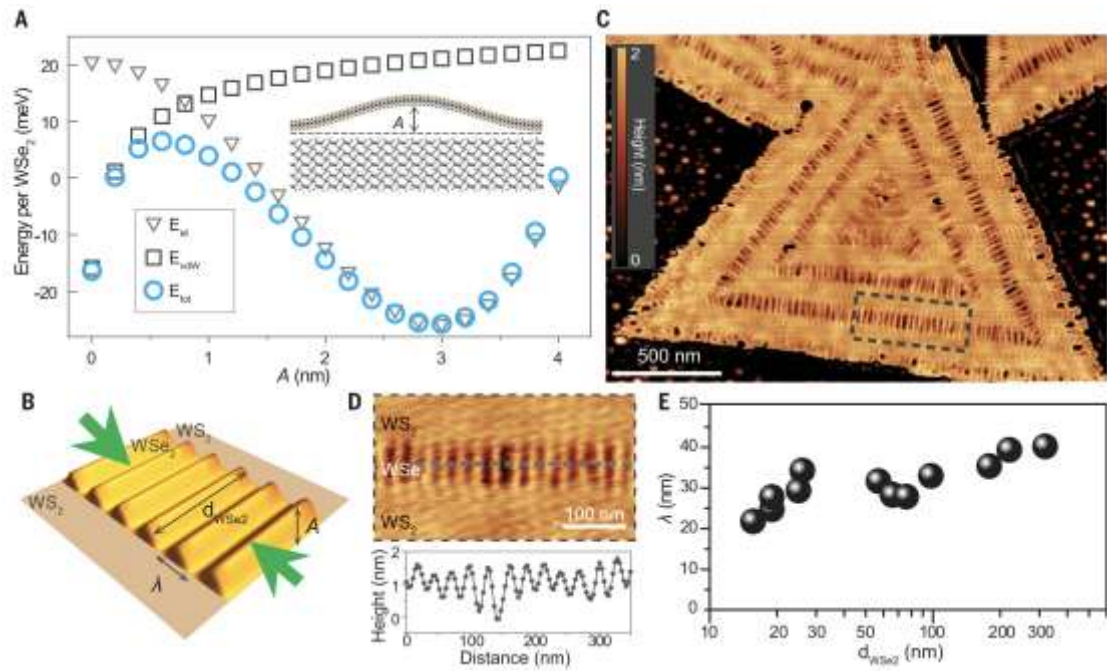


**Figure 4.11 Formation of out-of-plane ripples in WSe<sub>2</sub>.**

(A) Theoretically calculated elastic strain energy ( $E_{el}$ ), interlayer van der Waals binding energy ( $E_{vdw}$ ), and total energy ( $E_{tot}$ ) per WSe<sub>2</sub> as a function of WSe<sub>2</sub> ripple height ( $A$ ) ( $E_{el}$  and  $E_{vdw}$  shifted by -32 meV and 53 meV, respectively, for clarity). Inset: schematic of the rippled WSe<sub>2</sub> on substrate. (B) Schematic of rippled WSe<sub>2</sub> and flat WS<sub>2</sub>, where the ripple wavelength ( $\lambda$ ),  $A$ , and  $d_{WSe_2}$  are indicated. (C) AFM height image of a representative WS<sub>2</sub>/WSe<sub>2</sub> superlattice. Scale bar, 500 nm. (D) Enlarged AFM image of the boxed area in (C) and height profile along the dashed line. Scale bar, 100 nm. (E)  $\lambda$  of superlattices with different  $d_{WSe_2}$ .

The rippled and flat states are separated by an energetic barrier (with an activation energy of 10 to 20 meV per WSe<sub>2</sub>), because the increase in  $A$  in the regime  $0 < A < 1$  nm rapidly destabilizes  $E_{vdw}$  without substantially stabilizing  $E_{el}$ . Figure 4.11A thus

predicts that the attractive vdW force from the substrate keeps WSe<sub>2</sub> flat and that the transition from the flat to rippled state can only occur in the presence of a substantial perturbation. As a result, these theoretical findings suggest that the synthesis conditions in our experiment, which maintained a constant growth environment with no strong perturbations, allowed the superlattice to remain flat and the growth edge straight during growth.

### *Formation of Ripples in WSe<sub>2</sub>*

The superlattices reported herein were subjected to a cool-down process after growth, from a relatively high growth temperature (600 °C) to room temperature. This process could perturb the samples (e.g., thermal expansion/contraction of the superlattice and SiO<sub>2</sub>) and induce ripples in WSe<sub>2</sub>, which is what we observed in our samples. The atomic force microscope (AFM) height image of a representative WS<sub>2</sub>/WSe<sub>2</sub> superlattice (Figure 4.11C) shows out-of-plane ripples in WSe<sub>2</sub> (schematically illustrated in Figure 4.11B). These ripples ran continuously across the WSe<sub>2</sub> stripes only and were periodic along the heterointerfaces, as shown in the enlarged AFM image (Figure 4.11D top). The peak-to-valley height ( $A$ ) was between 1 and 2 nm (measured from the AFM profile shown in Figure 4.11D bottom). This value is surprisingly near that of  $A$  for the lowest energy state in Figure 4.11A, despite the use of a simple energetic model and an idealized superlattice geometry. We also observed that the ripple wavelengths ( $\lambda$ ) for superlattices with different  $d_{\text{WSe}_2}$  remained relatively constant (near 30 nm, as shown in Figure 4.11E), with little dependence on  $d_{\text{WSe}_2}$  over one order of magnitude (ranging from 20 to 320 nm). This result suggests that the

presence of WS<sub>2</sub>/WSe<sub>2</sub> interfaces had minimal effect on the energetics of the ripple formation in this regime, and that the constant compressive strain in WSe<sub>2</sub> (even up to  $d_{\text{WSe}_2} = 320$  nm) was released through rippling. This finding also explains the smaller range of  $\Delta_{\text{WSe}_2}$  shown in Figure 4.10D.

### *Long Coherence Length of 2D Epitaxy*

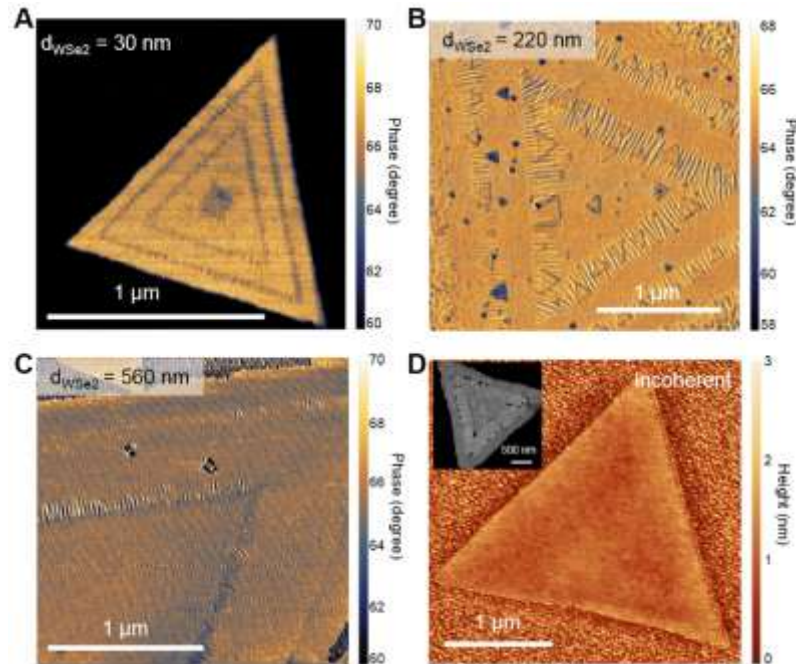


**Figure 4.12 AFM images of WS<sub>2</sub>/WSe<sub>2</sub> heterostructures.**

(A-C) AFM phase images of WS<sub>2</sub>/WSe<sub>2</sub> heterostructures with different  $d_{\text{WSe}_2}$  of 30, 220, and 560 nm, respectively. Ripples are not continuous across the entire WSe<sub>2</sub> region in the superlattice with  $d_{\text{WSe}_2}$  of 560 nm. (D) AFM height image of an incoherent WS<sub>2</sub>/WSe<sub>2</sub> heterostructures showing no out-of-plane ripples. Inset: DF-TEM image of a similar sample showing the WS<sub>2</sub>/WSe<sub>2</sub>/WS<sub>2</sub> composition.

For superlattices with  $d_{\text{WSe}_2} > 320$  nm, however, the periodic ripples were no longer continuous across the WSe<sub>2</sub> area (see Figure 4.12). This difference indicates the presence of an alternative strain relaxation mechanism, including the formation of misfit dislocations and a coherence length of  $\sim 320$  nm for our WS<sub>2</sub>/WSe<sub>2</sub> superlattices. This

coherence length was substantially greater than the critical thickness of 2 nm for the Si/Ge system with a similar  $\Delta \sim 4\%$  [144], as well as the critical thickness for the  $\text{WS}_2/\text{WSe}_2$  system estimated using the People-Bean model (below 20 nm, see Figure 4.13) [145]. We note that the People-Bean model ( $h_c \cong \frac{1-\nu}{1+\nu} \frac{1}{16\pi\sqrt{2}} \frac{b^2}{a} \frac{1}{\Delta^2} \ln\left[\frac{h_c}{b}\right]$ ), where  $a = 0.329$  nm is the lattice constant of  $\text{WSe}_2$ .  $b$  is the length of Burgers vector, and we take  $b = a = 0.329$  nm as it corresponds to the easiest formed misfit dislocation;  $\nu$  is the Poisson's ratio of  $\text{WSe}_2$ ) is known to overestimate the critical thickness for  $\Delta < 6.2\%$  [146]. A full explanation for such a long coherence length would require a general theory optimized for 2D, which is currently lacking. However, we expect that our stable superlattice growth conditions and a larger energetic barrier for dislocation formation in 2D system may account for the long coherence length. For example, there are limited configurations of covalent bonding for dislocations in 2D systems and no screw dislocations.

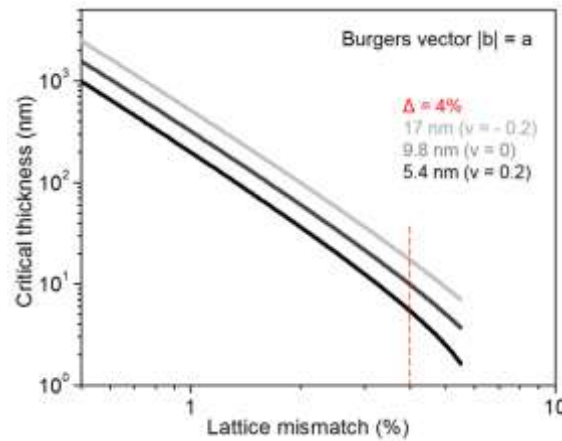


**Figure 4.13 Critical thickness analysis.**

Critical thickness as a function of lattice mismatches, for  $\nu = -0.2$  (light gray), 0 (gray), and 0.2 (black), based on the People-Bean model. A critical thickness of 17 nm ( $\nu = -0.2$ ), 9.8 nm ( $\nu = 0$ ), and 5.4 nm ( $\nu = 0.2$ ) is estimated for the  $\text{WS}_2/\text{WSe}_2$  epitaxial system with lattice mismatch of 4%.

## 4.7 *Summary*

In this chapter we presented our work on coherent monolayer TMD superlattices with nanoscale-controlled supercell dimensions and lattice coherence maintained over the entire structure. Grown by an omnidirectional epitaxy, these superlattices display a surprisingly isotropic lattice structure, despite large lattice mismatches. Broad PL peak shifts as large as 250 meV were achieved by precise strain engineering via the nanoscale supercell dimension control. These monolayer superlattices display uniform PL intensity due to the supercell dimension being smaller than the diffraction limit. The compressive epitaxial strain further results in ripple formation in WSe<sub>2</sub>.

Our demonstration of monolayer TMD superlattice represent the atomic-thickness monolayer limit of heterostructures. Monolayer heterostructures can be readily synthesized using the modulated MOCVD technique, allowing for the production of complex device in the monolayer limit. The strain induced ripples in these monolayer TMDs can be used to modulate the spatial mechanical properties, opening up the possibility for creating mechanical metamaterials, as well as creating controlled folding for 3D objects. Furthermore, the omnidirectional epitaxy not only presents a powerful framework for the epitaxial synthesis of nanomaterials and the engineering of their properties, but also opens up the possibility of a new interdisciplinary research direction as our coherent superlattice is crystalline yet highly deformable.

## CHAPTER 5

### HIGH PERFORMANCE MONOLAYER DEVICES

#### ***5.1 Introduction***

So far, we have discussed the synthesis of large-scale films and coherent superlattices of TMDs, both in the monolayer limit. These monolayers serve as an ideal material for realizing various electronic and optoelectronic devices with unique advantages. For instance, transistors based on these monolayer TMDs possess lower source-drain leakage current due to the confinement of current in the atomic layer and the larger in-plane electron effective mass ( $m^* \sim 0.55m_0$  for MoS<sub>2</sub>, and  $m^* \sim 0.19m_0$  for Si [100]) [34, 147, 148]. On the other hand, controlling the defect density, especially achieving low defect density, has been a major effort in the development of high-performance heterostructure devices (Nobel Prize in Physics, 2000) [149]. The coherent monolayer TMD heterostructures discussed in the previous chapter present an unprecedented material system for the realization of high-performance heterostructure devices in the atomic-thickness limit.

While monolayer TMD FETs can be realized with conventional metal electrodes (such as gold) as we showed earlier in Chapter 3, the bulky electrodes increase the overall thickness of the device, making the further integration of such atomically-thin systems challenging. To generate fully functioning circuits in the atomic-thickness limit, creating all-monolayer-devices consisting of semiconductor-semiconductor and metal-semiconductor heterostructures is indispensable.

In this chapter, which is largely adapted from Ref. 133 and Ref. 150, we present our work on high-performance monolayer devices of semiconductor/semiconductor (e.g. WS<sub>2</sub>-WSe<sub>2</sub>) and metal/semiconductor (e.g. graphene-MoS<sub>2</sub>) heterostructures. First, we fabricated and examined three types of devices based on our coherent semiconductor heterostructures—p-n diodes with high rectification ratios ( $>10^6$ ), LEDs, and double heterostructure (DH) transistors, where the coherent heterointerfaces were generated between WS<sub>2</sub> (*n*-type, in general) and WSe<sub>2</sub> (*p*-type). Second, we developed a scalable method to produce monolayer graphene-TMDs as a representative metal-semiconductor interface. With wafer-scale homogeneity, the graphene is laterally connected to monolayer MoS<sub>2</sub> and WS<sub>2</sub>, and act as ohmic edge contacts with a low average contact resistance of 30 k $\Omega$ · $\mu$ m.

## ***5.2 Monolayer WSe<sub>2</sub>/WS<sub>2</sub> P-N Diodes***

Our 2D superlattices have dislocation-free heterointerfaces with precisely controlled nanoscale supercell dimensions. These two advanced properties are crucial for producing practical devices that are difficult to produce otherwise. To demonstrate this, we have fabricated and examined three types of devices based on our coherent heterostructures—p-n diodes, LEDs, and double heterostructure (DH) transistors, where the coherent heterointerfaces were generated between WS<sub>2</sub> (*n*-type, in general) and WSe<sub>2</sub> (*p*-type).

### ***High-Performance P-N Diodes***

We have successfully fabricated electrical devices that include only one WSe<sub>2</sub>-WS<sub>2</sub> (p-n) heterojunction between two metal electrodes (Figure 5.1A, inset). A representative

p-n diode shows high forward-bias current ( $>10 \mu\text{A}$ ) and low reverse-bias current ( $\sim 10 \text{ pA}$ ), producing a high rectification ratio ( $>10^6$ ), as illustrated in Figure 5.1. The high performance for our p-n diodes is consistent with the dislocation-free coherent heterointerfaces, as the coherent interfaces could minimize the scattering of carriers by dislocations, resulting in a higher electrical conductivity under forward bias. Furthermore, the defect-assisted hopping transport of charge carriers will be minimized, which accounts for a lower conductivity under reverse bias.

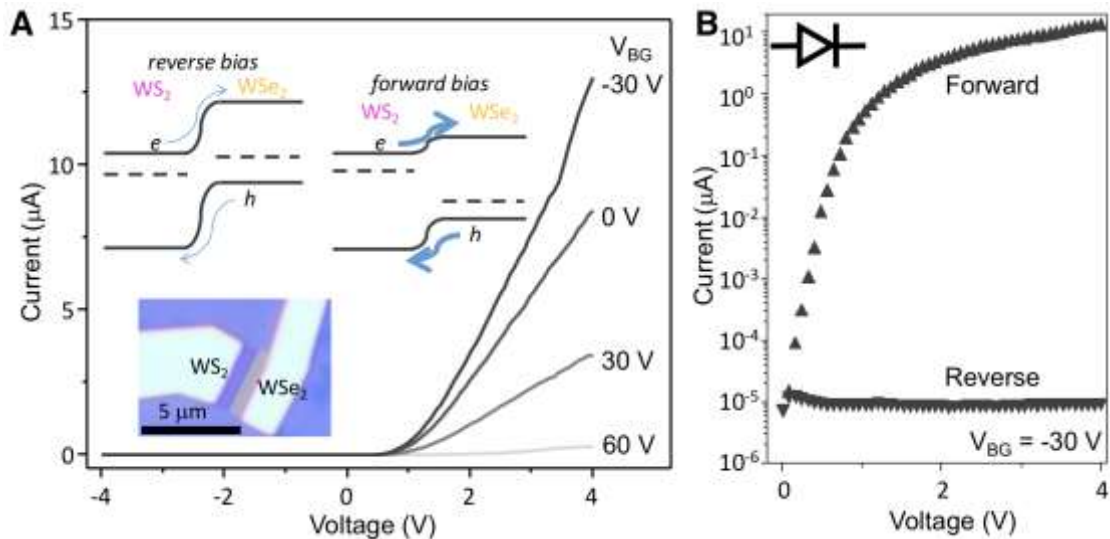


**Figure 5.1 Electrical transport of WSe<sub>2</sub>/WS<sub>2</sub> p-n diodes without encapsulation.** (A) Current-Voltage (*I-V*) curves for a WSe<sub>2</sub>-WS<sub>2</sub> p-n diode under different V<sub>BG</sub>. (B) Forward and reverse *I-V* curves for the same device in (A) at V<sub>BG</sub> of -30V showing a rectification ratio of 10<sup>6</sup>.

### *Enhanced Device Lifetime by Hexagonal Boron Nitride Encapsulation*

In the devices fabricated and measured above, monolayer WS<sub>2</sub> and WSe<sub>2</sub> was exposed to the ambient during measurements. As a result, the devices were not stable and did not show constant behavior in repeated measurements, possibly due to the oxidation and adsorption of chemical species on the channel surface. In order to achieve high-performance heterostructure devices, we fabricated p-n diode devices with

hexagonal boron nitride (*h*-BN) encapsulation, which has been the standard method for producing 2D device with high electrical quality [40, 151] and sharp band-to-band photoluminescence spectral peaks [152–154].

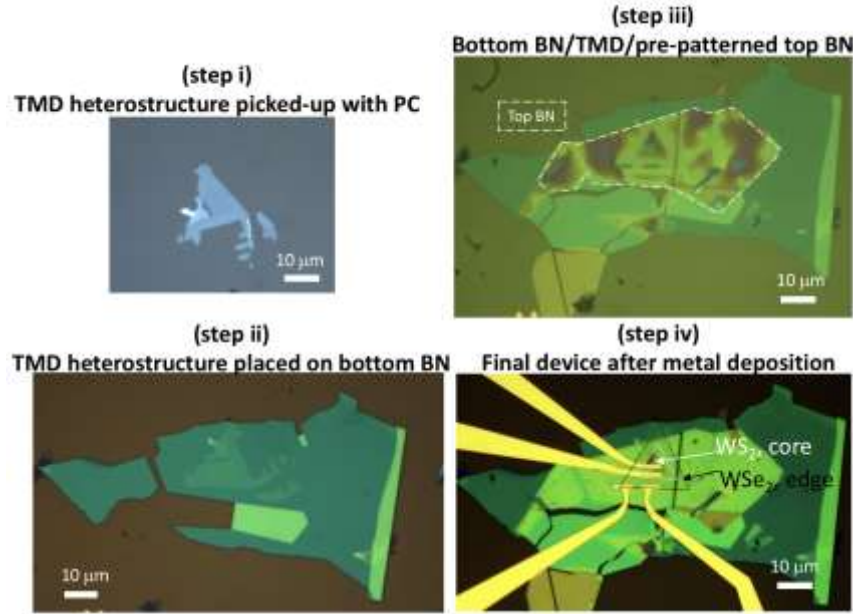
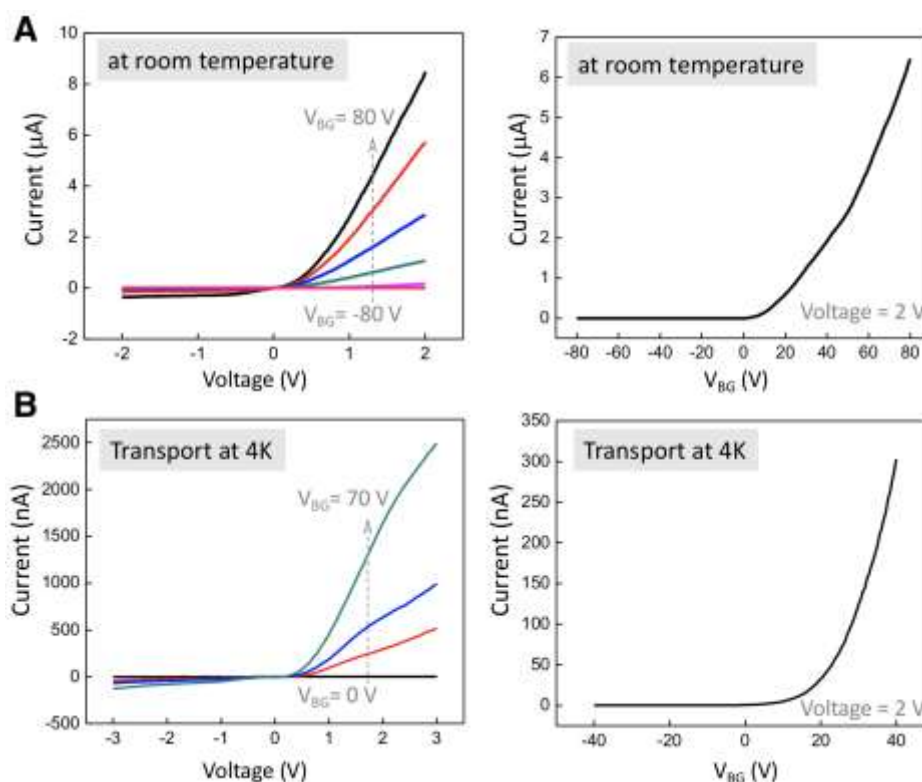


**Figure 5.2 Micrographs of fabrication of *h*-BN encapsulated TMD devices.**

Monolayer WSe<sub>2</sub>-WS<sub>2</sub> heterostructure was picked-up by PC and sandwiched between bottom and top (pre-patterned) *h*-BN flakes (both ~ 30 nm). Ti/Au was used for electrical contacts to the TMD heterostructure device.

Figure 5.2 shows optical micrographs after different stages of the *h*-BN encapsulated WSe<sub>2</sub>-WS<sub>2</sub> device fabrication using dry transfer method [155]. (i) the WSe<sub>2</sub>-WS<sub>2</sub> heterostructure was picked up with polycarbonate (PC) from its growth substrate; (ii) the WSe<sub>2</sub>-WS<sub>2</sub> heterostructure was placed on top of a bottom *h*-BN flake; (iii) a pre-patterned top *h*-BN is aligned and placed on top of the whole stack, forming a vertical BN-TMD-BN sandwich structure; (iv) 0.5 nm Ti / 50 nm Au were deposited to form contacts to both WS<sub>2</sub> and WSe<sub>2</sub> via the pre-patterned voids on top *h*-BN.

**Figure 5.3 Electrical transport of WSe<sub>2</sub>/WS<sub>2</sub> p-n diodes with *h*-BN encapsulation.** I-V curves under different V<sub>BG</sub> and V<sub>BG</sub> dependence for a *h*-BN encapsulated WSe<sub>2</sub>-WS<sub>2</sub> p-n diode, measured at room temperature (A) and 4K (B), respectively.



After *h*-BN encapsulation, the entire device became significantly more stable—its conduction level was highly consistent in repeated measurements. We examined the electrical transports at both room temperature and 4K (results shown in Figure 5.3). Under both measurement conditions, the devices show expected rectification behavior (consistent with devices without encapsulation shown in Figure 5.1). Notably, the device showed decent conduction even at 4K, suggesting the high quality electrical contacts from electrodes to both WS<sub>2</sub> and WSe<sub>2</sub>, which is often challenging but essential for high-performance devices at cryogenic temperatures. Interestingly, the encapsulated device showed an opposite gate dependence compared with the non-encapsulated device. This varied gate dependence implies the monolayer materials' sensitivity to surface treatments/processing, which can be utilized in order to control the device properties over a broad range.

## Electroluminescence of Monolayer WSe<sub>2</sub>/WS<sub>2</sub> P-N Diodes (LEDs)

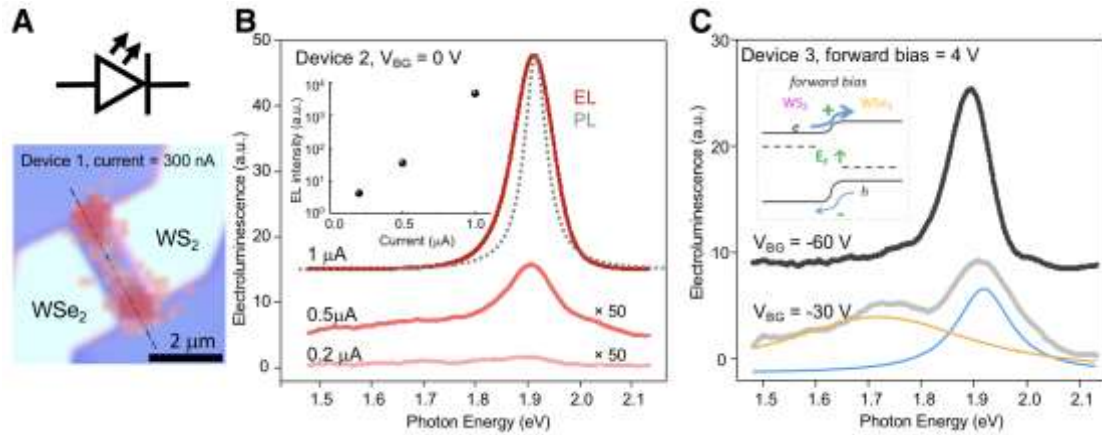


**Figure 5.4 Electroluminescence of WSe<sub>2</sub>/WS<sub>2</sub> p-n diodes without encapsulation.**

(A) EL intensity (red) map overlaid with optical micrograph of the p-n diode device, showing the EL centered at WS<sub>2</sub>-WSe<sub>2</sub> heterointerface (marked with dashed line). (B) EL spectra (red) under current  $I = 0.2, 0.5,$  and  $1 \mu\text{A}$ , respectively, together with PL spectrum (grey). Inset: EL intensity for corresponding current intensity, showing an exponential dependence. (C) EL spectra recorded under  $V_{\text{BG}} = -60$  and  $-30 \text{ V}$ , with fitted peaks (blue and orange) and the band diagram shown in inset. All curves are offset for clarity.

We further observed strong electroluminescence (EL) from the p-n diodes. The false-color EL image overlaid on the optical micrograph of the p-n heterostructure device confirms that the luminescence originates from the heterointerface between WS<sub>2</sub> and WSe<sub>2</sub> (Figure 5.4A, interface marked with the dashed line). The EL is observed under the forward-bias condition, and its intensity dramatically increases with the injected current ( $I$ ). For example, the EL from the device in Figure 5.4B increases by three orders of magnitude when  $I$  increases only by a factor of 5 (inset, Figure 5.4B). The EL spectrum shows a peak similar to the PL peak from WS<sub>2</sub>, which suggests that the light emission is likely to originate from the  $e$ - $h$  recombination within WS<sub>2</sub>. These observed features for EL and the backgate dependence (Figure 5.4C) matches very well with the expected band alignment (Figure 5.4C, inset). The EL spectra at more positive

gate bias (-30V) show multiple peaks suggesting that electrons (injected from WS<sub>2</sub> side) and holes (injected from WSe<sub>2</sub> side) recombine near the WS<sub>2</sub>-WSe<sub>2</sub> heterointerface. However, it produces only a single peak from WS<sub>2</sub> under a more positive gate bias (-60V) as the hole carrier density increases in our device and dominates the current flow across the junction (into WS<sub>2</sub>).

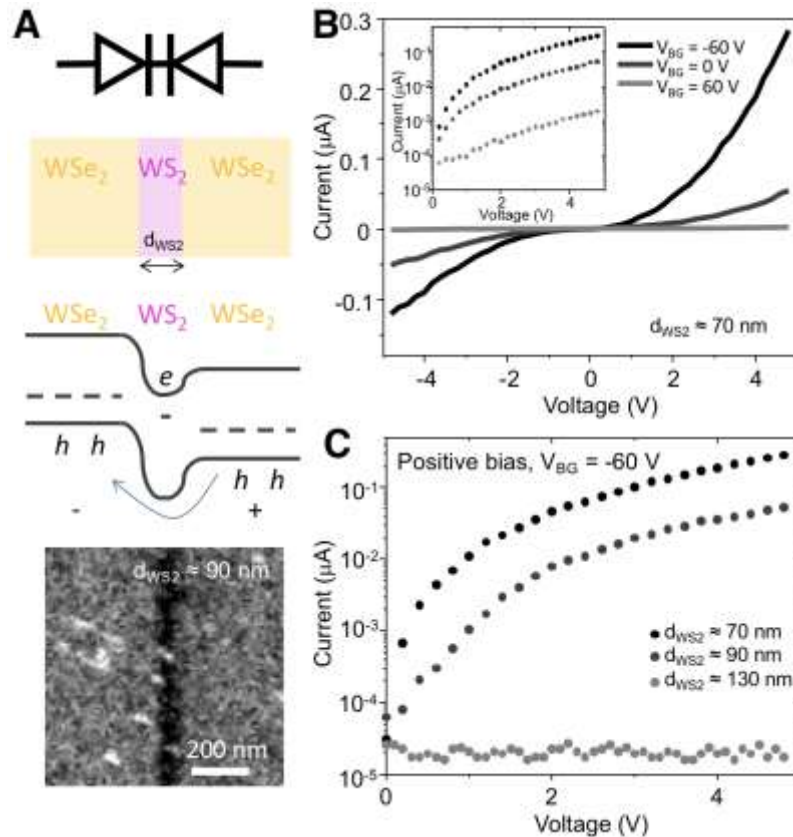


**Figure 5.5 Electrical transport of WSe<sub>2</sub>/WS<sub>2</sub>/WSe<sub>2</sub> double heterostructures.**

(A) From top to bottom: symbol, schematic, band diagram of WSe<sub>2</sub>-WS<sub>2</sub>-WSe<sub>2</sub> double heterostructure (DH), and an SEM image of a representative DH device with  $d_{WS_2} \approx 90$  nm. (B)  $I$ - $V$  curves for a DH device with  $d_{WS_2} \approx 70$  nm under different  $V_{BG}$ . (C)  $I$ - $V$  curves for three DH devices with  $d_{WS_2} \approx 70, 90,$  and  $130$  nm, respectively.

The high current needed for EL and the efficient radiative recombination both require the absence of dislocations. Therefore, the observation of EL suggests that the coherent heterointerface is crucial for high-performance LEDs. We note that our devices

are directly fabricated on the SiO<sub>2</sub>/Si growth substrate without any encapsulation and the EL measurements were performed under ambient conditions. This suggests that its performance (brightness and stability) may be further improved, which calls for more comprehensive EL studies in the future to fully understand and optimize the optoelectronic properties of our coherent heterostructures.

### **5.3 Double Heterostructure (DH) Transistors**

We successfully fabricated 2D double heterostructure devices (Nobel Prize in Physics, 2000) [149], based on double coherent heterojunctions (WSe<sub>2</sub>-WS<sub>2</sub>-WSe<sub>2</sub>) with the width of middle part ( $d_{WS_2}$ ) very narrow and precisely controlled. The schematic and band diagram are depicted in Figure 5.5A, together with an SEM image of a representative DH device with  $d_{WS_2} \approx 90$  nm. Our DH devices (over 10 of such devices were studied) show symmetric, nonlinear  $I$ - $V$  characteristics with no rectification behavior (Figure 5.5B), as expected from their symmetric configuration. Their  $p$ -type transport is consistent with the band diagram shown in Figure 5.5A, where the hole is the main carrier and WS<sub>2</sub> region acts as a barrier. As these DH devices are conceptually similar to double-diodes connected in opposite directions, they may conduct only when the middle region is narrow with the device conductivity strongly dependent on  $d_{WS_2}$ . This is indeed what we observe from our devices. (Figure 5.5C) The device with  $d_{WS_2} \approx 70$ nm is approximately one order of magnitude more conductive than the device with  $d_{WS_2} \approx 90$ nm, and we were unable to observe conduction for devices with  $d_{WS_2}$  larger than 130 nm. This is also consistent with the depletion width of  $\sim 320$  nm for TMD lateral heterostructures reported [71]. Our demonstration of double

heterostructures provides an example for building devices with designed band structures with excellent dimension control, which would stimulate further exploration of complex device applications.

#### ***5.4 Monolayer Transistor: Metal-Semiconductor Heterojunctions***

While the above devices show the promise of monolayer devices based on TMD/TMD heterostructures, the lack of monolayer metallic components in these devices limits their integration while maintain the atomic thickness. In the following section, which is adapted from Ref. 150, we present our work on integrating graphene, a monolayer metal, with TMDs in the lateral direction to serve as high-performance one-dimensional electrical contact.

Even though monolayer two-dimensional (2D) materials [9, 39] such as graphene [46] and transition metal dichalcogenides (TMDs) [156] show promising results towards atomically-thin circuitry [127, 156–162], the contact volume and resistance often dominate over the total device volume and resistance. There are two fundamentally different contact interface geometries for 2D materials: top contacts and edge contacts (Figure 5.6A) [163, 164]. Conventional methods use 3D metallic electrodes to top-contact monolayer 2D materials. Recent developments have shown that low contact resistance is achievable in this configuration [103, 107, 165–172], but the total electrode volume is an intrinsic problem for this approach. Graphene top-contacts can provide much smaller volumes with low contact resistances when they have sufficiently large contact areas [40, 173]. However, due to the van der Waals gap between graphene and the TMD [164, 174, 175], the contact resistance increases

dramatically as the length of the graphene top contact is reduced below the transfer length to the tens of nm scale [176].

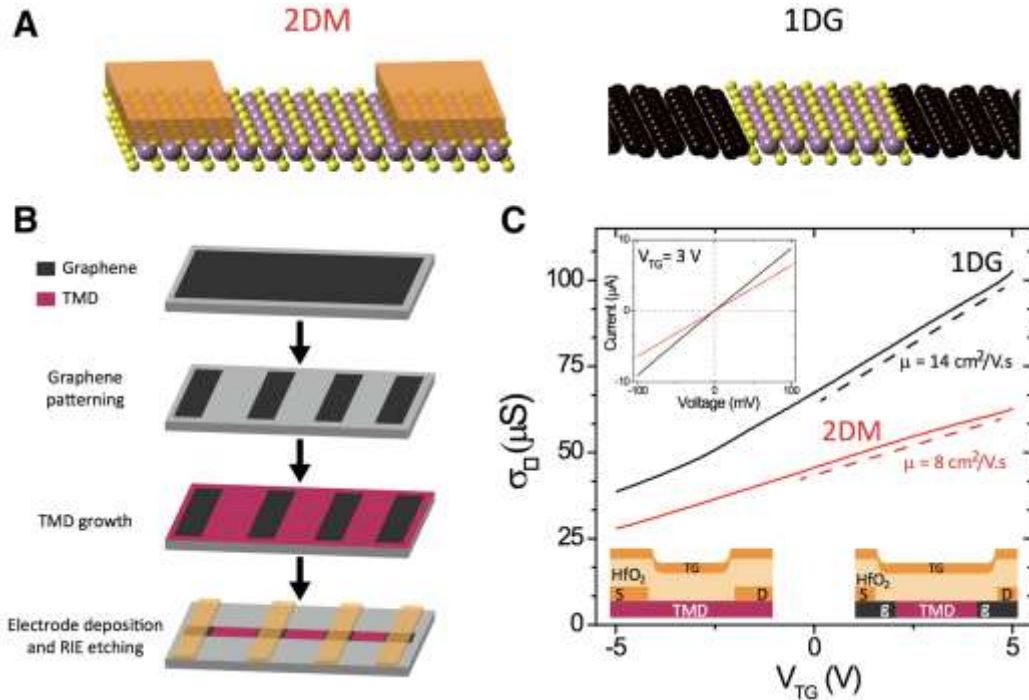


**Figure 5.6 Graphene-TMD lateral heterostructures using graphene as contact.** (A) Schematic illustration of metal top (2DM) contacts (left) and graphene edge (1DG) contacts (right) for TMD devices. (B) The large-scale growth and fabrication process for producing TMD transistor arrays with 1DG edge contacts. (C) Top gate voltage ( $V_{\text{TG}}$ ) dependence of the two-terminal sheet conductance ( $\sigma_{\square}$ ) measured from MoS<sub>2</sub> devices (length 22  $\mu\text{m}$  and width 20  $\mu\text{m}$ ) with 1DG contacts (black curve) and with 2DM electrodes (red curve; contact dimensions 23  $\mu\text{m} \times 22 \mu\text{m} \times 55 \text{ nm}$ ). (Top inset) IV characteristics for the two devices at  $V_{\text{TG}} = 3 \text{ V}$ . (Bottom insets) Cross-sectional device schematics for the devices with 2DM (left) and 1DG (right) contacts, showing the TMD channel, the graphene contacts (g), and the source (S), drain (D) and top gate (TG) electrodes with the insulating HfO<sub>2</sub> layer.

Edge contacts, on the other hand, offer the potential for efficient carrier injection to atomically thin materials despite a much smaller contact area defined by their atomic thickness [174]. Conventional metal electrodes have been successfully used to make edge contacts to graphene [177], but the large electrodes still dominate the device volume. Another approach, which alters the crystalline phase of a 2D TMD

semiconductor to make it metallic, generates an edge contact to the TMD with small contact volume and resistance [178–180]. However, it relies on a phase that is metastable, and it uses methods that are customized for the specific chemical composition of the TMD.

To realize the full potential of atomically-thin TMD materials for electronics will require contacts with a low intrinsic volume that are scalable with low contact resistances, chemically and thermally stable, and versatile towards use with different TMD materials. In this section, we demonstrate edge contacts to monolayer TMDs that fulfill these requirements by using monolayer graphene as the electrode. We fabricate laterally-stitched graphene/TMD heterostructures using a scalable and patternable growth method with homogeneous quality over the entire substrate. The resulting one-dimensional graphene (1DG) contacts show low contact resistance ( $R_c$ ) of approximately  $30 \text{ k}\Omega\cdot\mu\text{m}$ , with ohmic behavior down to liquid helium temperatures, while adding the least possible additional volume to the devices.

### ***Monolayer Graphene-TMD Lateral Heterostructures***

Figure 5.6B summarizes our approach. A monolayer graphene film, grown by chemical vapor deposition (CVD) [181] is transferred onto a  $\text{SiO}_2/\text{Si}$  substrate and patterned by photolithography and oxygen plasma etching. The key step for making lateral connections between the graphene and a TMD is the use of the highly controllable MOCVD process (discussed in Chapter 3) for the growth of single layer TMDs ( $\text{MoS}_2$  or  $\text{WS}_2$ ) from the graphene edges, causing the ensuing TMD growth to occur only on the exposed  $\text{SiO}_2$  surface and not on the graphene (see Ref. 150 for more

details). The resulting heterostructure film is then further processed to fabricate an array of devices that use graphene as one-dimensional edge contacts to the TMD channels.

In Figure 5.6C we plot the gate-dependent 2-probe conductance of a representative MoS<sub>2</sub> device (22 μm long) contacted by graphene electrodes (20 μm wide) and we compare it to the results from a device with conventional metal top (2DM) contacts with dimensions 23 μm × 22 μm × 55 nm. All results shown here and discussed below were obtained at room temperature and ambient conditions, unless otherwise noted. Both sets of contacts show ohmic behavior (see inset).

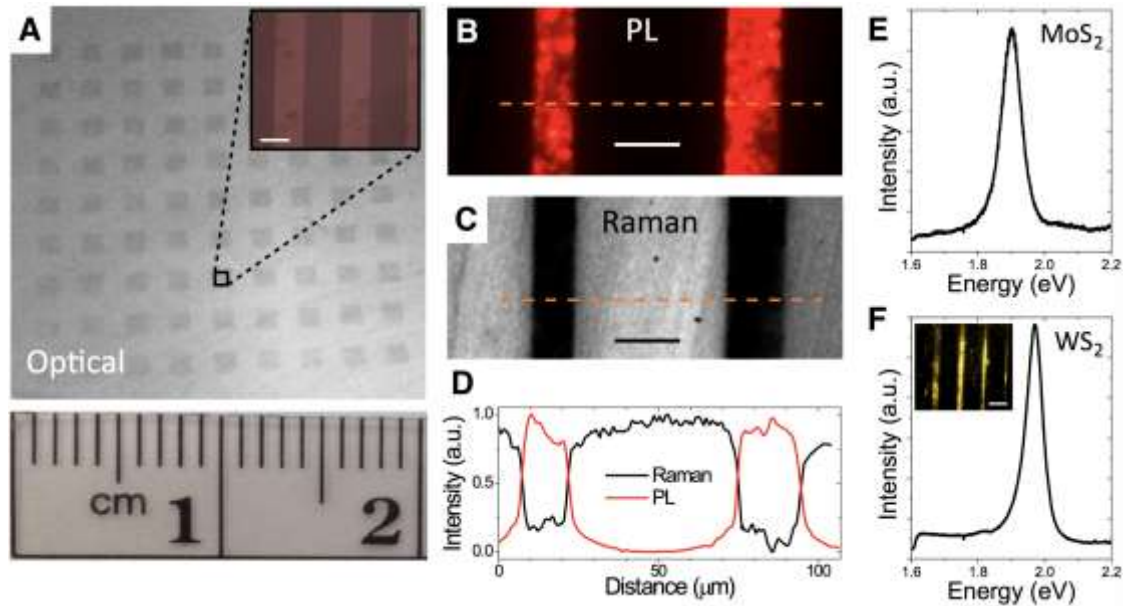


**Figure 5.7 Graphene-TMD heterostructures with large scale uniformity.**

(A) Optical image of a typical growth substrate over a 2 cm × 2 cm area. Each dark grey square contains 20 graphene stripes connected by a monolayer MoS<sub>2</sub> film. (Inset) Optical image showing monolayer MoS<sub>2</sub> (darker) grown between graphene stripes (lighter). Scale bar, 15 μm. (B) MoS<sub>2</sub> PL intensity mapping centered at 650 nm and (C) graphene G-band Raman mapping. Scale bars, 25 μm. (D) PL and Raman intensity profiles extracted along the dashed line as indicated in (B) and (C). PL spectrum for (E) MoS<sub>2</sub> and (F) WS<sub>2</sub>. (Inset) WS<sub>2</sub> PL intensity mapping. Scale bar, 50 μm.

Surprisingly, the graphene electrodes show a lower contact resistance despite drastic reduction in the electrode volume and, as we confirm below, the contact area.

This results in a higher 2-probe conductance, and therefore also an enhanced 2-probe field-effect mobility for the devices with 1DG contacts (Figure 5.6C, main panel). The improved contact resistance of the graphene electrodes implies that there is a strong connection between the graphene and TMD edges, suggesting a lack of a van der Waals gap or tunnel barrier as previously observed in 2DM contacts [164, 167] or overlapped graphene top contacts [40, 176]. We note that the 2-probe mobility obtained using 1DG contacts ranges from 10 to 30 cm<sup>2</sup>/Vs, consistent with our work discussed in Chapter 3.

The growth and fabrication process described above results in lateral TMD/graphene heterostructures with uniform properties over large areas. An optical micrograph of the heterostructure film over centimeter scales is shown in Figure 5.7A. We observe homogeneous graphene/MoS<sub>2</sub> heterostructures over the entire substrate with no visible overlap or multilayer regions in the optical contrast (see the zoomed-in image in the inset, Figure 5.7A). The monolayer homogeneity and spatial controllability are further confirmed by the MoS<sub>2</sub> photoluminescence (PL; Figure 5.7B) and graphene G-band Raman mapping (Figure 5.7C). The PL and Raman intensity profiles extracted along the dashed lines of Figure 5.7, B and C, show abrupt transitions within the optical resolution (approximately 1 μm) between the two materials (Figure 5.7D) demonstrating excellent compatibility with large area patterning with precise spatial control. The TMD layer show good optical properties as demonstrated by the sharp peaks in their PL spectra, similar to the ones obtained in exfoliated flakes (Figure 5.7, E and F) [3, 31].

### ***Confirmation of Lateral Connections: the Overall Monolayer Thickness***

Systematic studies further show that the nucleation behavior of the TMD is strongly dependent on the partial pressure ( $P_M$ ) of the transition metal precursor ( $\text{Mo}(\text{CO})_6$  for  $\text{MoS}_2$  and  $\text{W}(\text{CO})_6$  for  $\text{WS}_2$ ) during the growth. A scanning electron microscopy (SEM) image of a representative sample grown under optimized conditions, with  $P_M$  below 0.7 mTorr, is shown in Figure 5.8A (main panel) where we observe no  $\text{MoS}_2$  nucleation on graphene nor the formation of multilayer  $\text{MoS}_2$  regions in our TMD film. On the other hand, when the growth is performed under a more reactive environment (higher  $P_M$ ), we observe multilayer  $\text{MoS}_2$  regions on both the graphene and the  $\text{MoS}_2$  film (Figure 5.8A, inset). As shown below, the nucleation behavior of the TMD has a direct impact on the lateral stitching of the graphene and the TMD.

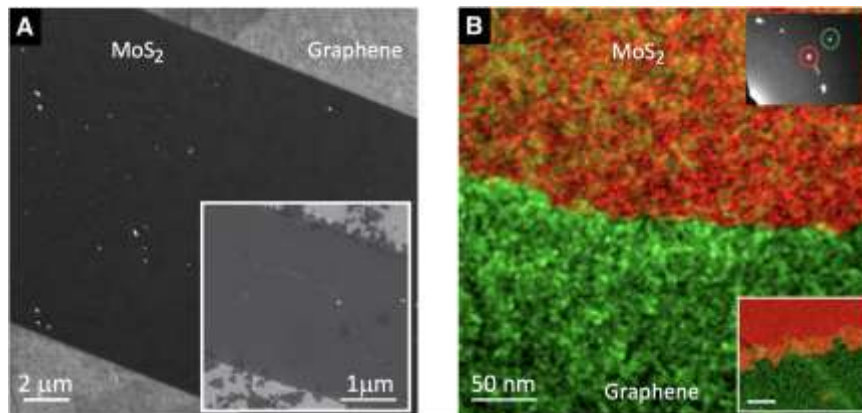


**Figure 5.8 Confirmation of lateral connection between graphene and TMD.**

(A) SEM image of a graphene/ $\text{MoS}_2$ /graphene lateral junction grown under a low Mo precursor pressure. (Inset) SEM image of a junction grown under high Mo precursor pressure. The presence of few-layer  $\text{MoS}_2$  flakes (dark triangles) on the graphene and on the monolayer  $\text{MoS}_2$  film indicate a more reactive growth environment. (B) A dark-field transmission electron microscopy (DF-TEM) image of the lateral junction formed between graphene and  $\text{MoS}_2$ , grown under a low Mo precursor pressure. (Upper inset) The diffraction spots used for the graphene area (green) and  $\text{MoS}_2$  (red). (Lower inset) A representative DF-TEM image of an overlapped junction obtained under non-optimal (high precursor pressure) growth conditions. Scale bar, 50 nm.

The lateral connection between the graphene and the TMD can be probed by dark-field electron microscopy (DF-TEM). Figure 5.8B shows a representative DF-TEM image of a graphene/MoS<sub>2</sub> junction grown under optimized conditions, showing no overlap region between the graphene and MoS<sub>2</sub> within the imaging resolution (below 10 nm). The selected diffraction spots are shown on the upper right inset. The lateral connection between graphene and MoS<sub>2</sub> is observed consistently over different regions of the substrate. A representative example of an overlapped graphene/MoS<sub>2</sub> junction, grown under high  $P_M$  (above 1 mTorr), is shown in the inset of Figure 5.8B. Its overlapped structure is similar to the ones that were recently reported [176], which displayed much higher contact resistance (approximately 300 k $\Omega$ · $\mu$ m) than our laterally-stitched 1DG contacts (see Figure 5.9C for a more quantitative comparison). The sharpness of our junctions is further confirmed by electron energy loss spectroscopy (EELS) analysis.

The formation of the lateral connection between graphene and MoS<sub>2</sub> (or WS<sub>2</sub>) only at low  $P_M$ , is consistent with the layer-by-layer growth mode as we discussed in Chapter 3 for our MOCVD growth of monolayer TMD. There, the nucleation and growth were limited to the SiO<sub>2</sub> growth surface until a fully continuous monolayer was formed. On the other hand, multilayer regions were found to form if the precursor concentration was higher. We similarly found that the TMD only nucleates on the SiO<sub>2</sub> surface including at the graphene edges at lower  $P_M$ , and the TMD grains grow on the SiO<sub>2</sub> surface until they meet and laterally connect to form a homogeneous layer. In contrast, with higher  $P_M$ , the TMD nucleates also on the graphene surface, leading to multilayer formation and regions of overlapped graphene/TMD junctions (see inset of Figure 5.8A). Our

results thus strongly suggest that the precise control of all the precursor pressures, which is a key feature of our MOCVD approach, is central to the fabrication of laterally connected edge-contacts between graphene and TMDs.

### 5.5 Low Contact Resistance of Graphene Electrodes

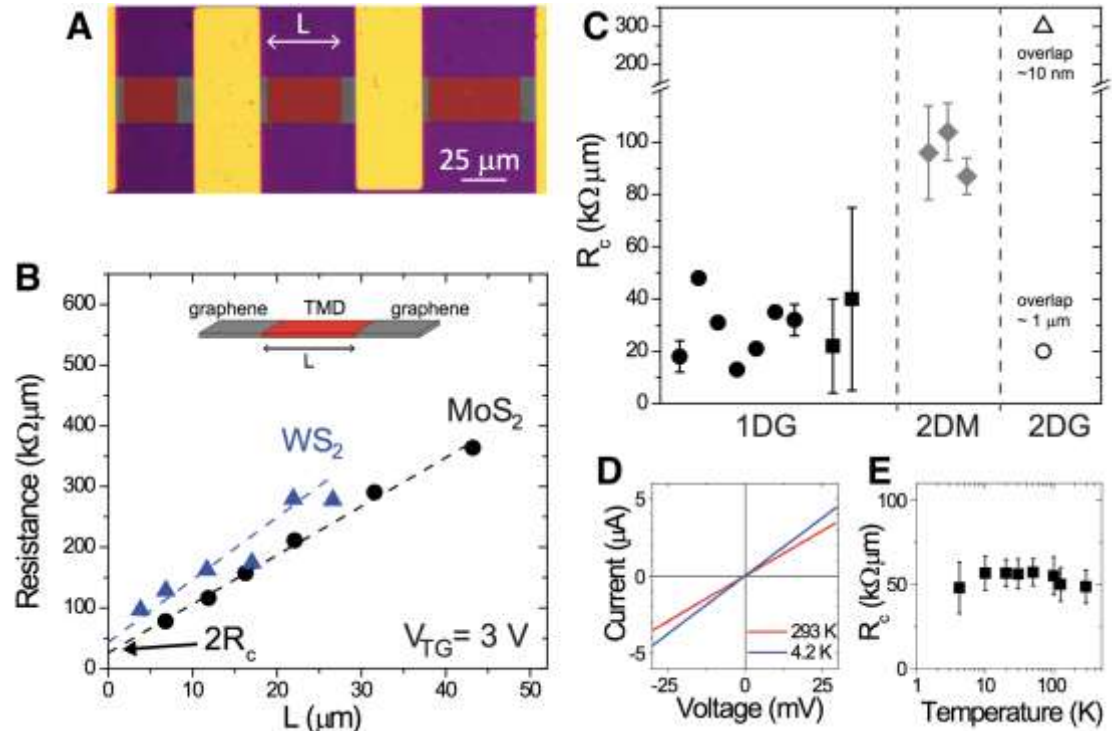


**Figure 5.9 High performance 1D edge contact of graphene electrodes.**

(A) Optical micrograph of the device geometry used in the transfer length measurements, where  $L$  is the MoS<sub>2</sub> channel length. (B) 2-probe resistance as a function of  $L$  for MoS<sub>2</sub> (black circles) and WS<sub>2</sub> (blue triangles) with 1DG contacts. The y-intercept of the linear fits gives  $2R_c$  and the slope gives the sheet resistance. (C)  $R_c$  values for different devices at high carrier density. The solid circles (solid squares) represent our MoS<sub>2</sub> (WS<sub>2</sub>) based devices with 1DG contacts. The gray diamonds represent  $R_c$  for our 2DM contacts to MoS<sub>2</sub>. Devices with 2DG contacts from references [176] and [40] are denoted by the open triangle and open circle, respectively. (D) Source-drain current *versus* voltage at 293 K (red) and 4.2 K (blue) for a MoS<sub>2</sub> based device with 1DG contacts at  $V_{\text{TG}} = 3 \text{ V}$  ( $n \sim 1 \times 10^{13} \text{ cm}^{-2}$ ). (E)  $R_c$  as a function of temperature for the same device in (D).

We performed quantitative determinations of contact resistances using the analog of transfer length measurements (TLMs) [167, 169, 179], based on the 2-probe resistance of TMD channels measured with varying length and fixed width (see Figure 5.9A for an optical image of a device). The total 2-probe resistance is  $R = 2R_c + \left(\frac{\rho_{TMD}}{W}\right)L$ , where  $\rho_{TMD}$  is the TMD resistivity, and  $W$  and  $L$  are the TMD channel width and length respectively. In this analysis we ignore the contact resistance between graphene and the metal contact. However, we note that this contribution can become relevant if the contact area between the metal electrode and graphene is reduced. Figure 5.9B shows the measured dependence of  $R$  on  $L$  for two devices with 1DG contacts to MoS<sub>2</sub> (black circles) and WS<sub>2</sub> (blue triangles) channels. These measurements were taken at a top gate voltage of  $V_{TG} = 3$  V, corresponding to a carrier density of  $n \sim 1 \times 10^{13}$  cm<sup>-2</sup>, estimated from the threshold voltage and the gate capacitance. The  $R_c$  values are obtained by extrapolating to zero TMD length, which are similarly low for the 1DG contacts to both MoS<sub>2</sub> and WS<sub>2</sub>, on the order of 20 k $\Omega \cdot \mu\text{m}$ . This suggests that our method is versatile towards its use with different TMDs.

The one-dimensional graphene edge contacts show consistently low contact resistances with good reproducibility. In Figure 5.9C we plot our results for  $R_c$  obtained by TLM measurements for seven MoS<sub>2</sub> (solid circles) and two WS<sub>2</sub> based devices (solid squares) with 1DG contacts, obtained from five different growth runs on different substrates. The values for  $R_c$ , measured at a carrier density of  $n \sim 1 \times 10^{13}$  cm<sup>-2</sup>, remain similar throughout different samples, with the median  $R_c$  of 30 k $\Omega \cdot \mu\text{m}$ . For a direct comparison, we fabricated three MoS<sub>2</sub> based devices using Ti/Au metal electrodes, which are widely used to contact TMD materials, next to some of the devices with 1DG

contacts. These devices with 2DM contacts show higher contact resistance values ( $R_c \sim 95 \text{ k}\Omega \cdot \mu\text{m}$ ; denoted by solid diamonds, Figure 5.9C) at similar carrier densities that are consistent with previously reported results [37]. These results confirm that our graphene electrodes provide low resistance edge contacts to TMDs despite the minimal electrode volume with  $R_c$  values that are smaller than those of conventional Ti/Au 2DM contacts but are larger than the smallest values recently reported from pure metal electrodes [170, 182]. Here we restrict our comparison to contacts to monolayer TMDs only, since  $R_c$  is known to increase with the decrease in layer number [164, 172, 183, 184].

Figure 5.9C presents additional comparison with graphene top (2DG) contacts, which have achieved similarly low contact resistances in the order of  $R_c \sim 20 \text{ k}\Omega \cdot \mu\text{m}$  while reducing significantly the electrode volume when compared to 2DM contacts (open circle in Figure 5.9C) [40, 173]. However, when the overlap area between the graphene top contact and MoS<sub>2</sub> is reduced, the devices show an increase in contact resistance ( $R_c \sim 300 \text{ k}\Omega \cdot \mu\text{m}$ ; open triangle in Figure 5.9C) and display nonlinear  $I$ - $V$  characteristics at room temperature [176], showing that 2DG contacts may not be suitable for small scale devices. Likewise,  $R_c$  in devices with 2DM contacts is known to increase exponentially when the contact length is decreased below the transfer length ( $L_T \sim 15 - 600 \text{ nm}$ ) [167, 169, 184], which limits the minimum device footprint. On the other hand, our 1DG contacts should not be bound by such limitations, since it uses the edge contact geometry. Furthermore, temperature dependent electrical measurements confirm the ohmic nature of the graphene edge contacts to MoS<sub>2</sub>: our MoS<sub>2</sub> devices with 1DG contacts show linear IV characteristics with little temperature dependence from room temperature down to liquid helium temperatures (Figure 5.9D), and we observe

no temperature dependence for  $R_c$ , extracted from TLM, over the same temperature range (Figure 5.9E). Altogether, these results suggest that 1DG contacts provide an excellent route for reducing the overall device size while maintaining low-resistance ohmic contacts.

## 5.6 Summary

In this chapter we presented our work on producing truly monolayer devices, including WS<sub>2</sub>-WSe<sub>2</sub> and graphene-MoS<sub>2</sub> lateral heterostructures, as examples for semiconductor-semiconductor and metal-semiconductor lateral heterostructures. These heterostructures were synthesized using the technique we discussed earlier in Chapter 3 and 4. First, three kinds of new devices fabricated based on our coherent WS<sub>2</sub>-WSe<sub>2</sub> heterostructures—p-n diodes (both with and without encapsulation), LEDs, and double heterostructure transistors—all show high performance, which is consistent with the high quality of the coherent heterointerfaces as discussed in Chapter 4. Second, we showed that graphene can be laterally connected to TMD in the monolayer plane, acting as an excellent 2D metallic electrode while maintaining the monolayer thickness. Our demonstration of high-performance TMD-TMD and graphene-TMD heterostructures provides a versatile method for integration of materials in the monolayer limit, and such scalable method can be used for producing atomically-thin circuitry.

## CHAPTER 6

### HYBRID THIN FILMS WITH VERTICALLY PROGRAMMED COMPOSITION

#### 6.1 Introduction

Up to this point, we have been focusing on producing large-scale films as well as high-quality heterostructures of TMDs in the monolayer limit. These monolayers provide 2D building blocks that can be integrated with themselves as well as other materials, to create hybrid thin films with vertically controlled composition (Figure 6.1). Such hybrid thin films provide the foundation for modern integrated circuitry and novel materials discovery<sup>1-3</sup>.

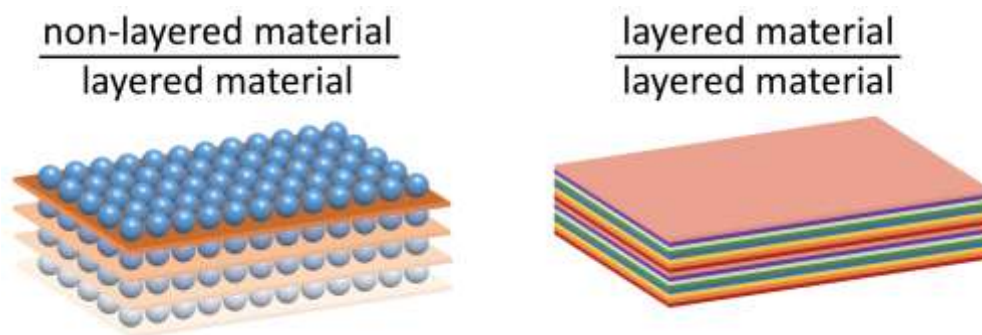


**Figure 6.1 Monolayer TMDs as building blocks for 3D structures.**

(Left) Vertical structures of monolayer TMDs (thin sheets) and non-layered materials (spheres). (Right) Vertical structures of 2D layered materials including monolayer, in which colors represent different 2D building blocks.

In this chapter, which is largely adapted from Ref. 98 and Ref. 186, we will first present an example of hybrid thin films via direct growth, where vertical  $\text{SiO}_2/\text{MoS}_2$  thin films are generated by alternating the growth of  $\text{SiO}_2$  and  $\text{MoS}_2$  (adapted from Ref. 98). We further demonstrate our approach for integrating different TMDs in the vertical direction to form van der Waals (vdW) heterostructures (adapted from Ref. 186). While the vdW heterostructures where monolayer TMDs are stacked on top of one another

[101, 186, 187] presents a powerful approach to produce atomically thin films with novel properties [177, 188–191], the challenges related to generating such films with pristine interfaces on the large scale limits this approach to small-scale proof-of-concept demonstrations. We report the generation of wafer-scale high-quality semiconductor films whose vertical composition and properties are directly designed on the atomic scale using layer-by-layer assembly of monolayer TMDs with excellent spatial uniformity and pristine interfaces.

## ***6.2 Hybrid Films of MoS<sub>2</sub>/SiO<sub>2</sub> with Vertical Composition Control***

With the data presented in Chapter 3, we confirmed the structural and electrical uniformity of the wafer-scale ML MoS<sub>2</sub> film grown by our MOCVD method. This makes our film compatible with the batch device fabrication processes on a technologically relevant scale. Moreover, as SiO<sub>2</sub> provides a substrate for its growth, one can produce high quality ML films on a variety of substrates by depositing SiO<sub>2</sub> prior to the growth. This versatility would allow the realization of high performance FETs directly on non-conventional substrates, such as metal and thermally stable plastic. In addition, one can integrate multiple layers of MoS<sub>2</sub> devices by repeating the TMD film growth, device fabrication, and SiO<sub>2</sub> deposition, which could enable novel three-dimensional circuitry.

In Figure 6.2, we demonstrate this unique potential by producing multi-stacked ML MoS<sub>2</sub> films as well as electronic devices fabricated at different vertical levels. Figure 6.2A shows the schematics and photos of three substrates each with single, double or triple ML MoS<sub>2</sub> films grown at different levels. The first (bottom) ML film was grown

on a fused silica substrate while the additional layers were grown on SiO<sub>2</sub> (100 nm thick) deposited on the previously grown MoS<sub>2</sub> ML using plasma-enhanced CVD (PECVD). The color of the substrate, which remains uniform for each substrate, becomes darker as the number of layers increases. Their absorption spectra, shown in Figure 6.2B, present almost identical absorption at all measured wavelengths, once normalized by the number of stacks grown (see inset), suggesting little degradation of the optical properties of the ML MoS<sub>2</sub> films after subsequent oxide deposition and MoS<sub>2</sub> growth.

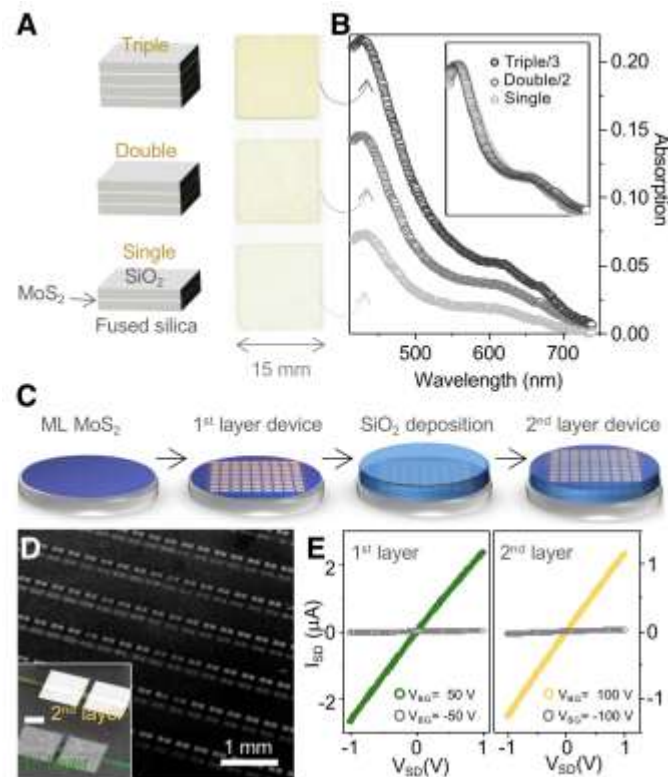


**Figure 6.2 Hybrid thin film of SiO<sub>2</sub>/MoS<sub>2</sub> vertical heterostructures.**

(A) Schematics (left) and optical image (right) of single, double and triple stacking of ML-MoS<sub>2</sub>/SiO<sub>2</sub>. (B) Optical absorption spectra for single, double and triple stacks, respectively (normalized spectra shown in the inset). (C) Schematic for fabrication of MoS<sub>2</sub> device/SiO<sub>2</sub> stacking using alternating MOCVD growth, device fabrication with photolithography, and SiO<sub>2</sub> deposition. See main text for details. (D) False-color SEM image of MoS<sub>2</sub> FET arrays on 1<sup>st</sup> (bottom) and 2<sup>nd</sup> (top) layer (zoomed-in image of a pair of devices shown in the inset, scale bar 50 μm). (E) I<sub>SD</sub>-V<sub>SD</sub> curves measured from two neighboring devices on 1<sup>st</sup> and 2<sup>nd</sup> layer, respectively, both showing the n-type conductance switching.

Figure 6.2C shows the schematics of our multi-stacked device fabrication process: (i) first ML MoS<sub>2</sub> growth on a SiO<sub>2</sub>/Si wafer, (ii) FET fabrication, (iii) deposition of SiO<sub>2</sub> (thickness of 500nm), (iv) second ML MoS<sub>2</sub> growth and FET fabrication. A false-color SEM image in Figure 6.2D shows an array of MoS<sub>2</sub> FETs successfully fabricated using this process. It includes functioning MoS<sub>2</sub> FETs located at two different vertical levels, the conductance of which can be simultaneously modulated with a global back gate. The I<sub>SD</sub>-V<sub>SD</sub> curves measured from two adjacent FETs located next to each other, both laterally and vertically (see inset, Figure 6.2D), are shown in Figure 6.2E. Both devices show V<sub>BG</sub> dependent conductance change (notice the smaller change for the 2<sup>nd</sup> layer) with an on-state  $\sigma_{\square}$  of 2.5  $\mu\text{S}$  (1<sup>st</sup> layer) and 1.5  $\mu\text{S}$  (2<sup>nd</sup> layer), respectively. Furthermore, we measured similar  $\mu_{\text{FE}}$  values (11.5 cm<sup>2</sup>/Vs and 8.8 cm<sup>2</sup>/Vs) from the two devices. We note that the two ML MoS<sub>2</sub> films were grown on SiO<sub>2</sub> substrates prepared differently and that the 1<sup>st</sup> layer device has gone through additional steps, including the second MoS<sub>2</sub> growth. Our data in Figure 6.2 thus confirm the compatibility of our MOCVD-grown MoS<sub>2</sub> films with conventional thin film deposition and multi-stacking, which could be used to develop a three-dimensional device architecture based on TMD.

### ***6.3 Layer-by-Layer Assembly of TMDs into Wafer-Scale Vertical***

#### ***Heterostructures***

In this section, we present the production of wafer-scale high-quality vdW heterostructured films by layer-by-layer assembly of monolayer TMDs with excellent spatial uniformity and pristine interfaces. For this, we use the method of programmed

vacuum stacking, where a series of wafer-scale, three-atom-thick semiconductors ( $\text{MoS}_2$ ,  $\text{MoSe}_2$ , and  $\text{WS}_2$ ) are stacked under vacuum. Using our approach, we fabricate a variety of large-scale high-quality heterostructure films and devices that are previously inaccessible. These include superlattice films having composition vertically-designed layer-by-layer, batch-fabricated tunnel device arrays with their resistance tuned over four orders of magnitude, band-engineered heterostructure tunnel diodes, and millimeter-scale ultrathin membranes. In addition, these stacked films are highly detachable and compatible with water or plastic surface, which will enable their integration with advanced optical and mechanical systems and applications in unconventional environments. Furthermore, our approach could be compatible with other organic, inorganic, and emerging 2D materials, a prospect that may lead to an entirely new set of high-quality hybrid materials and multifunctional integrated circuits.

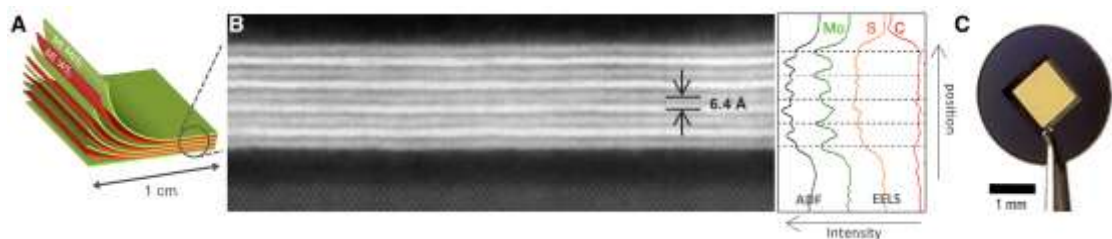


**Figure 6.3 High-quality vertically-designed films using layer-by-layer assembly of monolayer TMDs.**

(A) Schematic diagram of a vertically stacked  $\text{MoS}_2/\text{WS}_2$  superlattice. (B) (Left) A cross-sectional ADF-STEM image of a superlattice film transferred on a  $\text{SiO}_2/\text{Si}$  substrate. The bright and dark layers are  $\text{WS}_2$  and  $\text{MoS}_2$  MLs, respectively, with the Si crystal lattice shown at the bottom. (Right) Intensity profiles measured from the ADF-STEM image and the EELS mapping along the out-of-plane direction. Black, ADF STEM; green, EELS for Mo; orange, EELS for S; red, EELS for C. (C) Photo of a large-scale freestanding ultrathin semiconductor film (7-layer  $\text{MoS}_2$ ; thickness  $\sim 4.5$  nm). The film is fully suspended over a  $1 \times 1 \text{ mm}^2$  hole on a TEM chip.

Figure 6.3A-B shows a representative high-quality semiconductor heterostructure film generated using the programmed vacuum stack (PVS) process (explained in Figure

6.4). The film is assembled by vertically stacking nine layers of individual wafer-scale ML TMD films alternating between MoS<sub>2</sub> and WS<sub>2</sub> (see schematic in Figure 6.3A). The scanning transmission electron microscopy (STEM) data in Figure 6.3B confirm that its composition is vertically designed with atomic-scale precision and clean interfaces. First, five dark layers and four bright layers are clearly visible in the cross-sectional annular dark field (ADF)-STEM image of the film (Figure 6.3B left panel), which correspond to the five MLs of MoS<sub>2</sub> and four MLs of WS<sub>2</sub>, respectively. The chemical composition of each layer is directly confirmed by electron energy loss spectroscopy (EELS; Figure 6.3B right panel), which shows the Mo peaks only for the MoS<sub>2</sub> layers, but a uniform S signal everywhere within the film. Second, all nine individual layers appear uniform and continuous, and run straight and parallel to each other. The interfaces between adjacent layers remain clean and free of bubbles or wrinkles, with a constant interlayer distance of 0.64 nm, which is consistent with the value expected for MoS<sub>2</sub>/WS<sub>2</sub> with a non-zero interlayer rotation angle [192]. Third, the EELS data further shows a very low signal for carbon (red curve, Figure 6.3B) within the film near the detection limit of our instrument. Figure 6.3C presents another high-quality large-scale semiconductor film assembled with seven layers of MoS<sub>2</sub>, which is completely separated from the substrate and suspended over a 1 × 1 mm<sup>2</sup> square hole in the middle of a TEM chip. The freestanding film is thinner than 5 nm, with one of the highest aspect ratio (length/thickness ~ 0.2 million) ever reported for freestanding semiconductor films [193–195], indicating that our film has excellent structural quality and mechanical strength. Altogether, the data in Figure 6.3 demonstrate that we have successfully

produced high-quality, detachable films with atomic-scale programmability and pristine interfaces.

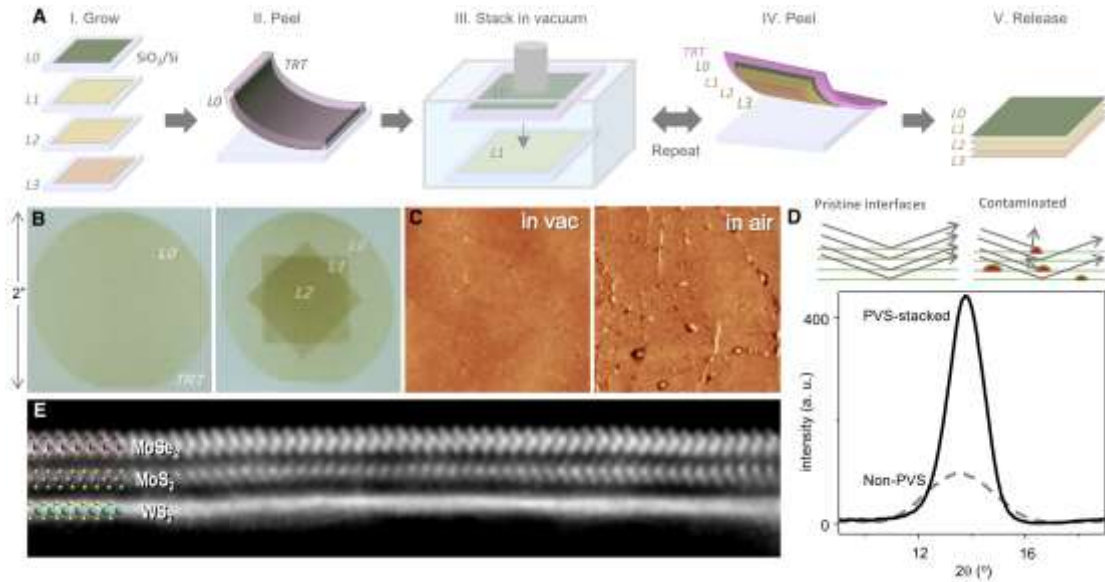


**Figure 6.4 Programmed vacuum stack (PVS) process.**

(A) A schematic of the PVS process; see main text for a detailed description. (B) Images of wafer-scale MoS<sub>2</sub> films after step (II) (left), where the first layer (L0) on TRT is peeled from a 2" wafer, and after step (IV) (right), where two more layers (L1 and L2; 1"-wide squares) are stacked on L0, forming a 3L-MoS<sub>2</sub> film. (C) AFM height images (2 μm × 2 μm) taken from the bottom (L2) side of 3L-MoS<sub>2</sub> films stacked in vacuum (left) and air (right). The film stacked in vacuum has a flatter surface without bubble-like structures. Height scales, ±5 nm. (D) XRD pattern of four-layer MoS<sub>2</sub> generated by the PVS process (solid curve) and by conventional dry transfer (dashed curve). The single peak at  $2\theta \approx 14^\circ$  originates from X-ray beams diffracted by monolayers spaced along the c-axis direction. Inset, schematics of the X-ray diffraction from stacked films with pristine interfaces (left) and contaminated interfaces (right). The effective beam area used for the measurement is an ellipse of 0.5 cm × 1 cm. (E) Cross-sectional STEM image of a MoSe<sub>2</sub>/MoS<sub>2</sub>/WS<sub>2</sub> film with the electron beam aligned with the armchair axis of MoSe<sub>2</sub> (top) and MoS<sub>2</sub> (middle).

Figure 6.4A schematically illustrates the PVS process: (I) wafer-scale building blocks (TMD MLs) are synthesized individually by MOCVD. (II) the initial layer L0, spin-coated with an adhesive polymer film, is mechanically peeled from the growth substrate (SiO<sub>2</sub>/Si) using a thermal release tape (TRT). (III) L0/TRT is then stacked and pressed on top of the next layer L1 (on the growth substrate) in a vacuum chamber,

forming an air-free interface between L0 and L1. (IV) L1/L0/TRT is peeled off from the substrate. The vacuum stack (III) and peel (IV) steps are repeated to directly program the vertical composition of the film with the desired number of layer ( $N_L$ ). (V) the  $N_L$ -layer film is then released from the TRT onto a target substrate, in either supported or suspended form.

The PVS process was designed to provide two key advantages over existing methods: the wafer-scale fabrication and the generation of pristine interlayer interfaces. For the former, MOCVD processes are used to grow homogeneous wafer-scale semiconductor monolayers as the building blocks ( $\text{MoS}_2$ ,  $\text{MoSe}_2$ , and  $\text{WS}_2$ ). For the latter, we optimize the synthesis to generate excellent surface properties, allowing these building blocks to be cleanly peeled off from the growth substrates without the use of any etchants or solvents. These building blocks are then assembled under vacuum using a customized apparatus for wafer-scale vacuum-stacking. As we show below, this vacuum stacking greatly improves the interface quality and flatness of the films, minimizing the amount of amorphous carbon or trapped air at the interfaces. Moreover, the PVS process can be used with an arbitrary building blocks as long as the adhesion to the stacked film is stronger than that to the growth substrate, making this a general approach for producing large-scale, vertically-designed stacked films with pristine interfaces.

These key advantages are realized in our films as confirmed by the following experiments. Here, we use multiple characterization techniques in combination, each of which covers a different and overlapping length scale from sub-nanometer up to centimeter scale, spanning over eight orders of magnitude in the characterizing length

scale. First, we confirm that our stacked films are spatially uniform on the wafer scale. Figure 6.4B displays photos of a three-layer MoS<sub>2</sub> film taken during the process. The figure shows a 2"-diameter circular region of L0 after the initial peeling (left image), and a three-layer MoS<sub>2</sub> film (right image) after two 1"-wide squares of MoS<sub>2</sub> MLs, L1 and L2, are subsequently stacked. All layers remain continuous and uniform in these photos. Additional Raman mapping (Figure 6.5, A-C) and optical absorption spectra (Figure 6.5D) up to ten layers further confirm the spatial uniformity from sub-micrometer up to centimeter scale and the consistent layer dependent characteristics of our stacked films.

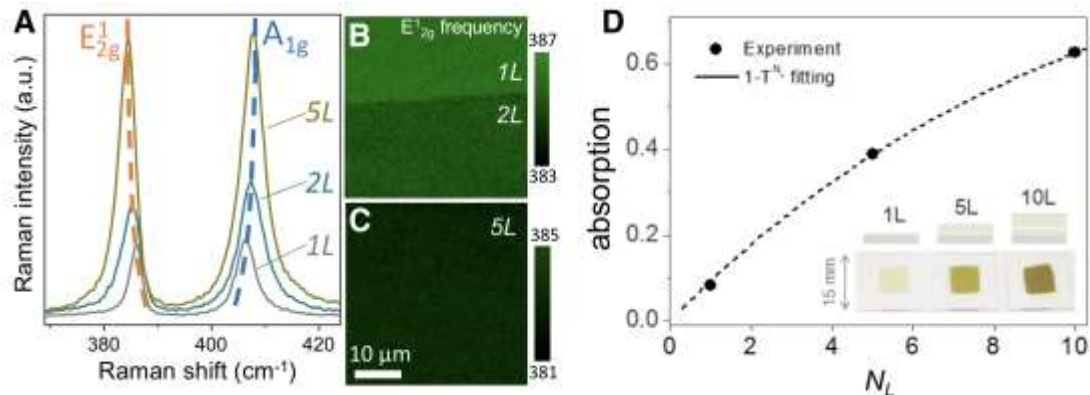


**Figure 6.5 Uniform Raman and optical absorption of PVS-stacked MoS<sub>2</sub> films.** (A) Raman spectra taken from 1L-, 2L- and 5L-MoS<sub>2</sub>. Dashed lines track the trajectory of peak frequency as a function of  $N_L$ . (B) Raman frequency mapping of E<sub>12g</sub> peak across 1L- and 2L-MoS<sub>2</sub> films. (C) Raman frequency mapping of E<sub>12g</sub> peak at 5L-MoS<sub>2</sub>. (D) Absorption measured at 532 nm as a function of  $N_L$  with a spot size of 1 cm. The trend follows the expected layer dependent absorption  $1 - T^{N_L}$  with  $T = 0.91$ , close to the value for ML MoS<sub>2</sub>. Inset: Schematics and photos of the measured films,  $N_L=1, 5, 10$ .

Second, the films generated using the PVS process show greatly improved interlayer structures and flatness. In Figure 6.4D we present thin-film X-ray diffraction (XRD) data measured from a PVS-stacked 4L-MoS<sub>2</sub> film (solid curve) over an area of 0.5 by 1 cm<sup>2</sup>. These data show a peak at  $2\theta \approx 14^\circ$ , where  $\theta$  is the angle of incident X-

rays to the sample plane, corresponding to the monolayer spacing along the c-axis direction, the intensity of which is five times higher than that observed from the other film, which was generated by a non-PVS process (dashed curve; conventional dry-transfer [191]). In addition, the peak position can be converted to an average interlayer spacing of 0.64 nm, close to the expected value of 0.65 nm calculated for twisted MoS<sub>2</sub> multilayers [192]. The above results indicate that the PVS process indeed improves the coherence of interlayer structure over centimeter scale, suggesting cleaner interfaces with reduced amount of interlayer contaminations in the films. Furthermore, Figure 6.4C shows the atomic force microscopy (AFM) images (measured on the bottom side of L2) of two MoS<sub>2</sub> films ( $N_L = 3$ ), preparation steps of which are identical except for the stacking environment: one is stacked in vacuum (left), and the other in air (right). The film stacked in vacuum (roughness  $\sim 270$  pm) is much smoother than the one stacked in air (roughness  $\sim 700$  pm). In addition, the vacuum-stacked film is free of bubble-like features, which are clearly visible in the film stacked in air and are similar to the features reported previously [196, 197].

Finally, our stacked films can be generated using various monolayer TMDs without the constraints of the lattice match or alignment. Figure 6.4E shows a cross sectional STEM image of a MoSe<sub>2</sub>/MoS<sub>2</sub>/WS<sub>2</sub> film, where the zig-zag axes of the MoSe<sub>2</sub> (top) and MoS<sub>2</sub> (middle) layers are parallel to the electron beam, while that of WS<sub>2</sub> is not. This image shows that the vertical stacking is successful in the presence of a lattice mismatch (e.g. MoSe<sub>2</sub> lattice constant is larger than MoS<sub>2</sub> by  $\sim 4.2\%$ ) [198], or an interlayer rotation (between MoS<sub>2</sub> and WS<sub>2</sub>).

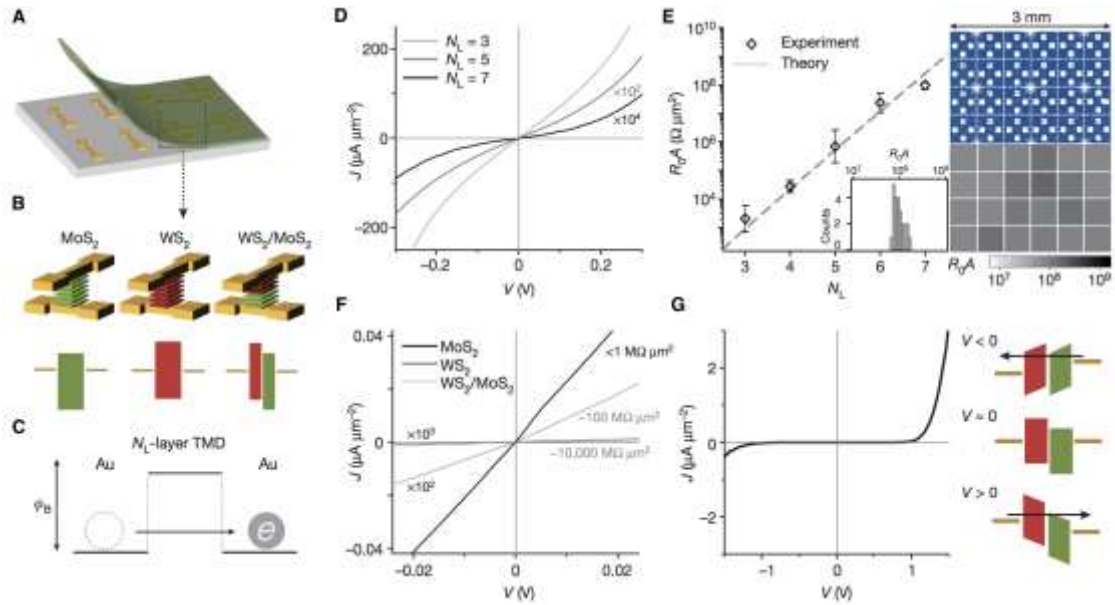


**Figure 6.6 Tuning electrical conductance of stacked semiconductor films using the number of layers or vertical composition.**

(A) Schematic of our device geometry in which a stacked film is sandwiched between top and bottom electrodes. (B) Schematic of devices with different film compositions (top) and their corresponding band profiles (bottom). (C) Schematic of the general band profile of our tunnel devices in the zero-bias regime.  $\phi_B$  is the barrier height, and  $e$  is the electron that tunnels through the barrier. (D)  $J$ - $V$  characteristics measured from three Au/ $N_L$ -layer MoS<sub>2</sub>/Au devices with  $N_L=3, 5$  and  $7$ . The curves for  $N_L=5$  are multiplied by  $10^2$  and for  $N_L=7$  by  $10^4$ . (E) Zero-bias tunnel resistance–area product measured as a function of  $N_L$  (left). Each data point is an average from ten devices; the error bars show the standard deviation. The dashed line is calculated using a tunnel model with a single fitting parameter,  $\phi_B=0.5$  eV. An optical image of an array of 24 tunnel devices made with seven-layer MoS<sub>2</sub> over an area of  $2\text{ mm} \times 3\text{ mm}$  is shown top right. A spatial map of the tunnel resistance of the 24 devices is shown at bottom right; the corresponding histogram is shown in the inset of the left panel. (F)  $J$ - $V$  curves near zero bias measured from MoS<sub>2</sub>, WS<sub>2</sub> and WS<sub>2</sub>/MoS<sub>2</sub> devices, all with  $N_L=6$ . The curves for WS<sub>2</sub>/MoS<sub>2</sub> and WS<sub>2</sub> are multiplied by  $10^2$  and  $10^3$ , respectively. The corresponding tunnel resistance is shown for each  $J$ - $V$  curve. (G) (Left)  $J$ - $V$  curve of the heterostructure WS<sub>2</sub>/MoS<sub>2</sub> device in the large bias regime, where the WS<sub>2</sub> side is grounded, showing diode behavior with the forward bias current about 10 times larger than the reverse bias current at 1.4 V. (Right) the corresponding band diagrams under large reverse bias ( $V < 0$ ), zero-bias ( $V \sim 0$ ), and large forward bias ( $V > 0$ ), which have different effective electron tunnel length. Arrows indicate the direction of electron tunneling.

## ***6.4 Tuning Electrical Conductance of Stacked Semiconductor Films by Vertical Composition Control***

Our PVS process allows for the generation of a large number of distinct, vertically-designed semiconductor films with only a small set of 2D building blocks. For example, with  $n$  kinds of 2D building blocks, one can construct  $n^L$  distinct films by stacking  $L$  layers. Here, the  $n$  different building blocks can be individually grown without considering the specific stacking sequence, making the programming process simple and straightforward. Moreover, these stacked films would enable batch-fabrication of electronic and optoelectronic devices as the PVS process generates homogenous structures and properties over large areas.

In Figure 6.6, we demonstrate these by generating a series of distinct stacked films and heterostructures that have a larger number of stacked interfaces, all assembled with two representative TMD MLs ( $\text{MoS}_2$  and  $\text{WS}_2$ ). To study their electrical properties, we fabricate large arrays of metal/stacked film/metal vertical tunnel devices as shown in Figure 6.6, A and B. Here, we choose gold as the electrode metal, forming a tunnel band diagram as schematically illustrated in Figure 6.6C. Using the tunnel device geometry, we can investigate the uniformity and high quality of PVS-stacked films accurately over large area, because tunneling is exponentially sensitive to the barrier properties including the thickness, band structure, doping, and defects.

Figure 6.6D shows the representative current density versus bias ( $J$ - $V$ ) curves measured from  $N_L$ -layer  $\text{MoS}_2$  films ( $N_L = 3, 5, 7$ ). All three  $J$ - $V$  curves show similar non-Ohmic behavior, with the current increasing superlinearly with an increasing bias. In addition, the magnitude of  $J$  strongly depends on  $N_L$ , decreasing approximately by

ten-fold with each additional layer. Figure 6.6E (left) further plots the average zero-bias resistance-area product ( $R_0A$ ; average from ten devices) as a function of  $N_L$ , which confirms the same exponential  $N_L$  dependence. This exponential dependence and the superlinear  $J$ - $V$  curves strongly suggest that the main transport mechanism in our devices is electron tunneling as schematically shown in Figure 6.6C, which is the same mechanism observed from similar devices made with exfoliated hexagonal boron nitride flakes [199]. Furthermore, our experimental data quantitatively match the theoretical zero-bias resistance, which is calculated based on a tunnel model [200] using the barrier height  $\phi_B$  as the single fitting parameter (Figure 6.6E dash line, plotted with  $\phi_B = 0.5$  eV).

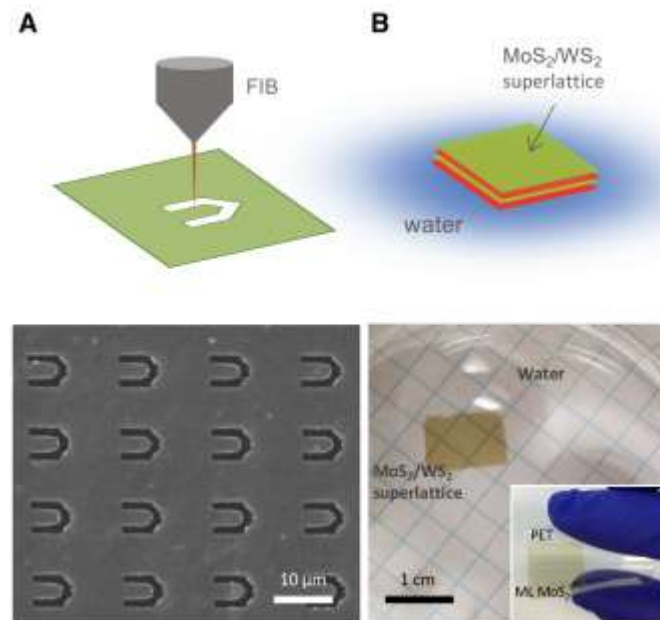


**Figure 6.7 TMD films at different interfaces.**

(A) (Bottom) SEM image of cantilever-shaped structures generated within a 7L-MoS<sub>2</sub> membrane. These structures are made using focused-ion beam milling (top schematic). (B) A 4L-MoS<sub>2</sub>/WS<sub>2</sub> superlattice floating on water with no additional support (schematic at the top). (Inset) Image of a 1''-wide monolayer MoS<sub>2</sub> film transferred onto a plastic (PET) substrate from water.

The agreement between our experimental data and the theoretical model indicates that our MoS<sub>2</sub> films have a well-controlled  $N_L$  and band energy (i.e. doping level) uniform across the entire films without structural inhomogeneities (such as cracks, wrinkles or trapped impurities) that would strongly affect the tunnel current. This is further supported by the spatial map of  $R_0A$  values measured from an array of twenty four 7L-MoS<sub>2</sub> tunnel devices over an area of  $2 \times 3 \text{ mm}^2$  (Figure 6.6E, right panel). This map shows a 100% device yield with a uniform tunnel resistance. The tunnel resistance histogram of these measurements (Figure 6.6E, inset) further shows a single narrow peak with a standard deviation that corresponds to a thickness variation of only 0.1 layers (about 70 pm).

The electrical properties of our stacked films are also composition-sensitive. As schematically depicted in Figure 6.6B for three example devices of 6L-MoS<sub>2</sub>, 6L-WS<sub>2</sub> and 3L-WS<sub>2</sub>/3L-MoS<sub>2</sub>, varying the composition drastically modified the tunnel band profiles of the devices. Figure 6.6F presents the  $J$ - $V$  curves of these devices near zero bias, showing up to  $\sim 10,000$ -fold increase in resistance when the composition of the film is changed from MoS<sub>2</sub> ( $< 1 \text{ M}\Omega \cdot \mu\text{m}^2$ ) to WS<sub>2</sub> (about  $10 \text{ G}\Omega \cdot \mu\text{m}^2$ ). In addition, an intermediate value of about  $100 \text{ M}\Omega \cdot \mu\text{m}^2$  is observed from the WS<sub>2</sub>/MoS<sub>2</sub> heterostructure device. The different band alignments of MoS<sub>2</sub> versus WS<sub>2</sub> (Figure 6.6B, bottom) explains this large tuning range. Even though MoS<sub>2</sub> and WS<sub>2</sub> have similar bandgap energies, the Fermi level of gold is closer to the center of the WS<sub>2</sub> bandgap [201], leading to a higher tunnel barrier and thus larger resistance for the WS<sub>2</sub> device. Similarly, the effective barrier height in the heterostructure WS<sub>2</sub>/MoS<sub>2</sub> device is approximately the average of those of MoS<sub>2</sub> and WS<sub>2</sub>, explaining the intermediate

tunnel resistance value [200]. Moreover, the heterostructure WS<sub>2</sub>/MoS<sub>2</sub> device shows an asymmetric, diode-like  $J$ - $V$  curve at larger biases (Figure 6.6G), with the forward bias current  $\sim 10$  times larger than reverse bias current at 1.4 V, in contrast to the symmetric curves of MoS<sub>2</sub> and WS<sub>2</sub> devices. This behavior is similar to the characteristic behavior of the metal-insulator-insulator-metal tunnel diode reported recently [202], whereby the effective tunnel distance changes depending on the bias direction owing to the barrier height offset at the insulator-insulator interface. (Figure 6.6G, right).

### **6.5 TMD Films at Various Interfaces**

The above results confirm that our PVS process enables the production of large-scale high-quality semiconductor films with precisely designed vertical compositions and electrical and optical properties. Moreover, these PVS-stacked films are highly detachable, transferable, and compatible with various environments and processing. For instance, the films can be patterned to generate freestanding structures, or transferred to form unconventional interfaces, as we demonstrate below.

Figure 6.7A first demonstrates the fabrication of freestanding structures of an array of cantilever-shaped structures, patterned using a focused ion beam milling (SEM image shown at bottom), within a 7L-MoS<sub>2</sub> film ( $1 \times 1 \text{ mm}^2$ , shown in Figure 6.3C). This process allows us to pattern ultrathin semiconductor structures with an arbitrary shape, such as cantilevers or holes, which could lead to a new class of micro- and nano-electromechanical systems [203] and nanoporous membranes [204]. Finally, Figure 6.7B shows a large-scale 4L-Mo/W/Mo/WS<sub>2</sub> superlattice film floating on water surface,

generating a semiconductor/water interface. The film is delaminated from a substrate by simply dipping it into water [205] with no polymer support, which provides another way of releasing the stacked films onto surfaces with different thermal/chemical nature, such as plastic substrates (inset photo).

## **6.6 Summary**

In this chapter we presented our work on production of two types of hybrid films—TMD/non-layered material and TMD/TMD vertical heterostructures. In the first case, we demonstrate vertical MoS<sub>2</sub>/SiO<sub>2</sub> films via direct, sequential growth approach. In the second case, we produce large-scale vertical TMD films using a growth-and-stack approach. These demonstrations represent a powerful platform for systematically generating previously unavailable large-scale heterostructures and devices whose properties are designed with atomic scale precision. For example, its application to emerging layered materials, including monolayer superconductors [206] and ferromagnets [10, 11], would produce novel interfaces and superlattices where superconductivity and magnetic orders coexist, with the coupling between them being tuned layer-by-layer. Furthermore, hybrid materials and devices, where non-layered materials, such as organic films and self-assembled nanostructures, are stacked vertically, layer-by-layer, along with the 2D layered materials and atomically-thin circuits. These potentials will accelerate the discovery of novel materials and the large-scale development of ultrathin multifunctional integrated circuitry.

## REFERENCES

- [1] K. S. Novoselov, Nobel lecture: Graphene: Materials in the flatland. *Rev. Mod. Phys.* **83**, 837 (2011).
- [2] C. Ataca, H. Sahin, S. Ciraci, Stable, single-layer MX<sub>2</sub> transition-metal oxides and dichalcogenides in a honeycomb-like structure. *J. Phys. Chem. C.* **116**, 8983–8999 (2012).
- [3] K. F. Mak, C. Lee, J. Hone, J. Shan, T. F. Heinz, Atomically Thin MoS<sub>2</sub>: A New Direct-Gap Semiconductor. *Phys. Rev. Lett.* **105**, 136805 (2010).
- [4] Z. Ye *et al.*, Probing excitonic dark states in single-layer tungsten disulphide. *Nature.* **513**, 214–218 (2014).
- [5] K. F. Mak, K. L. McGill, J. Park, P. L. McEuen, The valley Hall effect in MoS<sub>2</sub> transistors. *Science.* **344**, 1489–1492 (2014).
- [6] W. Wu *et al.*, Piezoelectricity of single-atomic-layer MoS<sub>2</sub> for energy conversion and piezotronics. *Nature.* **514**, 470–474 (2014).
- [7] H. Zhu *et al.*, Observation of piezoelectricity in free-standing monolayer MoS<sub>2</sub>. *Nat. Nanotechnol.* **10**, 151–155 (2014).
- [8] P. Y. Huang *et al.*, Direct imaging of a two-dimensional silica glass on graphene. *Nano Lett.* **12**, 1081–1086 (2012).
- [9] A. K. Geim, I. V. Grigorieva, Van der Waals heterostructures. *Nature.* **499**, 419–425 (2013).
- [10] B. Huang *et al.*, Layer-dependent ferromagnetism in a van der Waals crystal down to the monolayer limit. *Nature.* **546**, 270–273 (2017).
- [11] C. Gong *et al.*, Discovery of intrinsic ferromagnetism in two-dimensional van der Waals crystals. *Nature.* **546**, 265–269 (2017).
- [12] L. Li *et al.*, Black phosphorus field-effect transistors. *Nat. Nanotechnol.* **9**, 372–377 (2014).
- [13] X. Ling, H. Wang, S. Huang, F. Xia, M. S. Dresselhaus, The renaissance of black phosphorus. *Proc. Natl. Acad. Sci.* **112**, 4523–4530 (2015).
- [14] J. F. Ge *et al.*, Superconductivity above 100 K in single-layer FeSe films on doped SrTiO<sub>3</sub>. *Nat. Mater.* **14**, 285–289 (2015).

- [15] Y. Saito, T. Nojima, Y. Iwasa, Highly crystalline 2D superconductors. *Nat. Rev. Mater.* **2**, 16094 (2016).
- [16] M. Servalli, A. D. Schlüter, Synthetic Two-Dimensional Polymers. *Annu. Rev. Mater. Res.* **47**, 361–389 (2017).
- [17] Q. H. Wang, K. Kalantar-Zadeh, A. Kis, J. N. Coleman, M. S. Strano, Electronics and optoelectronics of two-dimensional transition metal dichalcogenides. *Nat. Nanotechnol.* **7**, 699–712 (2012).
- [18] C. Zhang *et al.*, Systematic study of electronic structure and band alignment of monolayer transition metal dichalcogenides in Van der Waals heterostructures. *2D Mater.* **4**, 15026 (2016).
- [19] K.-A. N. Duerloo, Y. Li, E. J. Reed, Structural phase transitions in two-dimensional Mo- and W-dichalcogenide monolayers. *Nat. Commun.* **5**, 4214 (2014).
- [20] G.-B. Liu, D. Xiao, Y. Yao, X. Xu, W. Yao, Electronic structures and theoretical modelling of two-dimensional group-VIB transition metal dichalcogenides. *Chem. Soc. Rev.* **44**, 2643–2663 (2015).
- [21] K. F. Mak, J. Shan, Photonics and optoelectronics of 2D semiconductor transition metal dichalcogenides. *Nat. Photonics.* **10**, 216–226 (2016).
- [22] W. Yao, D. Xiao, Q. Niu, Valley-dependent optoelectronics from inversion symmetry breaking. *Phys. Rev. B.* **77**, 235406 (2008).
- [23] X. Xu, W. Yao, D. Xiao, T. F. Heinz, Spin and pseudospins in layered transition metal dichalcogenides. *Nat. Phys.* **10**, 343–350 (2014).
- [24] D. Xiao, G. Bin Liu, W. Feng, X. Xu, W. Yao, Coupled spin and valley physics in monolayers of MoS<sub>2</sub> and other group-VI dichalcogenides. *Phys. Rev. Lett.* **108**, 196802 (2012).
- [25] D. Xiao, M.-C. Chang, Q. Niu, Berry phase effects on electronic properties. *Rev. Mod. Phys.* **82**, 1959–2007 (2010).
- [26] T. Cao *et al.*, Valley-selective circular dichroism of monolayer molybdenum disulphide. *Nat. Commun.* **3**, 887 (2012).
- [27] K. F. Mak, K. He, J. Shan, T. F. Heinz, Control of valley polarization in monolayer MoS<sub>2</sub> by optical helicity. *Nat. Nanotechnol.* **7**, 494 (2012).
- [28] H. Zeng, J. Dai, W. Yao, D. Xiao, X. Cui, Valley polarization in MoS<sub>2</sub>

- monolayers by optical pumping. *Nat. Nanotechnol.* **7**, 490–493 (2012).
- [29] G. Sallen *et al.*, Robust optical emission polarization in MoS<sub>2</sub> monolayers through selective valley excitation. *Phys. Rev. B - Condens. Matter Mater. Phys.* **86**, 81301 (2012).
- [30] A. M. Jones *et al.*, Optical generation of excitonic valley coherence in monolayer WSe<sub>2</sub>. *Nat. Nanotechnol.* **8**, 634–638 (2013).
- [31] A. Splendiani *et al.*, Emerging Photoluminescence in Monolayer MoS<sub>2</sub>. *Nano Lett.* **10**, 1271–1275 (2010).
- [32] D. Jena, Tunneling transistors based on graphene and 2-D Crystals. *Proc. IEEE.* **101**, 1585–1602 (2013).
- [33] J. Kang *et al.*, Graphene and beyond-graphene 2D crystals for next-generation green electronics. *Proc. SPIE* **9083**, 908305 (2014).
- [34] S. B. Desai *et al.*, MoS<sub>2</sub> transistors with 1-nanometer gate lengths. *Science.* **354**, 99–102 (2016).
- [35] M. Chhowalla *et al.*, Two-dimensional semiconductors for transistors. *Nat. Rev. Mater.* **1**, 16052 (2016).
- [36] B. Radisavljevic, A. Radenovic, J. Brivio, V. Giacometti, A. Kis, Single-layer MoS<sub>2</sub> transistors. *Nat. Nanotechnol.* **6**, 147–150 (2011).
- [37] B. W. H. Baugher, H. O. H. Churchill, Y. Yang, P. Jarillo-Herrero, Intrinsic Electronic Transport Properties of High-Quality Monolayer and Bilayer MoS<sub>2</sub>. *Nano Lett.* **13**, 4212–4216 (2013).
- [38] B. Radisavljevic, A. Kis, Mobility engineering and a metal–insulator transition in monolayer MoS<sub>2</sub>. *Nat. Mater.* **12**, 815–820 (2013).
- [39] K. S. Novoselov *et al.*, Two-dimensional atomic crystals. *Proc. Natl. Acad. Sci.* **102**, 10451–10453 (2005).
- [40] X. Cui *et al.*, Multi-terminal transport measurements of MoS<sub>2</sub> using a van der Waals heterostructure device platform. *Nat. Nanotechnol.* **10**, 534–540 (2015).
- [41] A. K. Geim, Nobel Lecture: Random walk to graphene. *Rev. Mod. Phys.* **83**, 851–862 (2011).
- [42] A. R. F. Frindt, A. D. Yoffe, Physical properties of layer structures : optical properties and photoconductivity of thin crystals of molybdenum disulphide. *Proc. Roy. Soc. A.* **273**, 69–83 (1962).

- [43] K. S. Novoselov *et al.*, Electric field effect in atomically thin carbon films. *Science*. **306**, 666–669 (2004).
- [44] K. S. Novoselov *et al.*, Two-dimensional gas of massless Dirac fermions in graphene. *Nature*. **438**, 197 (2005).
- [45] Y. Zhang, Y.-W. Tan, H. L. Stormer, P. Kim, Experimental observation of the quantum Hall effect and Berry's phase in graphene. *Nature*. **438**, 201–4 (2005).
- [46] A. K. Geim, K. S. Novoselov, The rise of graphene. *Nat. Mater.* **6**, 183–191 (2007).
- [47] K. S. Novoselov, A. H. Castro Neto, Two-dimensional crystals-based heterostructures: Materials with tailored properties. *Phys. Scr.* **T146**, 014006 (2012).
- [48] J. Kang, D. Shin, S. Bae, B. H. Hong, Graphene transfer: key for applications. *Nanoscale*. **4**, 5527 (2012).
- [49] Y.-C. Lin *et al.*, Wafer-scale MoS<sub>2</sub> thin layers prepared by MoO<sub>3</sub> sulfurization. *Nanoscale*. **4**, 6637–6641 (2012).
- [50] I. Song *et al.*, Patternable large-scale molybdenum disulfide atomic layers grown by gold-assisted chemical vapor deposition. *Angew. Chemie - Int. Ed.* **53**, 1266–1269 (2014).
- [51] J. H. J. H. Kim *et al.*, Work function variation of MoS<sub>2</sub> atomic layers grown with chemical vapor deposition: The effects of thickness and the adsorption of water/oxygen molecules. *Appl. Phys. Lett.* **106**, 251606 (2015).
- [52] S. Zhang *et al.*, Direct Observation of Degenerate Two-Photon Absorption and Its Saturation in WS<sub>2</sub> Monolayer and Few-Layer Films. *ACS Nano*. **9**, 7142–7150 (2015).
- [53] Q. Ji, Y. Zhang, Y. Zhang, Z. Liu, Chemical vapour deposition of group-VIB metal dichalcogenide monolayers: engineered substrates from amorphous to single crystalline. *Chem. Soc. Rev.* **44**, 2587–2602 (2015).
- [54] S. Najmaei *et al.*, Vapour phase growth and grain boundary structure of molybdenum disulphide atomic layers. *Nat. Mater.* **12**, 754–759 (2013).
- [55] A. M. van der Zande *et al.*, Grains and grain boundaries in highly crystalline monolayer molybdenum disulphide. *Nat. Mater.* **12**, 554–561 (2013).
- [56] Y.-H. Lee *et al.*, Synthesis and transfer of single-layer transition metal

- disulfides on diverse surfaces. *Nano Lett.* **13**, 1852–1857 (2013).
- [57] H. Liu *et al.*, Statistical study of deep submicron dual-gated field-effect transistors on monolayer chemical vapor deposition molybdenum disulfide films. *Nano Lett.* **13**, 2640–2646 (2013).
- [58] Y. Yu *et al.*, Controlled Scalable Synthesis of Uniform, High-Quality Monolayer and Few-layer MoS<sub>2</sub> Films. *Sci. Rep.* **3**, 1866 (2013).
- [59] Y. Zhang *et al.*, Controlled growth of high-quality monolayer WS<sub>2</sub> layers on sapphire. *ACS Nano.* **7**, 8963–8971 (2013).
- [60] C. Cong *et al.*, Synthesis and Optical Properties of Large-Area Single-Crystalline 2D Semiconductor WS<sub>2</sub> Monolayer from Chemical Vapor Deposition. *Adv. Opt. Mater.* **2**, 131–136 (2014).
- [61] X. Wang *et al.*, Chemical vapor deposition growth of crystalline monolayer MoSe<sub>2</sub>. *ACS Nano.* **8**, 5125–5131 (2014).
- [62] X. Lu *et al.*, Large-area synthesis of monolayer and few-layer MoSe<sub>2</sub> films on SiO<sub>2</sub> substrates. *Nano Lett.* **14**, 2419–2425 (2014).
- [63] J.-K. Huang *et al.*, Large-Area Synthesis of Highly Crystalline WSe<sub>2</sub> Monolayers and Device Applications. *ACS Nano.* **8**, 923–930 (2014).
- [64] B. Liu *et al.*, Chemical Vapor Deposition Growth of Monolayer WSe<sub>2</sub> with Tunable Device Characteristics and Growth Mechanism Study. *ACS Nano.* **9**, 6119–6127 (2015).
- [65] T. A. Empante *et al.*, Chemical Vapor Deposition Growth of Few-Layer MoTe<sub>2</sub> in the 2H, 1T', and 1T Phases: Tunable Properties of MoTe<sub>2</sub> Films. *ACS Nano.* **11**, 900–905 (2017).
- [66] J. Zhou *et al.*, Large-Area and High-Quality 2D Transition Metal Telluride. *Adv. Mater.* **29**, 1603471 (2017).
- [67] M. Samadi *et al.*, Group 6 transition metal dichalcogenide nanomaterials: synthesis, applications and future perspectives. *Nanoscale Horizons.* **3**, 90–204 (2018).
- [68] X. Duan *et al.*, Lateral epitaxial growth of two-dimensional layered semiconductor heterojunctions. *Nat. Nanotechnol.* **9**, 1024–1030 (2014).
- [69] Y. Gong *et al.*, Vertical and in-plane heterostructures from WS<sub>2</sub>/MoS<sub>2</sub> monolayers. *Nat. Mater.* **13**, 1135–1142 (2014).

- [70] C. Huang *et al.*, Lateral heterojunctions within monolayer MoSe<sub>2</sub>–WSe<sub>2</sub> semiconductors. *Nat. Mater.* **13**, 1096–1101 (2014).
- [71] M.-Y. Li *et al.*, Epitaxial growth of a monolayer WSe<sub>2</sub>-MoS<sub>2</sub> lateral p-n junction with an atomically sharp interface. *Science*. **349**, 524–8 (2015).
- [72] K. F. Mak, C. Lee, J. Hone, J. Shan, T. F. Heinz, Atomically Thin MoS<sub>2</sub>: A New Direct-Gap Semiconductor. *Phys. Rev. Lett.* **105**, 136805 (2010).
- [73] Y. Li *et al.*, Measurement of the optical dielectric function of monolayer transition-metal dichalcogenides : *Phys Rev B.* **205422**, 1–6 (2014).
- [74] M. M. Benameur *et al.*, Visibility of dichalcogenide nanolayers. *Nanotechnology.* **22**, 125706 (2011).
- [75] Z. Y. Zhu, Y. C. Cheng, U. Schwingenschlögl, Giant spin-orbit-induced spin splitting in two-dimensional transition-metal dichalcogenide semiconductors. *Phys. Rev. B - Condens. Matter Mater. Phys.* **84**, 153402 (2011).
- [76] G.-B. Liu, D. Xiao, Y. Yao, X. Xu, W. Yao, Electronic structures and theoretical modelling of two-dimensional group-VIB transition metal dichalcogenides. *Chem. Soc. Rev.* **44**, 2643–2663 (2015).
- [77] K. F. Mak, K. He, J. Shan, T. F. Heinz, Control of valley polarization in monolayer MoS<sub>2</sub> by optical helicity. *Nat. Nanotechnol.* **7**, 494–498 (2012).
- [78] W. Zhao *et al.*, Evolution of Electronic Structure in Atomically Thin Sheets of WS<sub>2</sub> and WSe<sub>2</sub>. *ACS Nano.* **7**, 791–797 (2013).
- [79] P. Tonndorf *et al.*, Photoluminescence emission and Raman response of monolayer MoS<sub>2</sub>, MoSe<sub>2</sub>, and WSe<sub>2</sub>. *Opt. Express.* **21**, 4908 (2013).
- [80] C. Lee *et al.*, Anomalous Lattice Vibrations of Single- and Few-Layer MoS<sub>2</sub>. *ACS Nano.* **4**, 2695–2700 (2010).
- [81] J. L. Verble, T. J. Wieting, Lattice mode degeneracy in MoS<sub>2</sub> and other layer compounds. *Phys. Rev. Lett.* **25**, 362–365 (1970).
- [82] G. L. Frey, R. Tenne, Raman and resonance Raman investigation of MoS<sub>2</sub> nanoparticles. *Phys. Rev. B.* **60**, 2883–2892 (2000).
- [83] H. Zeng *et al.*, Low-frequency Raman modes and electronic excitations in atomically thin MoS<sub>2</sub> films. *Phys. Rev. B.* **86**, 241301 (2012).
- [84] Y. Zhao *et al.*, Interlayer Breathing and Shear Modes in Few-Trilayer MoS<sub>2</sub> and WSe<sub>2</sub>. *Nano Lett.* **13**, 1007–1015 (2013).

- [85] A. Molina-Sánchez, L. Wirtz, Phonons in single-layer and few-layer MoS<sub>2</sub> and WS<sub>2</sub>. *Phys. Rev. B*. **84**, 155413 (2011).
- [86] R. W. Havener *et al.*, High-Throughput Graphene Imaging on Arbitrary Substrates with Wide field Raman Spectroscopy. *ACS Nano* **6**, 373–380 (2012).
- [87] D. B. Williams, C. B. Carter, "*Transmission Electron Microscopy*," Springer US, Boston, MA, (2009).
- [88] P. Y. Huang *et al.*, Grains and grain boundaries in single-layer graphene atomic patchwork quilts. *Nature*. **469**, 389–92 (2011).
- [89] P. Deb *et al.*, Breaking Friedel's Law in Polar Two Dimensional Materials. *Microsc. Microanal.* **23**, 1738–1739 (2017).
- [90] V. Intaraprasong, H. L. Xin, D. A. Muller, Analytic derivation of optimal imaging conditions for incoherent imaging in aberration-corrected electron microscopes. *Ultramicroscopy*. **108**, 1454–1466 (2008).
- [91] O. L. Krivanek *et al.*, Atom-by-atom structural and chemical analysis by annular dark-field electron microscopy. *Nature*. **464**, 571–574 (2010).
- [92] D. A. Muller, Structure and bonding at the atomic scale by scanning transmission electron microscopy. *Nat. Mater.* **8**, 263–270 (2009).
- [93] K. Kang *et al.*, High-mobility three-atom-thick semiconducting films with wafer-scale homogeneity. *Nature*. **520**, 656–660 (2015).
- [94] M. W. Tate *et al.*, High Dynamic Range Pixel Array Detector for Scanning Transmission Electron Microscopy. *Microsc. Microanal.*, 1–13 (2016).
- [95] Y. Han *et al.*, arXiv:1801.08053 (2018).
- [96] Y. Jiang *et al.*, arXiv:1801.04630 (2018).
- [97] C. Hu, "*Modern Semiconductor Devices for Integrated Circuits*," Prentice Hall, Upper Saddle River, NJ, (2010).
- [98] J. A. Rogers, T. Someya, Y. Huang, Materials and mechanics for stretchable electronics. *Science*. **327**, 1603–1607 (2010).
- [99] H. Ko *et al.*, Ultrathin compound semiconductor on insulator layers for high-performance nanoscale transistors. *Nature*. **468**, 286–289 (2010).
- [100] D. B. Mitzi, L. L. Kosbar, C. E. Murray, M. Copel, A. Afzali, High-mobility ultrathin semiconducting films prepared by spin coating. *Nature*. **428**, 299–303 (2003).

- [101] A. K. Geim, I. V Grigorieva, Van der Waals heterostructures. *Nature*. **499**, 419–425 (2013).
- [102] K. Kaasbjerg, K. S. Thygesen, K. W. Jacobsen, Phonon-limited mobility in n-type single-layer MoS<sub>2</sub> from first principles. *Phys. Rev. B*. **85**, 115317 (2012).
- [103] B. W. H. Baugher, H. O. H. Churchill, Y. Yang, P. Jarillo-Herrero, Intrinsic electronic transport properties of high-quality monolayer and bilayer MoS<sub>2</sub>. *Nano Lett.* **13**, 4212–4216 (2013).
- [104] B. Radisavljevic, A. Kis, Mobility engineering and a metal-insulator transition in monolayer MoS<sub>2</sub>. *Nat. Mater.* **12**, 815–820 (2013).
- [105] H. Schmidt *et al.*, Transport properties of monolayer MoS<sub>2</sub> grown by chemical vapor deposition. *Nano Lett.* **14**, 1909–1913 (2014).
- [106] D. Jariwala *et al.*, Band-like transport in high mobility unencapsulated single-layer MoS<sub>2</sub> transistors. *Appl. Phys. Lett.* **102**, 173107 (2013).
- [107] D. Ovchinnikov *et al.*, Electrical transport properties of single-layer WS<sub>2</sub>. *ACS Nano*. **8**, 8174–8181 (2014).
- [108] Q. Feng *et al.*, Growth of Large-Area 2D MoS<sub>2(1-x)</sub>.Se<sub>2x</sub> Semiconductor Alloys. *Adv. Mater.* **26**, 2648–2653 (2014).
- [109] H. Li *et al.*, From bulk to monolayer MoS<sub>2</sub>: evolution of Raman scattering. *Adv. Funct. Mater.* **22**, 1385–1390 (2012).
- [110] A. Berkdemir *et al.*, Identification of individual and few layers of WS<sub>2</sub> using Raman spectroscopy. *Sci. Rep.* **3**, 1755 (2013).
- [111] D. A. King, D. P. Woodruff, "*Growth and Properties of Ultrathin Epitaxial Layers*," Elsevier, Amsterdam, (1997).
- [112] R. Connor, H. Adkins, Hydrogenolysis of oxygenated organic compounds. *J. Am. Chem. Soc.* **54**, 4678–4690 (1932).
- [113] S. Cristol *et al.*, Theoretical study of the MoS<sub>2</sub> (100). surface: A chemical potential analysis of sulfur and hydrogen coverage. *J. Phys. Chem. B*. **104**, 11220–11229 (2000).
- [114] S. Li *et al.*, Halide-assisted atmospheric pressure growth of large WSe<sub>2</sub> and WS<sub>2</sub> monolayer crystals. *Appl. Mater. Today*. **1**, 60–66 (2015).
- [115] H. Kim, D. Ovchinnikov, D. Deiana, D. Unuchek, A. Kis, Suppressing Nucleation in Metal–Organic Chemical Vapor Deposition of MoS<sub>2</sub> Monolayers

- by Alkali Metal Halides. *Nano Lett.* **17**, 5056–5063 (2017).
- [116] Z. Wang *et al.*, NaCl-assisted one-step growth of MoS<sub>2</sub>–WS<sub>2</sub> in-plane heterostructures. *Nanotechnology.* **28**, 325602 (2017).
- [117] J. H. Sung *et al.*, Coplanar semiconductor–metal circuitry defined on few-layer MoTe<sub>2</sub> via polymorphic heteroepitaxy. *Nat. Nanotechnol.* **12**, 1064–1070 (2017).
- [118] J. Zhou *et al.*, A library of atomically thin metal chalcogenides. *Nature.* **556**, 355–359 (2018).
- [119] S. Najmaei *et al.*, Electrical Transport Properties of Polycrystalline Monolayer Molybdenum Disulfide. *ACS Nano.* **8**, 7930–7937 (2014).
- [120] J. Wang *et al.*, Epitaxial BiFeO<sub>3</sub> multiferroic thin film heterostructures. *Science.* **299**, 1719–1722 (2003).
- [121] D. G. Schlom *et al.*, Elastic strain engineering of ferroic oxides. *MRS Bull.* **39**, 118–130 (2014).
- [122] J. Faist *et al.*, Quantum Cascade Laser. *Science.* **264**, 553–556 (1994).
- [123] S. Nakamura, The Roles of Structural Imperfections in InGaN-Based Blue Light-Emitting Diodes and Laser Diodes. *Science.* **281**, 956–961 (1998).
- [124] V. I. Vdovin, Misfit Dislocations in Epitaxial Heterostructures: Mechanisms of Generation and Multiplication. *Phys. status solidi.* **171**, 239–250 (1999).
- [125] D. Jariwala, T. J. Marks, M. C. Hersam, Mixed-dimensional van der Waals heterostructures. *Nat. Mater.* **16**, 170–181 (2016).
- [126] D. Sarkar *et al.*, A subthermionic tunnel field-effect transistor with an atomically thin channel. *Nature.* **526**, 91–95 (2015).
- [127] Q. H. Wang, K. Kalantar-Zadeh, A. Kis, J. N. Coleman, M. S. Strano, Electronics and optoelectronics of two-dimensional transition metal dichalcogenides. *Nat. Nanotechnol.* **7**, 699–712 (2012).
- [128] K. Chen *et al.*, Electronic Properties of MoS<sub>2</sub>–WS<sub>2</sub> Heterostructures Synthesized with Two-Step Lateral Epitaxial Strategy. *ACS Nano.* **9**, 9868–9876 (2015).
- [129] Y. Gong *et al.*, Two-Step Growth of Two-Dimensional WSe<sub>2</sub>/MoSe<sub>2</sub> Heterostructures. *Nano Lett.* **15**, 6135–6141 (2015).
- [130] X. Q. Zhang, C. H. Lin, Y. W. Tseng, K. H. Huang, Y. H. Lee, Synthesis of

- lateral heterostructures of semiconducting atomic layers. *Nano Lett.* **15**, 410–415 (2015).
- [131] H. Heo *et al.*, Rotation-Misfit-Free Heteroepitaxial Stacking and Stitching Growth of Hexagonal Transition-Metal Dichalcogenide Monolayers by Nucleation Kinetics Controls. *Adv. Mater.* **27**, 3803–3810 (2015).
- [132] K. Bogaert *et al.*, Diffusion-Mediated Synthesis of MoS<sub>2</sub>/WS<sub>2</sub> Lateral Heterostructures. *Nano Lett.* **16**, 5129–5134 (2016).
- [133] S. Xie *et al.*, Coherent, atomically thin transition-metal dichalcogenide superlattices with engineered strain. *Science*. **359**, 1131–1136 (2018).
- [134] S. Helveg *et al.*, Atomic-Scale Structure of Single-Layer MoS<sub>2</sub> Nanoclusters. *Phys. Rev. Lett.* **84**, 951–954 (2000).
- [135] J. V. Lauritsen *et al.*, Size-dependent structure of MoS<sub>2</sub> nanocrystals. *Nat. Nanotechnol.* **2**, 53–58 (2007).
- [136] P. Johari, V. B. Shenoy, Tuning the Electronic Properties of Semiconducting Transition Metal Dichalcogenides by Applying Mechanical Strains. *ACS Nano*. **6**, 5449–5456 (2012).
- [137] Y. Wang *et al.*, Strain-induced direct–indirect bandgap transition and phonon modulation in monolayer WS<sub>2</sub>. *Nano Res.* **8**, 2562–2572 (2015).
- [138] R. Schmidt *et al.*, Reversible uniaxial strain tuning in atomically thin WSe<sub>2</sub>. *2D Mater.* **3**, 21011 (2016).
- [139] R. Frisenda *et al.*, Biaxial strain tuning of the optical properties of single-layer transition metal dichalcogenides. *npj 2D Mater. Appl.* **1**, 10 (2017).
- [140] Y. Klein, E. Efrati, E. Sharon, Shaping of Elastic Sheets by Prescription of Non-Euclidean Metrics. *Science*. **315**, 1116–1120 (2007).
- [141] B. Davidovitch, R. D. Schroll, D. Vella, M. Adda-Bedia, E. A. Cerda, Prototypical model for tensional wrinkling in thin sheets. *Proc. Natl. Acad. Sci.* **108**, 18227–18232 (2011).
- [142] D. Nandwana, E. Ertekin, Ripples, Strain, and Misfit Dislocations: Structure of Graphene–Boron Nitride Superlattice Interfaces. *Nano Lett.* **15**, 1468–1475 (2015).
- [143] A. Ambrosetti, N. Ferri, R. A. DiStasio, A. Tkatchenko, Wavelike charge density fluctuations and van der Waals interactions at the nanoscale. *Science*.

351, 1171–1176 (2016).

- [144] J. W. Matthews, A. E. Blakeslee, Defects in epitaxial multilayers. *J. Cryst. Growth.* **27**, 118–125 (1974).
- [145] R. People, J. C. Bean, Calculation of critical layer thickness versus lattice mismatch for  $\text{Ge}_x\text{Si}_{1-x}/\text{Si}$  strained-layer heterostructures. *Appl. Phys. Lett.* **47**, 322–324 (1985).
- [146] J. E. Ayers, Mismatched Heteroepitaxial Growth and Strain Relaxation. *Heteroepitaxy Semicond.*, 161–248 (2007).
- [147] D. Wickramaratne, F. Zahid, R. K. Lake, Electronic and thermoelectric properties of few-layer transition metal dichalcogenides. *J. Chem. Phys.* **140**, 124710 (2014).
- [148] H. D. Barber, Effective mass and intrinsic concentration in silicon. *Solid. State. Electron.* **10**, 1039–1051 (1967).
- [149] Z. I. Alferov, Nobel Lecture: The double heterostructure concept and its applications in physics, electronics, and technology. *Rev. Mod. Phys.* **73**, 767–782 (2001).
- [150] M. H. D. Guimarães *et al.*, Atomically thin ohmic edge contacts between two-dimensional materials. *ACS Nano.* **10**, 6392–6399 (2016).
- [151] C. R. Dean *et al.*, Boron nitride substrates for high-quality graphene electronics. *Nat. Nanotechnol.* **5**, 722–726 (2010).
- [152] G. Scuri *et al.*, Large Excitonic Reflectivity of Monolayer  $\text{MoSe}_2$  Encapsulated in Hexagonal Boron Nitride. *Phys. Rev. Lett.* **120**, 37402 (2018).
- [153] O. A. Ajayi *et al.*, Approaching the intrinsic photoluminescence linewidth in transition metal dichalcogenide monolayers. *2D Mater.* **4**, 31011 (2017).
- [154] F. Cadiz *et al.*, Excitonic Linewidth Approaching the Homogeneous Limit in  $\text{MoS}_2$ -Based van der Waals Heterostructures. *Phys. Rev. X.* **7**, 21026 (2017).
- [155] P. J. Zomer, M. H. D. Guimarães, J. C. Brant, N. Tombros, B. J. van Wees, Fast pick up technique for high quality heterostructures of bilayer graphene and hexagonal boron nitride. *Appl. Phys. Lett.* **105**, 13101 (2014).
- [156] X. Duan, C. Wang, A. Pan, R. Yu, X. Duan, Two-dimensional transition metal dichalcogenides as atomically thin semiconductors : opportunities and challenges. *Chem. Soc. Rev.* **44**, 8859–8876 (2015).

- [157] M. P. Levendorf *et al.*, Graphene and boron nitride lateral heterostructures for atomically thin circuitry. *Nature*. **488**, 627–632 (2012).
- [158] A. D. Franklin, Nanomaterials in transistors: From high-performance to thin-film applications. *Science*. **349**, aab2750 (2015).
- [159] D. Jariwala, V. K. Sangwan, L. J. Lauhon, T. J. Marks, M. C. Hersam, Emerging Device Applications for Semiconducting Two-Dimensional Transition Metal Dichalcogenides. *ACS Nano*. **8**, 1102–1120 (2014).
- [160] G. Fiori *et al.*, Electronics based on two-dimensional materials. *Nat. Nanotechnol.* **9**, 768–779 (2014).
- [161] K. S. Novoselov *et al.*, A roadmap for graphene. *Nature*. **490**, 192–200 (2012).
- [162] B. Radisavljevic, A. Radenovic, J. Brivio, V. Giacometti, A. Kis, Single-layer MoS<sub>2</sub> transistors. *Nat. Nanotechnol.* **6**, 147–50 (2011).
- [163] F. Léonard, A. A. Talin, Electrical contacts to one- and two-dimensional nanomaterials. *Nat. Nanotechnol.* **6**, 773–783 (2011).
- [164] A. Allain, J. Kang, K. Banerjee, A. Kis, Electrical contacts to two-dimensional semiconductors. *Nat. Mater.* **14**, 1195–1205 (2015).
- [165] Y. Xu *et al.*, Contacts between Two- and Three-Dimensional Materials: Ohmic, Schottky, and p–n Heterojunctions. *ACS Nano*. **10**, 4895–4919 (2016)
- [166] W. Liu *et al.*, Role of Metal Contacts in Designing High-Performance Monolayer n-Type WSe<sub>2</sub> Field Effect Transistors. *Nano Lett.* **13**, 1983–1990 (2013).
- [167] H. Liu *et al.*, Switching Mechanism in Single-Layer Molybdenum Disulfide Transistors: An Insight into Current Flow across Schottky Barriers. *ACS Nano*. **8**, 1031–1038 (2014).
- [168] M. W. Iqbal *et al.*, High-mobility and air-stable single-layer WS<sub>2</sub> field-effect transistors sandwiched between chemical vapor deposition-grown hexagonal BN films. *Sci. Rep.* **5**, 10699 (2015).
- [169] A. Rai *et al.*, Air Stable Doping and Intrinsic Mobility Enhancement in Monolayer Molybdenum Disulfide by Amorphous Titanium Suboxide Encapsulation. *Nano Lett.* **15**, 4329–4336 (2015).
- [170] A. Sanne *et al.*, Radio Frequency Transistors and Circuits Based on CVD MoS<sub>2</sub>. *Nano Lett.* **15**, 5039–5045 (2015).

- [171] W. Liu, D. Sarkar, J. Kang, W. Cao, K. Banerjee, Impact of Contact on the Operation and Performance of Back-Gated Monolayer MoS<sub>2</sub> Field-Effect-Transistors. *ACS Nano*. **9**, 7904–7912 (2015).
- [172] S.-L. Li *et al.*, Thickness Scaling Effect on Interfacial Barrier and Electrical Contact to Two-Dimensional MoS<sub>2</sub> Layers. *ACS Nano*. **8**, 12836–12842 (2014).
- [173] Y. Liu *et al.*, Toward Barrier Free Contact to Molybdenum Disulfide Using Graphene Electrodes. *Nano Lett.* **15**, 3030–3034 (2015).
- [174] J. Kang, W. Liu, D. Sarkar, D. Jena, K. Banerjee, Computational Study of Metal Contacts to Monolayer Transition-Metal Dichalcogenide Semiconductors. *Phys. Rev. X*. **4**, 31005 (2014).
- [175] Y. Ma, Y. Dai, M. Guo, C. Niu, B. Huang, Graphene adhesion on MoS<sub>2</sub> monolayer: An ab initio study. *Nanoscale*. **3**, 3883 (2011).
- [176] X. Ling *et al.*, Parallel Stitching of 2D Materials. *Adv. Mater.* **28**, 2322–2329 (2016).
- [177] L. Wang *et al.*, One-dimensional electrical contact to a two-dimensional material. *Science*. **342**, 614–617 (2013).
- [178] S. Cho *et al.*, Phase patterning for ohmic homojunction contact in MoTe<sub>2</sub>. *Science*. **349**, 625–628 (2015).
- [179] R. Kappera *et al.*, Phase-engineered low-resistance contacts for ultrathin MoS<sub>2</sub> transistors. *Nat. Mater.* **13**, 1128–1134 (2014).
- [180] H. Yamaguchi *et al.*, Spatially Resolved Photoexcited Charge-Carrier Dynamics in Phase-Engineered Monolayer MoS<sub>2</sub>. *ACS Nano*. **9**, 840–849 (2015).
- [181] L. Brown *et al.*, Polycrystalline Graphene with Single Crystalline Electronic Structure. *Nano Lett.* **14**, 5706–5711 (2014).
- [182] K. K. H. Smithe, C. D. English, S. V. Suryavanshi, E. Pop, High Mobility in Monolayer MoS<sub>2</sub> Devices Grown by Chemical Vapor Deposition. *IEEE* **3087**, 239–240 (2015)
- [183] Z. Li, X. Li, J. Yang, Comparative Study on Electronic Structures of Sc and Ti Contacts with Monolayer and Multilayer MoS<sub>2</sub>. *ACS Appl. Mater. Interfaces*. **7**, 12981–12987 (2015).
- [184] Y. Guo *et al.*, Study on the Resistance Distribution at the Contact between

- Molybdenum Disulfide and Metals. *ACS Nano*. **8**, 7771–7779 (2014).
- [185] K. Kang *et al.*, Layer-by-layer assembly of two-dimensional materials into wafer-scale heterostructures. *Nature*. **550**, 229–233 (2017).
- [186] Y. Liu *et al.*, Van der Waals heterostructures and devices. *Nat. Rev. Mater.* **1**, 16042 (2016).
- [187] K. S. Novoselov, A. Mishchenko, A. Carvalho, A. H. Castro Neto, 2D materials and van der Waals heterostructures. *Science*. **6298**, aac9439 (2016).
- [188] W. Xu *et al.*, Correlated fluorescence blinking in two-dimensional semiconductor heterostructures. *Nature*. **541**, 62–67 (2017).
- [189] B. Hunt *et al.*, Massive Dirac Fermions and Hofstadter Butterfly in a van der Waals Heterostructure. *Science*. **340**, 1427–1430 (2013).
- [190] P. Rivera *et al.*, Valley-polarized exciton dynamics in a 2D semiconductor heterostructure. *Science*. **351**, 688–691 (2016).
- [191] C.-J. Kim *et al.*, Chiral atomically thin films. *Nat. Nanotechnol.* **11**, 520–524 (2016).
- [192] K. Liu *et al.*, Evolution of interlayer coupling in twisted molybdenum disulfide bilayers. *Nat. Commun.* **5**, 4966 (2014).
- [193] D.-H. Kim *et al.*, Stretchable and Foldable Silicon Integrated Circuits. *Science*. **320**, 507–511 (2008).
- [194] H. Jang *et al.*, Quantum Confinement Effects in Transferrable Silicon Nanomembranes and Their Applications on Unusual Substrates. *Nano Lett.* **13**, 5600–5607 (2013).
- [195] B. Li *et al.*, Scalable Transfer of Suspended Two-Dimensional Single Crystals. *Nano Lett.* **15**, 5089–5097 (2015).
- [196] M.-H. Chiu *et al.*, Spectroscopic Signatures for Interlayer Coupling in MoS<sub>2</sub>-WSe<sub>2</sub> van der Waals Stacking. *ACS Nano*. **8**, 9649–9656 (2014).
- [197] A. V Kretinin *et al.*, Electronic Properties of Graphene Encapsulated with Different Two-Dimensional Atomic Crystals. *Nano Lett.* **14**, 3270–3276 (2014).
- [198] W. S. Yun, S. W. Han, S. C. Hong, I. G. Kim, J. D. Lee, Thickness and strain effects on electronic structures of transition metal dichalcogenides: 2H-MX<sub>2</sub> semiconductors (M = Mo, W; X = S, Se, Te).. *Phys. Rev. B*. **85**, 33305 (2012).
- [199] L. Britnell *et al.*, Electron Tunneling through Ultrathin Boron Nitride

Crystalline Barriers. *Nano Lett.* **12**, 1707–1710 (2012).

- [200] J. G. Simmons, Generalized Formula for the Electric Tunnel Effect between Similar Electrodes Separated by a Thin Insulating Film. *J. Appl. Phys.* **34**, 1793–1803 (1963).
- [201] J. Kang, S. Tongay, J. Zhou, J. Li, J. Wu, Band offsets and heterostructures of two-dimensional semiconductors. *Appl. Phys. Lett.* **102**, 12111 (2013).
- [202] P. Maraghechi, A. Foroughi-Abari, K. Cadien, A. Y. Elezzabi, Enhanced rectifying response from metal-insulator-insulator-metal junctions. *Appl. Phys. Lett.* **99**, 253503 (2011).
- [203] S. H. Baek *et al.*, Giant Piezoelectricity on Si for Hyperactive MEMS. *Science*. **334**, 958–961 (2011).
- [204] J. Feng *et al.*, Single-layer MoS<sub>2</sub> nanopores as nanopower generators. *Nature*. **536**, 197–200 (2016).
- [205] A. Gurarlan *et al.*, Surface-Energy-Assisted Perfect Transfer of Centimeter-Scale Monolayer and Few-Layer MoS<sub>2</sub> Films onto Arbitrary Substrates. *ACS Nano*. **8**, 11522–11528 (2014).
- [206] X. Xi *et al.*, Strongly enhanced charge-density-wave order in monolayer NbSe<sub>2</sub>. *Nat. Nanotechnol.* **10**, 765–769 (2015).